Chem Soc Rev

Recent Advances in Activating Surface Reconstruction for High-efficiency Oxygen Evolution Reaction

Journal:	*Chemical Society Reviews*
Manuscript ID	CS-SYN-07-2020-000962.R2
Article Type:	Review Article
Date Submitted by the Author:	04-Jun-2021
Complete List of Authors:	Gao, Likun; Georgia Institute of Technology, Materials Science and Engineering Cui, Xun; South-Central University for Nationalities, College of Chemistry and Materials Science Sewell, Christopher; Georgia Institute of Technology, Materials Science and Engineering Li, Jian; Northeast Forestry University, Key Laboratory of Bio-Based Material Science & Technology (Northeast Forestry University), Ministry of Education Lin, Zhiqun; Georgia Institute of Technology, Materials Science and Engineering

Recent Advances in Activating Surface Reconstruction for High-Efficiency Oxygen Evolution Reaction

Likun Gao,[#a,b] Xun Cui,[#a] Christopher D Sewell,[#a] Jian Li,[b] Zhiqun Lin*[a]

a. School of Materials Science and Engineering, Georgia Institute of Technology, Atlanta, GA 30332, USA.

b. Key Laboratory of Bio-based Material Science and Technology of Ministry of Education, Northeast Forestry University, Harbin 150040, China.

[#]These authors contributed equally: Likun Gao, Xun Cui, Christopher D Sewell

*Corresponding Authors: Zhiqun Lin

Email: zhiqun.lin@mse.gatech.edu

Abstract

A climax in the development of cost-effective and high-efficiency transition-metal-based electrocatalysts have been witnessed recently for sustainable energy and related conversion technologies. In this regard, structure-activity relationships based on several descriptors have already been proposed to rationally design electrocatalysts. However, the dynamic reconstruction of catalyst surface structures and compositions during electrocatalytic water oxidation, especially during the anodic oxygen evolution reaction (OER), complicate the streamlined prediction of catalytic activity. With the achievements in the operando and in situ techniques, it has been found that electrocatalysts occur surface reconstruction to in situ form the actual active species accompanied with the increased oxidation states during the OER in alkaline solution. Thorough understanding of the surface reconstruction process plays a critical role in establishing the unambiguous structure-composition-property relationships in pursuit of high-efficiency electrocatalysts. However, there remains several issues which are to be explored before realizing high electrocatalytic activities, including: (1) the identification of

initiators and pathways for surface reconstruction, (2) establishing the relationships between structure, composition, and electrocatalytic activity, and (3) the rational manipulation of the in situ catalyst surface reconstruction. In this review, the recent progress in the surface reconstruction of the transition-metal-based OER catalysts including oxides, non-oxides, hydroxides and alloys were summarized, emphasizing the fundamental understanding of reconstruction behavior from the original precatalysts to the actual catalysts based on operando analysis and theoretical calculations. The state-of-the-art strategies to tailor the surface reconstruction such as substituting/doping with metals, introducing anions, incorporating oxygen vacancies, tuning morphologies and exploiting plasmonic/thermal/photothermal effects, are then introduced. It is notable that the comprehensive operando/in situ characterizations together with computational calculations responsible for unveiling the improvement mechanism of OER. By delivering these progress, strategies, insights, techniques, and perspectives, this review will provide a comprehensive understanding of surface reconstruction and future guidelines for rationally developing the transition-metal-based OER catalysts.

1. Introduction

The design of high-efficiency, low-cost hydrogen fuel production is a critical piece in the development of clean and renewable energy for the societal, economic and environmental infrastructure.[1, 2] The sluggish reaction kinetics of the anodic reaction, where the oxygen evolution reaction (OER) takes place, restrict the improvement of water electrolysis efficiency, thereby hindering the realization of such an infrastructure.[2, 3] In addition, the precious-metal-based compounds such as RuO_2 and IrO_2, have been recognized as the state-of-art OER electrocatalysts, yet the scarcity of these compounds inevitably creates the cost issues for electrochemical energy technologies.[4] Transition-metal-based catalysts, typically comprising transition-metal elements and non-metal elements in **Fig. 1**, are cost-effective, and have recently been the focus of several studies yielding significant developments in their apparent electrocatalytic performance, especially for stable OER in alkaline media. In particular, more and more attention has been centered on gaining an in-depth understanding of catalytic

mechanisms and the dynamic behaviors of electrocatalysts under operando conditions, which enables the identification of highly active OER catalysts and further rational design of advanced electrocatalysts.[5, 6]

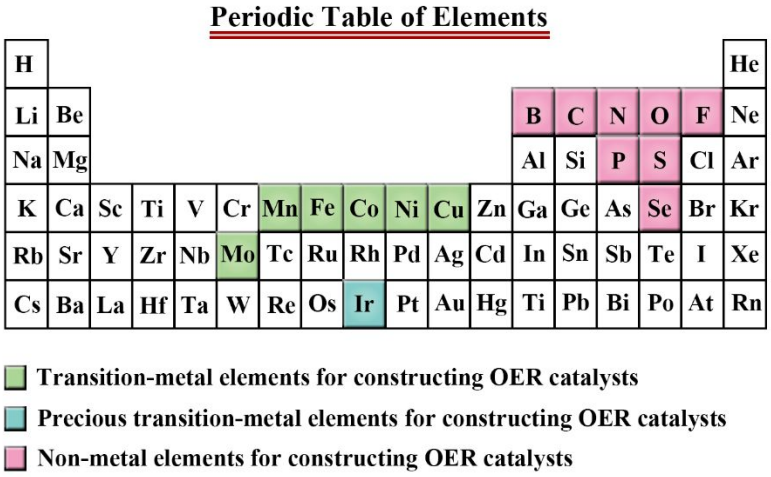

Fig. 1 The investigated elements for constructing transition-metal-based OER catalysts.

Generally, the activity of electrocatalysts is strongly linked to their structural characteristics and electron configurations. The transition metal cations with high valences are typically the highly active sites during water oxidation. However, transition metal cations tend to exist in the more stable, low oxidation states when under nonreaction conditions, as illustrated by Pourbaix diagrams.[7, 8] It has been found that transition-metal-based electrocatalysts[9-12], including oxides, non-oxides, hydroxides, and alloys; as well as several metal-organic frameworks (MOFs)[5, 13], such as NiCo-MOF, CoFe-MOF, etc.; and MOF-derived materials[14], such as MOF-derived bimetallic phosphide (FeNiP/C), etc., function as 'precatalysts', which are in situ oxidized into more active species at an applied potential during a practical electrocatalytic reaction process. The specific dynamic changes in a catalyst's local structure or atomic-level structure have been figuratively coupled with the concept of 'reconstruction'. With the development of operando/in situ characterization techniques, extensive research has been carried out via a series of real-time and in-place measurements/observations to track the reconstruction process, capture the dynamic evolution of electrocatalysts, and identify the true active species of various catalytic materials.[15] The results have demonstrated that most transition metal cations undergo a reconstruction process

involving an increase of the metal cations oxidation states or the leaching out of some metal cations or anions under OER conditions. Density functional theory (DFT) calculations based on modeled catalyst structures and changes in Gibbs free energies have been employed to interpret the electronic structure of the reconstructed electrocatalysts as well as unveil the mechanisms of the observed dynamic reconstruction and improvement in electrocatalytic activity.[16, 17] However, from recent progress in electrocatalytic dynamic reconstruction during the OER, it is imperative to establish more systematic understanding of dynamic reconstruction to discover the initiation factor of reconstruction and the relationship between reconstruction and electrocatalytic activity.

A range of reconstructed electrocatalysts, formed from the respective transition-metal-based precatalysts, have been reported; for example, some metal oxides and (oxy)hydroxides have been proven to exhibit more favorable properties as an OER catalyst than the corresponding original precatalysts and the same catalyst materials that were, instead, synthesized directly.[18-21] In this regard, there are many potential reasons for the improved OER activities which still require investigation. Currently, extensive research attention is focused on modulating the electrochemical oxidation potential needed to obtain the high-efficiency metal oxide/(oxy)hydroxide catalysts, which are more active but prove difficult to synthesize through common methods.[22, 23]

From the development perspective, more rational and effective strategies can be discovered and utilized to activate and tailor the surface reconstruction. For example, one study introduced additional energy into an electrocatalyst system through the thermal effect; and were successfully able to reduce the energy barrier required for surface reconstruction, resulting in a complete reconstruction.[23, 24] On the other hand, for partial surface reconstruction, the key fundamental issues concerning the synergistic electronic interactions between the reconstructed and original components have not been elucidated so far. Additionally, the scientific correlation among the reconstructed catalytic species, the degree of reconstruction, and the catalytic activity should be established through the analysis techniques and computational simulations, which is critical for providing guidelines to prepare highly efficient OER catalysts.

In this review, we spotlight the recent progress made regarding the dynamic reconstruction

of electrocatalysts during the OER, including the classification of the original catalysts, several strategies for modulating surface reconstruction, the identification of active species with related operando/in situ analyses and DFT calculations, and the current understanding of underlying mechanisms (summarized in **Fig. 2**), aiming to establish a guideline for comprehensive understanding of dynamic reconstruction as well as the mechanism causing improved OER activity. In the last section, several remaining challenges and new opportunities are discussed to potentially advance the studies of dynamic reconstruction in electrocatalytic reactions and aid in the rational design of high-performance earth-abundant electrocatalysts.

Fig. 2 Schematic illustration of the activation strategies for oxygen evolution reaction, including the classification of the original catalysts, the identifications of active species with related operando/in situ analyses and DFT calculations, and the cognition of underlying mechanisms.

2. Mechanisms for OER and surface activation

To better illustrate the surface reconstruction of transition-metal-based electrocatalysts in alkaline water oxidation and provide a more insightful understanding of structure-activity correlations during the OER, it is necessary to briefly introduce the fundamental principles of the OER. The thermodynamic equilibrium potential (E^0) of the OER is 1.23 V versus reversible

hydrogen electrode (RHE) under standard conditions.[2] Unfortunately, in practical electrocatalytic OER processes, the large energy barrier originating from the sluggish reaction kinetics generally causes applied potentials much higher than that of the equilibrium potential to be required (i.e., requires high overpotential) to achieve appreciable conversion of OH^- to O_2. Thus, under experimental conditions, OER requires high energy input and yields low energy conversion efficiency.[25, 26] In order to enable the OER to proceed at the potentials closer to the thermodynamic limit (i.e. reduce the overpotential), researchers have proposed several possible OER mechanisms that are instrumental for the targeted design and development of high-efficiency OER electrocatalysts. In this section, we focus on the fundamental principles of the alkaline OER and then provide a systematic understanding of surface reconstruction as well as the corresponding enhancement mechanism of electrocatalytic OER activity.

2.1. Fundamental principles of the OER

It should be acknowledged that the mechanism of OER is very complex and strongly associated to the structure of the electrocatalyst surface. In general, the most widely recognized OER mechanism is the adsorbate evolution mechanism (AEM), which involves a concerted four electron-proton transfers on the transition metal cation sites to yield O_2, as described in **Fig. 3a** and eqn (1) ~ (5).[27-29] Typically, *OH (* refers to the active site on the electrocatalyst) first generates on the active site (eqn (1)). The *OH then experiences a proton-coupled electron transfer process and transforms into *O (eqn (2)). Subsequently, *O undergoes one of the two following possible pathways to produce molecular O_2: (i) the direct coupling of two *O (eqn (3)) or (ii) the formation of *OOH by reacting with another OH^-, which further converts to O_2 through another proton-coupled electron transfer process (eqn (4) ~ (5)).[30-32]

$$OH^- + * \rightarrow *OH + e^- \quad (1)$$

$$*OH + OH^- \rightarrow *O + H_2O + e^- \quad (2)$$

$$*O + *O \rightarrow O_2 \quad (3)$$

or

$$*O + OH^- \rightarrow *OOH + e^- \quad (4)$$

$$*OOH + OH^- \rightarrow * + O_2 + e^- + H_2O \quad (5)$$

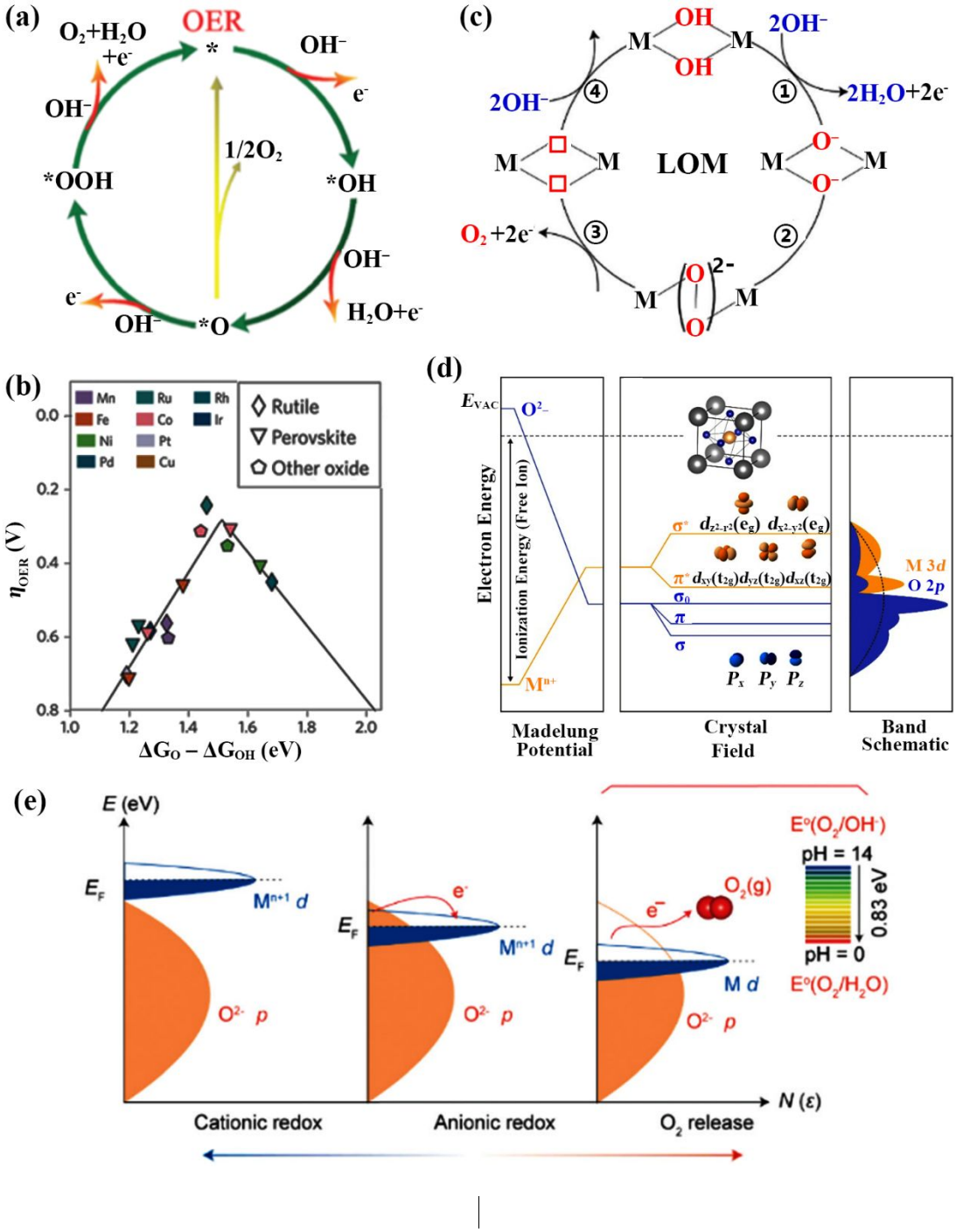

Fig. 3 (a) Schematic illustration of the AEM mechanism for the OER in alkaline electrolytes, where ‘‘*’’ represents the active site. Reproduced with permission from ref. 27. Copyright 2020, Royal Society of Chemistry. (b) Volcano plot for different kinds of transition-metal-based oxides for OER. Reproduced with permission from ref. 33. Copyright 2017, Springer Nature. (c) Schematic illustration of the LOM (lattice-oxygen-mediated mechanism) mechanism of the OER. Reproduced with permission from ref. 34. Copyright 2020, Royal

Society of Chemistry. (d) Schematic diagram illustrating the band structure of perovskite oxides. The inset unit cell is ascribed to the perovskite oxide. Reproduced with permission from ref. 35. Copyright 2015, Royal Society of Chemistry. (e) Schematic of the various oxidation-reduction processes occurred in perovskite oxides. The energy of M *d*-band reduces relative to the O 2*p*-band. Reproduced with permission from ref. 36. Copyright 2016, Springer Nature.

The overall OER performance on an electrocatalyst surface may be restricted by any of the above reaction processes; therefore, a systematic understanding of the bonding interaction between active sites and the oxygen-containing intermediates (*OH, *O, and *OOH) during the reaction is critical for the development of better OER electrocatalysts. In fact, the multistep OER mechanism has not yet been entirely experimentally verified until now owing to the complexity involved in the multi-electron transfer process. Nonetheless, a common consensus is that the interactions between the catalyst surface and reactants, oxygen-containing intermediates, and products play critical roles in determining the activation energy of the electrocatalytic OER.

Based on the Sabatier principle, to achieve optimal OER activity, the binding strengths of reaction intermediates to the active sites must be neither too strong nor too weak to ensure a delicate balance between ease of adsorption and desorption.[37] Previous DFT-based computational calculations have pointed out a general scaling relationship exists between the binding energies of *OH and *OOH (i.e., $\Delta G_{*OOH} - \Delta G_{*OH} = 3.2 \pm 0.2$ eV), indicating that the free energy diagram of OER pathway is, in fact, determined by only one free parameter, namely, the formation of *OOH species.[38] In addition, considering that the OH^- adsorption (eqn (1)) or O_2 release (eqn (5)) steps rarely play the potential-determining role in most OER electrocatalysts, $\Delta G_{*O} - \Delta G_{*OH}$ is universally used as the activity descriptor to evaluate the OER performance of a wide variety of metal-based catalysts.[33] As per the volcano plot in **Fig. 3b**, an ideal OER electrocatalyst with optimal activity requires intermediate binding strengths and a $\Delta G_{*O} - \Delta G_{*OH}$ value of 1.6 eV (corresponding to the apex of the volcano). It is worth noting that either too strong (left side of the volcano) or too weak (right side of the volcano) oxygen-binding will result in the formation of *OOH or the deprotonation of *OH being the

rate-determining step, respectively, limiting the overall kinetics of OER. However, in fact, the performance of most oxide-based OER electrocatalysts, including perovskite-, spinel-, rutile-, bixbyite-, and rock salt-based catalysts, operate in accordance with the aforementioned AEM; and thus are restricted by the scaling relationships between the oxygen intermediates, resulting in relatively large overpotentials for catalyzing OER. While the difference between ΔG_{*OH} and ΔG_{*OOH} is greater than 2.46 eV (2 × 1.23 eV), the minimum theoretical overpotential for an ideal catalyst is calculated to be 0.37 eV ([3.2 – 2 × 1.23]/2).[38-40] In this context, alleviating or breaking the restriction of this scaling relationship should be an effective approach to further enhance the electrocatalytic OER performance.

Considering that the binding strengths of oxygen-containing intermediates are greatly affected by the electronic structure of the electrocatalyst surface, it can feasibly achieve a high-efficiency catalyst via modulating the electronic configuration of the catalyst surface to optimize the value of $\Delta G_{*O} - \Delta G_{*OH}$.[41-43] This has facilitated the exploration of electronic structure parameters that can serve as activity descriptors to assist in the screening of high-efficiency electrocatalysts. As a result, the e_g orbital occupancy has, in addition to the binding strengths of oxygen-containing intermediates, also been proposed as a descriptor to readily demonstrate the relationship of the structure-activity for the OER catalyst under alkaline conditions. This is mainly due to the participation of the e_g orbital of the transition metal cations on the catalysts surfaces in the formation of σ-bonding with surface adsorbates (**Fig. 3d**).[35, 44] Therefore, the e_g orbital occupancy can greatly affect the surface binding strengths of oxygen-containing intermediates on the transition metal cations and, as a result, the electrocatalytic performance, which has been confirmed by DFT calculations. In general, the binding strengths of oxygen-containing intermediates become stronger along with the decrease of the e_g occupancy, and vice versa; the value of e_g occupancy close to unity is beneficial for optimizing OER activity. [44, 45]

Despite the significant advancements made in understanding the nature of the OER process, there are still uncertainties regarding the underlying reaction mechanisms, and the capability of the AEM to fully explain the OER process has been challenged in a series of experimental studies.[46-48] More recently, a new lattice-oxygen-mediated mechanism (LOM) based on the redox process of lattice oxygen anions and the reversible formation of a surface

oxygen vacancies (V_O) in transition metal oxides has been proposed as shown in **Fig. 3c** and eqn (6) ~ (9), which eliminates the concerted proton-electron transfer processes of the traditional AEM.[36, 49, 50] The LOM has been experimentally supported by ^{18}O isotope detection of the reaction products and computationally validated via DFT calculations.[48]

$$*OH \rightarrow (V_O + *OO)^{\dagger} + H^+ + e^- \quad (6)$$

$$(V_O + *OO)^{\dagger} + H_2O \rightarrow O_2 + (V_O + *OH)^{\dagger} + H^+ + e^- \quad (7)$$

$$(V_O + *OH)^{\dagger} + H_2O \rightarrow (*H_{O\text{-site}} + *OH)^{\dagger} + H^+ + e^- \quad (8)$$

$$(*H_{O\text{-site}} + *OH)^{\dagger} \rightarrow *OH + H^+ + e^- \quad (9)$$

$()^{\dagger}$ indicates that adsorbates are calculated in the same supercell.

In the typical LOM process, the dehydrogenation of *OH on the oxygen anion sites produces *OO species and V_O (eqn (6)), then the *OO species evolves back to *OH while releasing O_2 and electrons (eqn (7)). During this step, the V_O are re-occupied by *OH and an adjacent surface lattice oxygen is protonated (eqn (8)). Lastly, *OH is regenerated during the deprotonation process (eqn (9)). It is important to note that this step does not involve the formation of *OOH by reacting with another OH^-, as occurs in the AEM. The underlying cause of the LOM corresponds to the intrinsic property of the metal-oxygen bond (i.e., covalency) in metal oxides, with a high covalency of the metal-oxygen bond favoring the LOM OER; moreover, the metal-oxygen bond can be tailored by regulating the electronic structure, and thereby controlling the OER mechanism of LOM (**Fig. 3e**).[36, 51] In fact, the covalency of the metal-oxygen bond is theoretically dependent on the band structure of the metal oxide.[36] Generally, for the traditional AEM in which the metal sites serve as the active centers for the OER, the metal *d*-band of the metal oxide situates on the top of the oxygen *p*-band. Otherwise, as the higher location of oxygen *p*-band with respect to the metal *d*-band, it is more likely that the electrons transfer from the oxygen *p*-band to the metal *d*-band accompanied with the formation of ligand holes, leading to the release of oxygen to form oxygen vacancies. In this case, the weak binding ability of metal sites (i.e., high covalency of metal-oxygen bond) will shift the OER mechanism from AEM to LOM.

2.2. Fundamental understanding of surface reconstruction

It has been widely found that the surface of most OER electrocatalysts undergoes significant physicochemical property (i.e., chemical composition and physical structure) changes under strong oxidizing conditions during the OER process, thereby resulting in the formation of a newly reconstructed surface.[9, 12, 52] Considering that the OER is a typical heterogeneous catalytic process which occurs at the surface of the employed electrocatalysts, the catalytic behavior (i.e., reactants/intermediates adsorption, activation process, and products desorption) is mainly determined by the physicochemical properties of the catalyst surface.[53] Therefore, a more thorough analysis of the derived surface and identification of structural differences between the derived surface and corresponding bulk counterparts at atomic resolution is of vital importance in confirming the actual active species for these transition-metal-based OER catalysts. Particularly, it is crucial to clarify the effects of surface reconstruction on the observed improvement of performance.

In general, the surface reconstruction process involves the oxidation of the electrocatalyst surface. Previous literature has revealed that significant oxidation peaks, occurring in potential regions well below that of evident water oxidation (i.e., OER onset potential), are often observed and are assigned to the catalyst surface oxidation.[54-58] During anodic polarization, prior to achieving oxygen evolution (e.g., typically 1.0 V ~ 1.5 V vs. RHE), the metal cations in the catalyst surface typically shift from their more stable lower valence states (0/+2) to their more electrocatalytically active higher valence states (+3/+4).[59, 60] These high-valence metal species have already been widely recognized as the true active components in OER electrocatalysis.[16, 45] In addition to this change in cation valence state, the electrocatalyst surface can also undergo a change in composition. Previous studies have shown that the enthalpy values for transition-metal-based oxides are generally more negative compared with those of transition-metal-based sulfides, nitrides, and phosphides, indicating that the oxides are the thermodynamically stable final product of most electrochemical processes in aqueous solution.[61, 62] Accordingly, it can be deduced that the surface of transition-metal-based electrocatalysts has a high probability of reconstructing into an oxide or (oxy)hydroxide during the OER process; several examples of this are presented in the following chapter..

Notably, the reconstruction level of the catalyst surface depends heavily on the applied

anodic overpotential driving the water oxidation, as the redox potentials of employed electrocatalysts, especially for transition-metal-based catalysts, are located within the range required to initiate OER; therefore, increasing the applied anodic overpotential will increase the kinetics and degree of surface reconstruction.[45, 63] In addition to the applied overpotential, adjusting variable electrocatalytic conditions, such as electrolyte pH, temperature, atmosphere, and pressure, can also affect the surface reconstruction process by modulating the cation oxidation potentials. Previous work has demonstrated that high pH conditions can be in favor of the surface reconstruction since the oxidation potential of metal cations negatively shifts, leading to the generation of more high-valence metal species and, as a result, significantly improving the electrocatalytic activity.[64]

Along with these external factors, recent experimental and computational studies have revealed that the structural features of electrocatalysts, such as structural defects and covalence of the metal-oxygen bond, also play non-negligible roles in surface reconstruction.[65, 66] It has been experimentally validated that a high concentration of structural defects can promote surface reconstruction, leading to the production of more high-valence metal species and increasing the OER activity.[65] In addition, some recently published work revealed that the lattice oxygen evolution reaction (LOER), which occurs via the LOM, may also participate in the surface-reconstruction of electrocatalysts in materials with high metal-oxygen covalency.[16] In this case, multiple steps including OH^- adsorption, catalyst dissolution and re-deposition, lattice oxygen evolution, and molecular O_2 release may be involved. Particularly, for the perovskite $Ba_{0.5}Sr_{0.5}Co_{0.8}Fe_{0.2}O_{3-\delta}$ (BSCF), an amorphous Co/Fe oxy(hydroxide) shell was formed as a result of the LOER and serves as the real catalytic species for OER.[66] These results suggest that the surface-reconstruction ability could be enhanced by elaborately tuning the local structure of the electrocatalyst surface.

3. Electrocatalysts possessing surface activation in alkaline media

To date, transition-metal-based catalysts have been recognized as promising candidates for the electrocatalytic water oxidation reaction in alkaline medium due to their earth abundance (low cost), environmental friendliness, and high catalytic performance and stability

capable of surpassing the precious-metal-based benchmark OER catalysts (IrO_2 and RuO_2).[67-70] Of particular interest, many Ni-, Co-, Fe- and Mn-based OER catalysts undergo a surface reconstruction process during anodic polarization to form highly active oxyhydroxide species, which have been confirmed as the real active phase for alkaline OER reactions.[9, 12, 28, 34, 71-74] Generally, these transition-metal-based OER catalysts can be classified into metal oxides, metal non-oxides, metal hydroxides, and metal alloys. These four categories of OER electrocatalysts will be discussed in detail below and are summarized in **Table 1-4**.

3.1 Metal oxides

Among the many materials that can catalyze the OER, transition metal oxides have been found to have high reactivity and excellent stability in alkaline conditions. Early in the 1980s, it was found that MnO_2 could electrocatalyze water splitting and produce O_2 in alkaline solution.[75, 76] Since then, Mn-based oxide electrocatalysts have been extensively studied. Najafpour and Sedigh first reported that many Mn oxides with different crystal structures, i.e., Mn_3O_4, α-Mn_2O_3, β-MnO_2, $CaMnO_3$, $Ca_2Mn_3O_8$, $CaMn_3O_6$, $CaMn_4O_8$ and K-birnessite, converted to the same stable layered Mn oxide phase during the OER, and that this layered Mn oxide should be the actual electrocatalytic phase for water oxidation.[77] Recently, this electrochemically-induced surface reconstruction has been observed for several different kinds of metal oxides under anodic potentials, namely, spinel-type oxides, perovskite-type oxides, rock salt-type oxides, as well as some other oxides, suggesting a general significance of the phenomenon and the crucial need to understand the surface reconstruction to identify the true active sites for OER electrocatalysts. In the following sections, we outline recent findings pertaining to metal-oxide catalysts which undergo surface reconstruction during the alkaline OER process. **Table 1** provides a representative summary of the recently reported metal-oxide electrocatalysts that exhibit surface reconstruction, including spinel-type oxides, perovskite-type oxides, rock salt-type oxides, and precious transition-metal oxides (IrO_2 and IrO_x).

3.1.1 Spinel-type oxides. Spinel-type oxides have been largely investigated as OER electrocatalysts due to their outstanding catalytic performance. This is, in part, due to their unique crystal structures, which consist of a face-centered cubic (FCC) array of oxygen with

1/8 of the tetrahedral sites and 1/2 of the octahedral sites filled.[78] Additionally, the spinel structure also exhibits a degree of inversion, resulting in the usage of $(A_{1-x}B_x)_{Td}(A_xB_{2-x})_{Oh}O_4$ (A, B = metal) as the typical chemical formula, where x represents the inversion degree of the spinel and can be equal to any value from 0 to 1.[78, 79] When x = 0, the structure is considered a normal spinel, i.e., AB_2O_4, in which all metal A ions exist in the +2 oxidation state (denoted A^{2+}) and occupy the tetrahedral sites, while the metal B ions with +3 oxidation states (denoted B^{3+}) occupy the octahedral sites. When x = 1, it is regarded as an inverse spinel, i.e., $B(AB)O_4$, in which half of the B^{3+} ions occupy the tetrahedral sites, while the remaining half, along with the A^{2+} ions, fill the octahedral sites. A special case is the complex spinel ($0 < x < 1$), which can be defined as an intermediate between the normal and inverse spinels, that is, the A^{2+} and B^{3+} ions simultaneously occupy both the octahedral and tetrahedral sites.

It is well known that chemical composition, crystal structure, morphology, valence state, etc., can be controlled and tuned using various material preparation methods. For preparing spinels, the most commonly reported synthesis methods include sol-gel, hydrothermal/solvothermal, electrodeposition, electrospinning, template synthesis, and precipitation, which usually require a calcination process to obtain the final spinel structure.[78] The calcination conditions are especially important as defects, such as oxygen vacancies, A-site defects, and B-site defects, can be generated and tuned by varying these conditions (temperature, atmosphere and time).[80, 81] This controlled creation of defects is often taken advantage of to significantly improve the physical/chemical properties and intrinsic activity of spinel materials.[78, 82, 83] For example, oxygen vacancies can be introduced by altering the spinel synthesis conditions; more specifically, they are easily produced at low temperatures in an oxygen-deficient environment. Additionally, the number of oxygen vacancies can be tuned by adjusting the size and shape (nanosheets, nanowires, nanoparticles, etc.) of spinel nanomaterials.[84-86] Oxygen vacancies are often desired in spinel electrocatalysts as they can facilitate the excitation of the delocalized electrons around the oxygen vacancy to the conduction band, potentially increasing the electrical conductivity of catalysts and thus boosting the electrocatalytic activity.[85, 86]

It is worth noting that spinels with different metal cation occupancies in the two geometric spaces (tetrahedral and octahedral sites) exhibit different catalytic activities owing to the

variety of electronic structures. Wei et al. presented a study in which the activity descriptor of 17 spinel oxides, including $Mn_xCo_{3-x}O_4$ (x = 2, 2.5, 3), $Li_xMn_2O_4$ (x = 0.7, 1), XCo_2O_4 (X = Co, Ni, Zn) and XFe_2O_4 (X = Mn, Co, Ni), was investigated.[87] They determined that, as a general principle, the e_g occupancy of the metal cation on the octahedral sites could be considered as the activity descriptor for OER catalytic activities. The OER volcano plot (**Fig. 4a**) demonstrates that the oxygen evolution activity is governed by both the e_g filling of octahedral metal cations and the occupancy of the active cation at the octahedral site. Additionally, the distributions of the metal cations can be altered via the synthesis method, which could also explain the differences in the catalytic activities for spinels which have the same chemical formula but were prepared by different approaches (**Fig. 4b**).

After observing the photosystem Ⅱ water-oxidizing complex (PS Ⅱ-WOC) and the M_4O_4 core (M = metal) in metal oxides of various compositions and allotropes, Dismukes et al. pointed out that in the spinel structure, Co_3O_4 for example, the Co_4O_4 cubanes formed by octahedral cobalt ions and oxygen anions might act as the active sites for the four-electron-transfer OER.[88] They found that, through the removal of Li cations (tetrahedral site), the catalytically inactive spinel $LiMn_2O_4$ could be reconstructed into the catalytically active λ-MnO_2 phase, which is organized into cubical Mn_4O_4 subunits. In another study focused on the active sites for spinel OER electrocatalysts, Maiyalagan et al. observed that in the low-temperature-formed spinel-type delithiated $LiCoO_2$ (denoted LT-$LiCoO_2$, in which the Co^{3+} ions occupy the octahedral sites, hereafter denoted $Co^{3+}{}_{Oh}$), some of the $Co^{3+}{}_{Oh}$ ions would be oxidized into Co^{4+} during the OER process; this resulted in the presence of mixed-valent $Co^{3+/4+}$ ions.[89] In contrast, the $LiCoO_2$ fabricated at high temperature (denoted HT-$LiCoO_2$) adopted a rock salt structure, where the Li^+ and Co^{3+} ions appeared in alternate planes of the crystal structure because of the significant differences of size and charge between them. As shown in the cyclic voltammetry (CV) scan (**Fig. 4c**), Co_3O_4 showed a quasi-reversible redox couple (CoO_2/CoOOH) prior to the OER onset potential, while both the LT-$LiCoO_2$ and the HT-$LiCoO_2$ displayed two distinct oxidation peaks, of which the $Co^{3+/4+}$ oxidation/reduction was accompanied by the extraction/insertion of Li^+/H^+ from/into two different lattice sites. Notably, the oxidation peak in LT-$LiCoO_2$ appeared at a lower potential (1.43 V) than that of HT-$LiCoO_2$ (1.49 V) despite both catalysts initially having the same Co content and oxidation

state; this observation emphasizes the effect of crystal structure on the surface reconstruction process. Meanwhile, the second anodic peak in LT-$LiCoO_2$ was much weaker; this could possibly be attributed to the generation of defects during the low temperature formation of the lithiated spinel structure which caused a lower lithium diffusion rate in LT-$LiCoO_2$. In comparison, HT-$LiCoO_2$ with the well-formed and well-ordered layered structure had a higher lithium diffusion rate. Furthermore, despite having the same spinel framework, Co_3O_4 exhibited much lower OER activity than LT-$LiCoO_2$. This could be ascribed to the presence of Co^{2+} ions in the tetrahedral sites (denoted $Co^{2+}{}_{Td}$) of Co_3O_4, which must be oxidized before oxidization of the $Co^{3+}{}_{Oh}$ into Co^{4+}. By assuming that OER occurred via the lattice-oxygen-mediated mechanism (LOM), this difference in electrocatalytic activity can be further explained. O_2 formation would be prohibited at the tetrahedral sites because of the lack of bridging oxos between the adjacent tetrahedral metal centers. Additionally, the high OER activity of the LT-$LiCoO_2$ was strongly related to the Co_4O_4 cubane structure with Co–O–Co bonds, in which the direct coupling on adjacent octahedral $Co^{3+/4+}$ ions could promote the formation of O–O bonds, resulting in an easier release of O_2 (as shown in **Fig. 4d**).

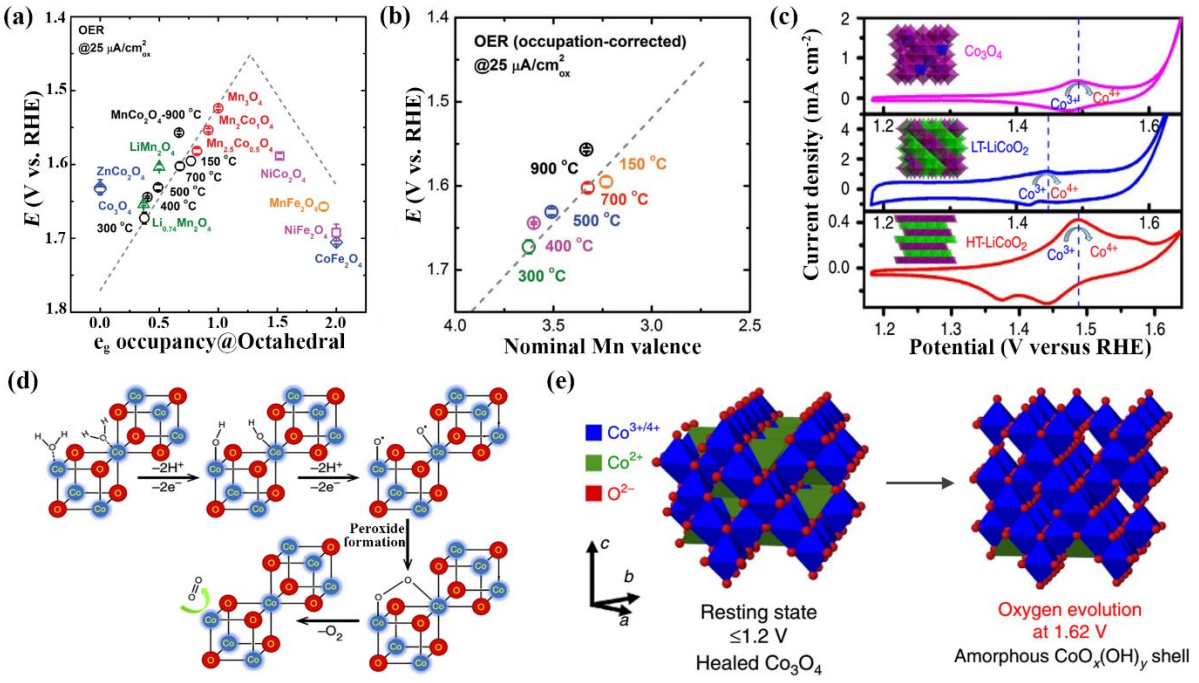

Fig. 4 (a) Correlation between OER activity and e_g occupancy of 17 spinels (the active cation at the octahedral site). (b) Correlation between OER activity and nominal Mn valence state of

various $MnCo_2O_4$ spinels (at 25 μA cm^{-2}_{Oxi}). Reproduced with permission from ref. 87. Copyright 2017, Wiley-VCH. (c) Cyclic voltammetry (CV) curves of Co_3O_4, LT-$LiCoO_2$ and HT-$LiCoO_2$ in 0.1 M KOH with a scan rate of 5 mV s^{-1}. Inset, the purple, blue and green colors in the structures represent the polyhedra of Co^{3+}, Co^{2+} and Li^+ ions, respectively. (d) OER mechanism based on LT-$LiCoO_2$ with a Co_4O_4 cubane unit. Adapted with permission from ref. 89. Copyright 2014, Springer Nature. (e) Surface structure transformation of spinel Co_3O_4 to a sub-nanometer shell of $CoO_x(OH)_y$ with edge-sharing Co octahedral structure under OER condition. Reproduced with permission from ref. 90. Copyright 2015, Springer Nature.

Recently, taking advantage of operando/in situ studies, the dynamically changing chemical environment of spinel metal cations during the OER process was investigated. Wang et al., utilizing operando X-ray absorption spectroscopy (XAS), revealed that cobalt ions located in the tetrahedral sites of spinel Co_3O_4 acted as the primary OER active site.[91] As mentioned previously, two types of cobalt ions, Co^{2+}_{Td} and Co^{3+}_{Oh}, exist in spinel Co_3O_4, both occupying different geometric spaces. To identify the active site in specific geometric spaces (tetrahedral or octahedral), $ZnCo_2O_4$ (Co^{3+}_{Oh}) and $CoAl_2O_4$ (Co^{2+}_{Td}) were synthesized via a facile ion-substitution strategy and compared to Co_3O_4. The operando Co *K*-edge extended X-ray absorption fine structure (EXAFS) results showed that for both $CoAl_2O_4$ and Co_3O_4, the Co–O bond experienced shrinkage in length, indicating an incomplete oxidation of the catalyst surface. Additionally, Co K-edge X-ray absorption near edge structure (XANES) results revealed an increase in cobalt valence state for $CoAl_2O_4$ and Co_3O_4, while the Co^{3+}_{Oh} predominated $ZnCo_2O_4$ remained stable with no oxidation. This suggested that only the Co^{2+}_{Td} with low oxidation state was capable of releasing electrons under anodic potentials, thus promoting its interaction with oxygen intermediates to produce the CoOOH intermediate species. Similarly, the surface of the Co_3O_4 reconstructed into a sub-nanometer amorphous $CoO_x(OH)_y$ shell with edge-sharing Co octahedral structure (**Fig. 4e**) under OER conditions in neutral electrolyte was uncovered by Bergmann and co-workers.[90] From the Co *K*-edge EXAFS spectra, three major peaks representing absorber-backscatterer distances were visible for the Co_3O_4, of which the second and third peak correspond to the Co–Co distances for edge-sharing Co octahedral (~2.85 Å) and corner-sharing Co octahedral and tetrahedral (~3.36 Å),

respectively. Obviously, the Co coordination variations along the OER proceeding could be clearly confirmed, where negative shifts of the peaks signified more generation of edge-sharing Co octahedral sites (from 1.0 to 1.62 V vs. RHE). This indicated that the Co^{2+}_{Td} ions in Co_3O_4 may get oxidized to +3 and their coordination would be changed from tetrahedral to octahedral. Simultaneously, the amorphous $CoO_x(OH)_y$ with edge-sharing Co octahedral structure and Co^{4+} ions originated from the oxidation of Co^{3+}_{Oh} was formed via deprotonation of OH bridges along with the increasing electrode potentials. Finally, they highlighted the importance of the formation of the amorphous $CoO_x(OH)_y$ with edge-sharing Co octahedral structure at the surface for oxygen evolution activity on Co_3O_4. However, the discussion on the geometric spaces (tetrahedral and octahedral) that the formation of oxyhydroxides takes place at, is still under debate. Other researchers also observed that the OER can take place at both tetrahedral and octahedral sites in some spinels; for example, spinel $NiCo_2O_4$ produces two kinds of active centers, Ni^{2+}/Ni^{3+} and Co^{2+}/Co^{3+}, during the OER.[92] Briefly, the formation of the oxyhydroxides species with oxo-bridged octahedral metal cations on the catalysts surfaces is essential in maximizing the OER reactivity for spinel oxides, which requires future in-depth investigation to shed more light on.

3.1.2 Perovskite-type oxides. Perovskite-type oxides, generally formed in the structure of ABO_3, are a frequently encountered structure in electrochemical studies due to their flexibility of both physical, chemical and catalytic properties.[93, 94] This structure can consist of a large proportion of the metallic ions in the periodic table, of which the A-site is able to accommodate rare-earth or alkaline-earth metals and the B-site is prone to be transition metals. **Fig. 5a** demonstrates the crystal structure of perovskite, of which B cations with smaller radii occupy the center of oxygen octahedral that share corners to form a three-dimensional framework, and A cations with relatively larger radii are located in the cavities created by eight corner-sharing BO_6 octahedral.[94] Besides the typical perovskite-type catalysts, such as $Ba_{0.5}Sr_{0.5}Co_{0.8}Fe_{0.2}O_{3-\delta}$,[44, 66, 95] $La_x(Ba_{0.5}Sr_{0.5})_{1-x}Co_{0.8}Fe_{0.2}O_{3-\delta}$,[96] $LaCoO_3$,[97, 98] $LaCo_{0.8}Fe_{0.2}O_{3-\delta}$,[99, 100] $SrCoO_3$,[101, 102] and $SrNb_{0.1}Co_{0.7}Fe_{0.2}O_{3-\delta}$,[103, 104] the double-perovskite $(Ln_{0.5}Ba_{0.5})CoO_{3-\delta}$ (Ln = Pr, Sm, Gd, and Ho) and the quadruple-perovskite $CaCu_3Fe_4O_{12}$ were also found to have potential as highly active catalysts.[105-107]

In general, there are several ways to synthesize perovskite oxides, such as sol-gel, hydrothermal/solvothermal, solid-state, co-precipitation, and other methodologies.[93, 108] Regardless of the process used, however, further harsh, high-temperature processing (≥ 600 ^{o}C) is required for the crystallization of perovskite oxides. This obligatory synthesis step results in large particle sizes/aggregations, low surface area, and thus low mass activity, which is detrimental to the enhancement of their electrocatalytic activities.[108] Therefore, the exploration of new preparation approaches to achieve the perovskites which exhibit a combination of high mass activity, intrinsic activity, and stability, is one of the key focuses for further development of perovskite-type oxides OER catalysts.

To date, most attention have been paid on investigating the OER mechanism of perovskite-type oxide catalysts, identifying reliable descriptors of their OER activity, and improving their catalytic activities to the utmost extent. Based on experimental results and molecular orbital principles, Shao-Horns' group proposed the e_g occupancy of surface cations to demonstrate the OER activities, and identified $Ba_{0.5}Sr_{0.5}Co_{0.8}Fe_{0.2}O_{3-\delta}$ as a group of catalysts with landmark intrinsic catalytic activity at least one order of magnitude higher in comparison to that of state-of-the-art IrO_2 (**Fig. 5b**).[44] In a later study, they proved that $Ba_{0.5}Sr_{0.5}Co_{0.8}Fe_{0.2}O_{3-\delta}$ underwent surface reconstruction, specifically, the amorphization of its surface, during anodic polarization.[95] Compared to the completely crystalline surface of as-prepared $Ba_{0.5}Sr_{0.5}Co_{0.8}Fe_{0.2}O_{3-\delta}$, which displayed a corner-sharing octahedral structure (**Fig. 5c**), fast Fourier transform (FFT) analysis of a high-resolution transmission electron microscopy (HRTEM) image collected from the amorphous $Ba_{0.5}Sr_{0.5}Co_{0.8}Fe_{0.2}O_{3-\delta}$ surface after 5 CV cycles showed a bright diffuse ring with ~2.8 Å spacing (**Fig. 5d**), which accounted for the edge-sharing octahedral structures occupied by cobalt and iron cations, indicating the change of the atomic structure of the catalyst surface under anodic conditions. They also pointed out that the amorphous regions produced during water oxidation potentially increased effective active area, thus increasing the OER activity 4 ~ 5 times.

In a separate report, assisted with operando XAS measurements, Fabbri and co-workers captured the dynamic self-reconstruction on the surface of perovskite $Ba_{0.5}Sr_{0.5}Co_{0.8}Fe_{0.2}O_{3-\delta}$ under alkaline oxygen evolution operating conditions.[66] The self-

assembled formation of a metal oxyhydroxide layer was revealed, and the formation mechanism of the high-activity surface layer (CoO(OH) and FeO(OH)) accompanied with the dynamically changed local electronic and geometric structure during the OER was elaborated upon.[66] After performing operando XAS, holding the potential at intervals from 1.2 to 1.55 V vs. RHE in 0.1 M KOH, a significantly increased Co oxidation state at 1.425 V vs. RHE was observed in the Co K-edge XANES. Meanwhile, the evidence for the transformation into a (Co/Fe)O(OH) layer with edge-sharing polyhedral structure was provided in the EXAFS. The OER activity was also found to be positively correlated with the degree of the rising Co oxidation state and the local atomic structure variation. Further insight into this surface reconstruction was gained by analyzing the inductively coupled plasma optical emission spectrometry (ICP-OES) results, from which it was observed that, in the perovskite $Ba_{0.5}Sr_{0.5}Co_{0.8}Fe_{0.2}O_{3-\delta}$ catalyst, there was significant Ba and Sr cations leaching present, while Co and Fe dissolution was minimal, thus leading to a Co/Fe-enriched surface layer. The authors proposed that the formation of Co/Fe oxyhydroxide layer may be originated from the lattice oxygen evolution reaction (LOER) (**Fig. 5e**). Generally, when the OER occurs, the LOER also takes place. The LOER reaction on the perovskite oxides catalyst is proposed as follows (eqn (10)):

$$ABO_{3-\delta} + OH^- \leftrightarrow BO(OH) + A^{2+} + \frac{2-\delta}{2} O_2 + 3e^- \quad (10)$$

The highly soluble A-site cations (herein Ba^{2+} and Sr^{2+} cations) would easily leach into the electrolyte as triggered by the LOER, while the B-site cations (herein Co^{2-3+} and Fe^{2-3+} cations) is restricted to dissolve, thereby leading to the growth of an oxyhydroxide layer. Simultaneously, the oxygen would evolve from the electrochemical system that consisted of the electrolyte ions (i.e., OH^- ions) and the metal oxyhydroxide lattice, while the OH^- ions would replenish the lattice oxygen through LOM. Thus, for the perovskite $Ba_{0.5}Sr_{0.5}Co_{0.8}Fe_{0.2}O_{3-\delta}$ catalyst-based OER system, a stable dynamic cycle including the pristine perovskite structure and the self-assembled formation of the active oxyhydroxide surface layer, is established.

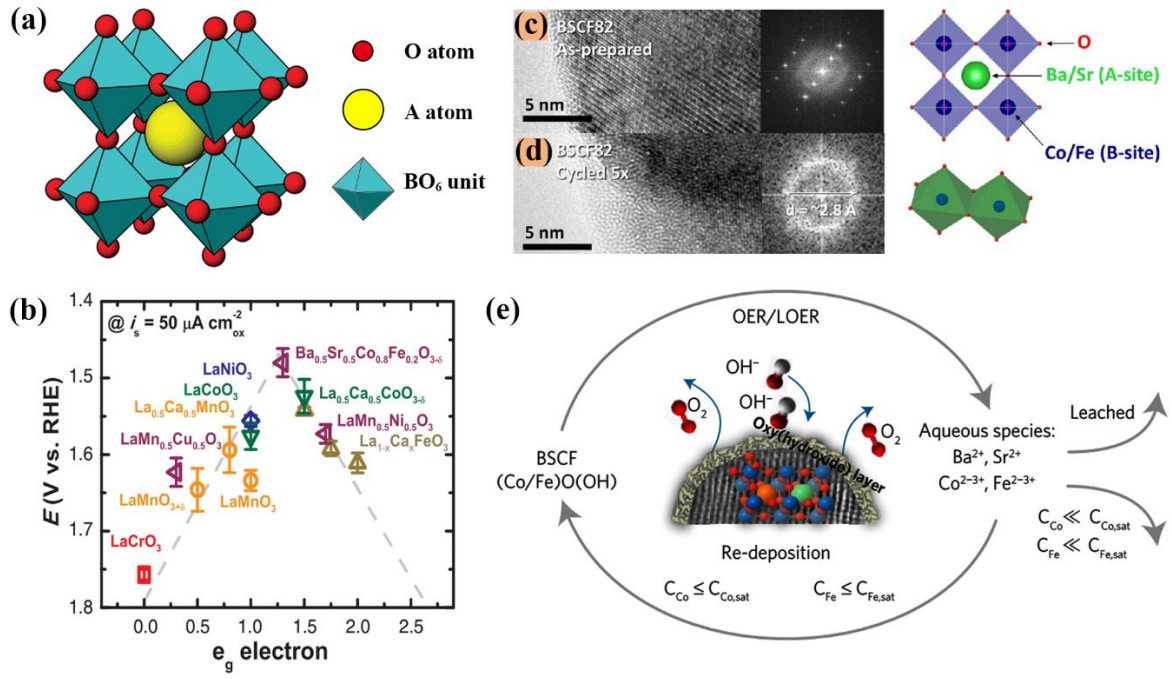

Fig. 5 (a) Perovskite with the ABO_3 structure. Reproduced with permission from ref. 94. Copyright 2012, Royal Society of Chemistry. (b) Correlation between the OER activity and the e_g electron occupancy based on the transition metal oxides. Reproduced with permission from ref. 44. Copyright 2011, American Association for the Advancement of Science. (c, d) High-resolution transmission electron microscopy (HRTEM) images and corresponding fast Fourier transforms (FFT) of the surfaces of as-prepared $Ba_{0.5}Sr_{0.5}Co_{0.8}Fe_{0.2}O_{3-\delta}$ (BSCF82) powder and BSCF82 electrodes after 5 CV cycles (from 1.1 to 1.7 V *vs.* RHE in O_2-saturated 0.1 M KOH electrolyte at 10 mV/s), respectively. Reproduced with permission from ref. 95. Copyright 2012, American Chemical Society. (e) Schematic illustration of the formation mechanism of the self-assembled active surface layer, (Co/Fe)O(OH). Reproduced with permission from ref. 66. Copyright 2017, Springer Nature.

Some studies have found that OER conditions including electrolyte pH, applied potential, temperature, etc., can alter the initiation potentials and kinetics of surface reconstruction.[72] Particularly, it has been well accepted that surface reconstruction is more likely to occur in alkaline electrolyte with high pH values.[64] This may be due, in part, to the tendency of transition-metal-based electrocatalysts to be easily corroded and destroyed under strong acidic oxidation conditions.[52] However, the reaction systems in more-recent commercial water

electrolysis technologies are primarily conducted in acidic electrolyte and center around the use of Ir, which is considered a unique metal for its relatively long survival time under the rigorous, corrosive conditions created by the acidic electrolyte.[71] Ir-based perovskites have been investigated as exceptional electrocatalysts under acidic OER conditions (0.1 M $HClO_4$).[109] As reported by Xu et al., during OER testing, Ir in $SrCo_{0.9}Ir_{0.1}O_{3-\delta}$ catalyst transformed into the highly active IrO_xH_y species with a corner-shared IrO_6 octahedron structure and increased oxidation state (from Ir^{3+} to Ir^{5+}), while Sr and Co dissolved into the electrolyte.[110] Correspondingly, the intrinsic activity of Ir in the reconstructed IrO_xH_y was found to be more than double that of Ir in IrO_2, as evidenced by the higher turnover frequency (TOF) of Ir achieved in the reconstructed species.

3.1.3 Rock salt-type oxides. Rock salt-type oxides (also called NaCl-type) with the general formula AO, of which A cations are alkali metals or transition metals (i.e., NiO, CoO, etc.), exhibit attractive OER.[111, 112] The structure of rock salt-type oxides comprises metal cations that are octahedrally coordinated by oxygen atoms, forming a three-dimensional network of edge-sharing octahedral.[112] Various synthesis methods for rock salt-type monometallic oxides have been described in previous literature, such as sol-gel, hydrothermal/solvothermal, electrodeposition, and several others.[113] In practice, additional annealing treatment under high-temperature conditions is needed to form crystalline oxides, making it difficult to synthesize nanoparticles, which are often desirable in electrocatalysis, without irreversible agglomeration.[113] Moreover, rock salt-type bimetallic oxides, such as $NiCoO_2$, can be formed by replacing Co^{2+} in the CoO rock salt structure with Ni^{2+}, since both cations have similar radii.[114, 115] It is difficult to obtain a single-phase rock salt-type bimetallic oxide through classical crystallization pathways, but success has been found using thermodynamically controlled synthesis methods. For example, Xiao and Yang reported a bio-inspired approach for the preparation of single phase $Co_xNi_{1-x}O$ formed in different molar ratios of Co/Ni ($0 \leq x \leq 1$), in which the disordered and hydrated precursors would be crystallized into the rock salt-type crystal structure via thermal decomposition.[114]

Similarly to the spinel and perovskite structures, rock salt-type electrocatalysts generally undergo a surface reconstruction process involving a phase transformation when exposed to

water oxidation conditions. Interestingly, in contrast to the extensively reported observation that mixed metal oxides, such as spinel $NiCo_2O_4$,[116] exhibit higher OER activities than their monometallic oxides counterparts, Boettcher et al. found that pure NiO_x catalyst films possessed higher OER activity than Ni/Co-based mixed rock salt-type oxides, with the activity of $Ni_yCo_{1-y}O_x$ catalysts decreasing as the Co content was increased.[117] This behavior was ascribed to the suppression of electrocatalyst surface reconstruction into the highly active oxyhydroxide species as more Co was incorporated, which was measured by the integrating the total charge under the Ni^{2+} oxidation peak in CV plots (**Fig. 6a**).[117] However, it is important to note that determining the amount of reconstructed oxyhydroxide species solely through this calculation is difficult; therefore, in situ and ex situ measurements such as in situ XAS, in situ Raman, ex situ HRTEM, etc., should be utilized to perform a more in-depth investigation on the dynamic process during the surface reconstruction of rock-salt type oxide electrocatalysts.

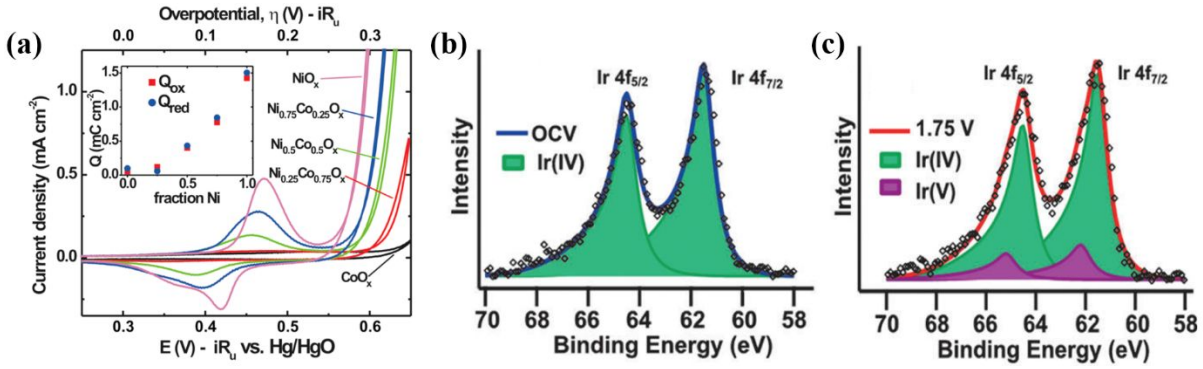

Fig. 6 (a) CV curves of the conditioned NiO_x, $Ni_yCo_{1-y}O_x$, and CoO_x films in 1.0 M KOH at 20 mV s^{-1} scanning rate. Inset, correlation between integrated charge Q for the redox processes and Ni content. Reproduced with permission from ref. 117. Copyright 2012, American Chemical Society. (b) Curve-fitted Ir 4f XPS spectrum of iridium oxide at open circuit voltage (OCV), of which the green regions represent Ir^{4+}. (c) Curve-fitted Ir 4f XPS spectrum of iridium oxide at 1.75 V, of which the green and purple regions represent Ir^{4+} and Ir^{5+}, respectively. Reproduced with permission from ref. 118. Copyright 2014, Wiley-VCH.

3.1.4 Other oxides. In addition to the aforementioned three types of non-precious transition-metal oxides (spinel, perovskite and rock salt) that undergo surface reconstruction during the OER process, changes in the surface speciation of Ir-based oxides, such as IrO_x,

have also been revealed. Pavlovic et al. confirmed the structure of in situ formed square pyramidal Ir–O species under the alkaline OER conditions by utilizing in situ Raman spectroscopy.[119] Moreover, based on theoretical calculations, it was highly suggested that Ir cations octahedrally coordinated by oxygen are the active sites enabling the OER. Beyond alkaline and acidic OER, neutral OER is of great importance to the development of practical electrocatalysis technology in an environmentally friendly and low cost way. However, the huge overpotentials in neutral solutions greatly limit its practical applications. Nevertheless, the surface reconstructions induced at high anodic potentials have been proven to favor the production of important intermediates in neutral electrolyte, thus facilitating oxygen evolution. For example, Nilsson et al. reported the dynamic change in chemical valence of Ir ions on the iridium oxide surface in the water mediate during the OER through an operando measurement based on ambient-pressure X-ray photoelectron spectroscopy (APXPS), which, in contrast to normal XPS which has a much deeper detecting depth, confines the characterization detecting depth to just the surface of the catalyst.[118] From operando electrochemical APXPS results, a chemical shift in binding energy and the presence of two distinct Ir oxidation states (Ir^{4+} and Ir^{5+}) were observed under OER conditions (**Fig. 6c**) when compared to data collected under open circuit conditions (OCP) (**Fig. 6b**), demonstrating that the Ir ions transformed into a higher oxidation state. Meanwhile, the authors pointed out that the growth of high-oxidation-state Ir species is confined to the catalyst surface layer, as no evidence provided by ordinary XPS measurements. From O 1s XPS spectra taken from OCP to OER conditions, the reduction of surface-adsorbed hydroxide into oxygen on the catalyst surface was detected, implying the occurrence of a deprotonation process during OER. As postulated by Rossmeisl et al., the high-efficiency OER could be ascribed to the following: the high-oxidation-state Ir (Ir^{5+}) with strong oxygen binding ability is prone to facilitate the formation of the OOH intermediate, resulting in enhanced oxygen evolution.[120]

Overall, the electrocatalytic activity of metal oxides are closely related to the local structure, metal oxidation state, and crystallinity along with the OER proceeding. Future research on the surface reconstruction of these complex transition-metal-based catalysts is still needed in order to enhance the fundamental understanding of their electrochemical behavior.

Table 1. Summary of the synthesis methods, surface reconstruction potential, original oxidation state, reconstructed oxidation state, and measurements for analyzing the surface reconstruction of the metal oxide catalysts, containing spinel-type oxides, perovskite-type oxides, and rock salt-type oxides, as well as the precious transition-metal oxides (IrO_2 and IrO_x) during the OER.

Catalyst	Synthesis method	Surface reconstruction potential (V vs. RHE)	Original oxidation state/structure	Reconstructed oxidation state/surface species/structure	Measurements for detecting surface reconstruction	Application (electrolyte)	Ref.
Spinel-type oxides							
$LiCoO_2$ (LT-$LiCoO_2$)	Solid state	1.43 V	Co^{3+}	Co^{4+}	CV	OER (0.1 M KOH)	89
Co_3O_4	Sol-gel	1.49 V	$Co^{2+}{}_{Td}$	CoOOH	operando XAS	OER (0.1 M KOH)	91
Co_3O_4	Calcination	1.41 V (first) 1.54 V (second)	Co^{2+} (first) Co^{3+} (second)	Co^{3+} (first) Co^{4+} (second)	in situ GIXRD[a] and quasi-in situ XAS	OER (0.1 M KPi)	90
$NiCo_2O_4$	Electrodeposition and annealing	~0.40 V vs. Hg/HgO ~0.45 vs. Hg/HgO	Ni^{2+} (first) Co^{2+} (second)	Ni^{3+} (first) Co^{3+} (second)	CV	OER (1.0 M KPi)	92
Perovskite-type oxides							
$Ba_{0.5}Sr_{0.5}Co_{0.8}Fe_{0.2}O_{3-\delta}$	Nitrate combustion method	~1.50 V	corner-sharing octahedral	cobalt and iron cations-contained edge-sharing octahedral	ex situ TEM and ex situ Raman	OER (0.1 M KOH)	95
$Ba_{0.5}Sr_{0.5}Co_{0.8}Fe_{0.2}O_{3-\delta}$	Flame spray	1.425 V	Co^{2+} and Fe^{2+} in perovskite structure	(Co/Fe)O(OH) in edge-sharing polyhedra	operando XAS	OER (0.1 M KOH)	66
$La_{1.1}Sr_{0.9}Ni_{0.8}Fe_{0.2}O_{4\pm\delta}$ (LSN ~ LSF, Fe from 0% to 100%)	Modified Pechini method, crystallization and annealing	1.385 ~ 1.524V	Ni^{2+} and Fe^{2+}	$Ni^{3.46\text{-}3.95+}$ and Fe^{4+} (Ni–Fe oxyhydroxides)	ex situ Mössbauer spectroscopy	OER (0.1 M KOH)	121
$LaCo_{0.8}Fe_{0.2}O_{3-\delta}$ (LCF700)	Molten salt method	1.52 V	Mainly in Co^0 state (Co-Co/Fe coordination	Mainly in Co^{3+} and Co^{4+} (edge-sharing trivalent cobalt oxides/hydroxides	operando XAS	OER (0.1 M KOH)	100

			in cobalt metal or Co/Fe alloy)	(Co/Fe)O(OH))			
$SrIrO_3$	Polymerized complex	0.84 V (first) 1.15 V(second)	Ir^{3+} (first) Ir^{4+} (second)	Ir^{4+} (first) Ir^{5+} (second)	ex situ XRD and ex situ XPS	OER (0.1 M $HClO_4$)	122
$SrCo_{0.9}Ir_{0.1}O_{3-\delta}$	Solid state	1.00 V ($Ir^{3+/4+}$) 1.00 V ($Co^{2+/3+}$) 1.20 V($Ir^{4+/5+}$)	corner-shared IrO_6 octahedrons	Amorphous IrO_xH_y phase with corner-shared IrO_6 octahedrons	ex situ XPS and ex situ XAS	OER (0.1 M $HClO_4$)	110
Rock salt-type oxides							
NiO_x	Solution synthesis and annealing	472 mV (vs. Hg/HgO)	Ni^{2+}	Ni^{3+} (NiOOH)	ex situ XPS	OER (1.0 M KOH)	117
Ni/NiO	Solvothermal and battery conversion chemistry	1.40 V	Ni^{2+}	$Ni^{3+/4+}$ (Ni oxyhydroxide)	operando UV-Vis, ex situ XAS and ex situ synchrotron XRD	OER (1.0 M KOH)	123
$NiCoO_2$	Hydrothermal	1.35 V	Ni^{2+} and Co^{2+}	Ni^{3+} and $Co^{3+/4+}$ (NiOOH and $CoOOH/CoO_2$)	LSV[a]	OER (0.1 M KOH)	57
NiCo@ $NiCoO_2$	Hydrothermal and calcination	≈1.40 V	Ni^{2+} and Co^{2+}	Ni^{3+} and Co^{3+}	LSV[a]	OER (1.0 M KOH)	116
Precious transition-metal oxides							
IrO_2	One-step dropcasting method	Not available	Ir^{4+}	Ir^{5+}	in situ APXPS	OER (H_2O)	118
IrO_x	Electrodeposition	Not available	Edge-sharing IrO_6 octahedral	a square pyramidal ‘‘Ir–O’’ species	in situ Raman	OER (0.1 M NaOH)	119

[a] Abbreviations: GIXRD, grazing-incident X-ray diffraction; LSV, linear sweep voltammetry.

3.2 Metal non-oxides

In contrast to metal oxides which sometimes show inherently limited conductivity and catalytic kinetics, transition metal non-oxides with the general formula A_xZ_y, where A is transition metals, such as Ni, Co, Fe, Cu or Mo, and Z is S, Se, N, P, B, C or F, lack such intrinsic restrictions. Because metal non-oxides possess metal-like conductivity, are relatively insensitive to harsh electrochemical conditions (strong acid/alkaline), and exhibit outstanding electrochemical activities, they have attracted an increasing number of researchers to explore their potential as water splitting catalysts.[124] Notably, transition metal non-oxides are generally

less thermodynamically stable under anodic potentials than transition metal oxides; therefore, metal sulfides (MS), metal selenides (MSe), metal nitrides (MN), metal phosphides (MP), metal borides (MB), metal carbides (MC), and metal fluorides (MF) can more easily undergo surface reconstruction, forming their corresponding active species, under the alkaline environment and high anodic potential of the OER process.[12, 52, 72, 74] Interestingly , unlike the surface reconstruction that occurs on metal oxides, it has been found that the non-oxide elements (Z in A_xZ_y) are depleted during anodic polarization and subsequently replaced by oxygen, thus resulting in the surface reconstruction of the metal non-oxides into metal oxides/(oxy)hydroxides.[11, 125] In the following sections, we outline recent findings pertaining to metal non-oxide catalysts which undergo surface reconstruction during the alkaline OER process. **Table 2** provides a representative summary of the recently reported metal non-oxide electrocatalysts that exhibit surface reconstruction, including metal chalcogenides (MS and MSe), metal pnictides (MN and MP), metal borides (MB), metal carbides (MC), and metal fluorides (MF).

3.2.1 Metal chalcogenides. Both S and Se are in group VIA of the periodic table (**Fig. 1**), meaning they have the same outermost electron configuration and thus show similar activities for OER.[10, 124] Although Te also resides in group VIA, metal tellurides are introduced in a later section focused on metal alloys due to the strong metallic property of Te. Chalcogenide biocatalysts, such as nitrogenase and hydrogenase, exhibit fantastic catalytic performance in their natural environment but not in acidic or alkaline media.[126-131] This inspired researchers to investigate metal chalcogenides as potentially promising electrocatalysts that could circumvent the obstacle of poor stability under extreme conditions (acidic/alkaline electrolyte) limiting the use of similar biocatalysts. Chalcogenides with various morphology ranging from nanoparticle, nanosphere, nanorod, nanoplate, nanoribbon to polyhedron, and with controllable shapes, sizes and phase have been successfully fabricated via different strategies, such as liquid exfoliation, hot injection, hydrothermal/solvothermal, electrospinning, and so forth.[132] Typically, layered chalcogenides, such as MoS_2, which possess superb conductivity and large exposed active edges, have attracted more attention.[124] However, similar to the fabrication of graphene, an exfoliation process is required to produce single or few layers from the original bulk

chalcogenide, ultimately limiting their practical application.[124]

Admittedly, the structure reconstruction with the formation of highly active oxides/oxyhydroxides would take place in metal chalcogenides during the OER. More attention has been focused on the direct observation of the electrocatalytic oxygen evolution process, especially the utilization of nanoscale surface characterizations to determine the structure transition mechanism as well as the true active species/sites for boosting OER. For example, taking advantage of the in situ electrochemical oxidation, Cui et al. realized the synthesis of in situ electrochemically tuned transition metal oxides (ECT-TMOs, including CoO, $Co_{0.5}Fe_{0.5}O$, $Co_{0.37}Ni_{0.26}Fe_{0.37}O$) through CV sweeping the corresponding transition metal sulfides (TMSs, including CoS_2, $Co_{0.5}Fe_{0.5}S_2$, $Co_{0.37}Ni_{0.26}Fe_{0.37}S_2$) in alkaline electrolyte.[18] After the modulation via in situ electrochemical oxidation process, numerous nanopores were created on the ECT-TMOs; additionally, an increased amount of electrocatalytically active sites on the ECT-TMOs were achieved, which led to the significantly improved OER activity. For example, ECT-$Co_{0.37}Ni_{0.26}Fe_{0.37}O$ showed a much lower overpotential (at current density of 10 mA cm^{-2}) of 232 mV than the directly-synthesized $Co_{0.37}Ni_{0.26}Fe_{0.37}O$ (299 mV). After this work, Xu et al. reported a previously unknown selenide, nickel iron diselenide ($Ni_xFe_{1-x}Se_2$), that could act as template precursor and then in situ generated the corresponding metal oxides ($Ni_xFe_{1-x}Se_2$-DO) under OER conditions.[21] Likewise, the formation of tiny nanopores and smaller particle size were observed in $Ni_xFe_{1-x}Se_2$-DO, resulting in the production of a higher number of active edge sites, which demonstrated a superior catalytic activity with an overpotential of only 195 mV at 10 mA cm^{-2} current density. Revealingly, these two prospective studies adopted the metal chalcogenides as precursors to achieve the corresponding metal oxides via the in situ electrochemical reconstruction, which not only provides a novel method to synthesize high-efficiency oxides/hydroxides OER catalysts that are difficult to realize to by common approaches, but also implies the vitally important function of in situ oxidation for improving water oxidation performance.

A gradual reconstruction of amorphous CoS_x into CoOOH via a $Co(OH)_2$ intermediate ($CoS_x \rightarrow Co(OH)_2 \rightarrow CoOOH$) in the OER process has been captured through in situ and ex situ technologies by Fan and co-workers.[20] A morphology transformation from the initial rhombic dodecahedral particles, comprising amorphous CoS_x, to numerous nanoplates,

comprising polycrystalline cobalt oxide/(oxy)hydroxide, was observed via ex situ scanning electron microscopy (SEM) (**Fig. 7a** and **7b**). Then, in situ HRTEM (**Fig. 7c** and **7d**) and in situ Fourier-transform infrared spectroscopy (FTIR) were carried out to verify that CoOOH is the final phase, is actual catalytic species responsible for the initiation of oxygen evolution, and that the observed conversion from CoS_x to CoOOH is irreversible after experiencing OER process. The complete loss of S on the catalyst surface was confirmed by ex situ XPS (**Fig. 7e**). The ex situ XANES spectrum further suggested that Co^{3+} predominated as the final oxidation state of the surface species, implying the conversion of CoS_x into Co^{3+} oxide/(oxy)hydroxide. Moreover, compared to the directly-synthesized CoOOH (315 mV overpotential at 10 mA cm^{-2} and 61 mV dec^{-1} Tafel slope), the CoS_x–derived CoOOH showed a relatively larger overpotential (396 mV) but similar Tafel slope (69 mV dec^{-1}), indicating that the active species are the same in both cases and the larger amount of active CoOOH in the directly-synthesized samples is responsible for the higher OER activity. It was also postulated that $CoSe_2$ could produce the same active species, CoOOH, during the OER. Therefore, this study verified surface-reconstruction-derived CoOOH as the actual active species in the case of metal chalcogenides (sulfides and selenides) for alkaline OER.

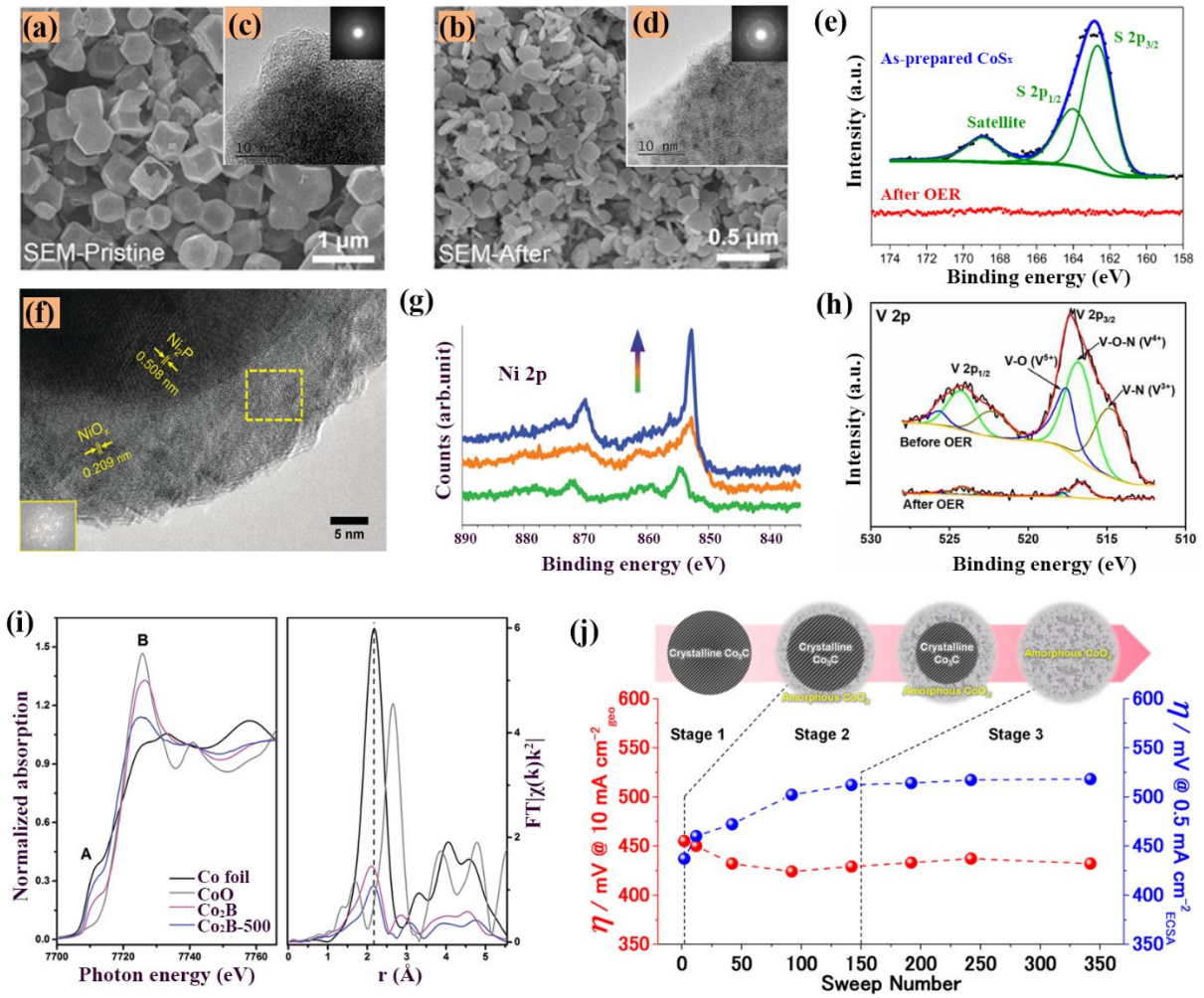

Fig. 7 The images of (a, b) SEM and (c, d) HRTEM of the original CoS_x and the CoS_x after OER, respectively. (e) S 2p XPS spectra of CoS_x before and after OER measurement. Reproduced with permission from ref. 20. Copyright 2018, American Chemical Society. (f) HRTEM image of the Ni_2P nanoparticles with a-hour electrochemical pretreatment at 1.5 V vs. RHE. (g) High-resolution depth-profiling XPS spectra of the Ni 2p area (The profiling depth increases along the arrow direction). Reproduced with permission from ref. 125. Copyright 2015, Royal Society of Chemistry. (h) V 2p XPS spectra of CoVFeN@NF catalyst before and after OER test. Reproduced with permission from ref. 133. Copyright 2020, Wiley-VCH. (i) XANES (left) and EXAFS (right) spectra of Co_2B, Co_2B-500 and references Co foil and CoO. Reproduced with permission from ref. 134. Copyright 2016, Wiley-VCH. (j) Tendency of OER overpotentials (η) along with the increasing LSV sweep number (1.0 ~ 1.9 V vs RHE) based on Co_3C electrode. Reproduced with permission from ref. 135. Copyright 2018, American Chemical Society.

3.2.2 Metal pnictides. Similar to metal chalcogenides, the design and use of metal pnictides in electrocatalysis was inspired by the natural catalytic hydrogenase.[129-131] It is well known that metal pnictides, including metal nitrides (MNs) and metal phosphides (MPs), are thermodynamically less stable than metal chalcogenides.[52] Therefore, metal pnictides can be more easily transformed into their corresponding highly active metal oxides/(oxy)hydroxides under oxidative potentials. To synthesize MPs or MNs, various phosphorus sources, such as sodium hypophosphate, sodium hydrophosphate acetate, etc.,[136] or nitrogen sources, such as ammonium hydroxide, ammonium nitrate, ammonium sulfate, and so forth,[124] have been heated under an inert protective atmosphere. Interestingly, metal pnictides can be formed with various constituent elements, stoichiometric ratios, and structures. For example, there are more than 9 stoichiometries of nickel phosphides with different Ni/P ratios, including NiP, NiP_2, NiP_3, Ni_2P, Ni_3P, $Ni_{12}P_5$, and Ni_5P_4, each showing disparate electrical conductivities and electrocatalytic performances.[137] The metallic character or even superconductivity of metal pnictides stems from the relatively high ratio of metal in their structures, which results in significant metal-metal bonding.[137]

Metal phosphides have been widely reported as high-efficient non-precious catalysts for oxygen evolution, which is due to their attractive catalytic activities and superb stabilities in strong acid and alkaline electrolyte solutions. Hu et al. were the first to developed and utilize Ni_2P as an OER catalyst in alkaline medium, and observed an electrochemical oxidation process involving the transformation into a core-shell structure, i.e., Ni_2P/NiO_x assembly, under OER conditions through ex situ HRTEM and high-resolution depth-profiling XPS analysis.[125] HRTEM images taken after OER revealed that shells with crystallinity matching nickel oxide/hydroxide species were produced around the Ni_2P particles (**Fig. 7f**). The reconstructed core-shell Ni_2P/NiO_x assembly was also evidenced by the XPS spectra, in which the phosphorus content was significantly increased, accompanied by a decrease in oxygen content, was measured when the sputtering depth reached 50 nm (**Fig. 7g**). Meanwhile, they pointed out that the generated core-shell structure may synergistically influence the catalytic activity; as of yet, further research is required to confirm the relationships between the original core and the reconstructed shell in detail. This partial surface reconstruction process during the OER in the presence of KOH has also been explored in Co-based phosphides, as well as some

bimetal-based phosphides, such as CoP, Co_2P, NiCoP, and $(Ni_{0.74}Fe_{0.26})_3P$ (as summarized in **Table 2**).[138-141]

Likewise, Chen et al. developed Co_4N nanowire arrays grown on carbon cloth (denoted Co_4N NW/CC) with excellent intrinsic metallic character as OER catalyst, and verified the catalytic mechanism via EXAFS and HRTEM.[142] The results of EXAFS suggested that the surface Co atoms were partially oxidized into cobalt oxide/hydroxide, producing a oxide/hydroxide shell with thin thickness on the surface of catalyst, while the majority of the catalyst still existed as Co_4N, as no cobalt oxides/hydroxides peaks were observed in the XPS spectra. Moreover, a steady-state amount of the electroactive species (CoO_x), as revealed by ex situ HRTEM, along with the analysis of CV tests, implied that the electrochemical surface reconstruction has its own limitation, that is, the formation of the outer CoO_x shell may block the Co_4N core from further oxidation. Compared to Co_3O_4 NW/CC (Co_3O_4 nanowire fabricated on carbon-cloth-based substrate) and Co(OH)F NW/CC (Co(OH)F nanowire fabricated on carbon-cloth-based substrate), the surface reconstruction activated Co_4N NW/CC (denoted SOA-Co_4N NW/CC) required the lowest overpotential and exhibited the best charge transfer kinetics. As evaluated by the electrochemical double-layer capacitance (C_{dl}), the SOA-Co_4N NW/CC also displayed the largest active surface area. Herein, the authors attributed the actual cause for the improved OER activity of SOA-Co_4N NW/CC to the synergistic action of the original Co_4N core with metallic property and reconstructed cobalt oxide/hydroxide shell. Benefiting from the superior conductivity of Co_4N material, the charge transport capability between the cobalt oxide/hydroxide shell and the current collector was significantly enhanced. Likewise, the surface reconstructed CoOOH shell provided active sites that could oxidize the absorbed OH^- species into O_2, thus favoring the higher OER activity.

With respect to investigate the catalytic mechanism, someone also pointed out the vitally important ingredient for improving the OER activity should be the composition defects and structure in the subsurface of the reconstructed layers in cobalt pnictides.[143] For instance, Wang and co-workers revealed that the higher OER activity of Co pnictides (Co_xP and Co_xN), in comparison to Co_3O_4, attributed to the larger extent of disordered structure and produced oxygen defect sites in the subsurface of the reconstructed Co_xO layers.[143] After anodic polarization, both the Co_xP with reconstructed Co_xO layers (denoted Co_xP–E) and Co_xN with

reconstructed Co_xO layers (denoted Co_xN–E) displayed the emergence of $Co^{2+}(O_h)$ peaks and the disappearance of $Co^{2+}(T_d)$ peaks in the EXAFS spectra, indicating that oxygen vacancies were formed. As showed in the angle resolved X-ray photoelectron (AR-XPS) spectra, the disappeared Co–P peak and the weakened Co–N peak in the Co_xP–E and Co_xN–E, respectively, suggested the reconstruction into Co_xO layer. The peaks of the adsorbed oxygen species, which is representative of the existence of oxygen defects, suggested a higher atomic ratio inside the reconstructed Co_xO layer than on its surfaces, indicating that the oxygen defects were concentrated on the subsurface of reconstructed layer. According to the ratios of $Co^{2+}(O_h)$ peak in the EXAFS spectra and the adsorbed oxygen species peak in the AR-XPS spectra, the amount of oxygen defects formed in the Co_xO layer subsurface followed the order: Co_xP–E > Co_xN–E > Co_3O_4–E; as a result, Co_xP-E exhibited the highest OER activity. Additionally, they found that the generation of CoOOH species may not occur in some cobalt-based compounds prepared through high-temperature annealing; for example, the high-temperature annealed spinel Co_3O_4 was found to be completely stable during the alkaline OER process, with no clear indicators of a phase transformation from Co_3O_4 to Co (oxy)hydroxides observed.[144]

Recently, Pan et al. utilized a trimetallic nitride (CoVFeN) as a novel OER catalyst to achieve an ultralow OER overpotential, which was the result of the catalytically active oxyhydroxide species reconstructed on its surface during the OER process.[133] Through the ex situ XRD, XPS and Raman analysis, it was confirmed that the original CoVFeN catalyst, which comprised numerous particles with rough surfaces, underwent a phase transition into the (oxy)hydroxide species, of which the reconstructed surface with numerous rough and more loosely disordered morphological nanoballs was proven to be FeOOH and CoOOH species. Additionally, the XPS results (**Fig. 7h**) indicated that CoVFeN was converted into cobalt (oxy)hydroxide species with an increased Co valence state, while the peaks of V disappeared due to the conversion from V–N species to alkaline-soluble V oxides (V_2O_5 and VO_2). They proposed that the leaching of V atoms is key to promote the transformation of cobalt oxides/nitrides on the surface of CoVFeN@NF into the cobalt (oxy)hydroxide species. This was supported by a lack of (oxy)hydroxide observed in CoFeN@NF after OER testing.

Although several detailed descriptions of the dynamic electrocatalysis process, in which a catalyst material undergoes a surface reconstruction prior to the initiation of oxygen evolution,

have been proposed, the identity of the active sites in reconstructed layers derived from bimetal pnictide catalysts is still under debate. For example, Chen et al. unveiled that a current-driven "shell-bulk" structure was built in $(Co,Fe)_3N$, where a hexagonal (Co,Fe)OOH shell was produced on the surface of $(Co,Fe)_3N$ under alkaline OER conditions.[145] In their study, they considered Co in the oxyhydroxide shell as the primary active sites owing to its periodic valence change between Co^{2+} and Co^{4+} in the electrochemical cycling process as supported by L-edge electron energy-loss spectroscopy (EELS) measurement; meanwhile, the effect of Fe was neglected due to the unchanged valence of Fe^{3+}. Noting that, the authors pointed out that the oxygen-related redox process should be the actual key for the electrochemical oxidation behavior, while the periodic swings in the oxyhydroxide shell is only an inherent process during the galvanostatic cycling. Therefore, confirming Co as the active sites is relatively difficult because the performance contribution of Co redox is insignificant, especially during the long-time cycling tests. Consequently, theoretical simulations, such as DFT, would provide more insight into the identity of the actual active sites by revealing which ones exhibit the lowest kinetic barriers for boosting water splitting.

3.2.3 Metal borides. Besides metal chalcogenides and metal pnictides, metal borides have recently garnered enormous interest and been explored as potential materials that can rival noble metal-based OER electrocatalysts. However, there are relatively few studies of metal borides as OER electrocatalysts compared with metal chalcogenides and metal pnictides. Similarly to metal pnictides, the electrocatalytic activity of metal borides also changes with the variation of metal elements and stoichiometric ratios of metal/boron. For example, two commonly reported cobalt borides with different stoichiometries, CoB and Co_2B, have been found to exhibit different electrocatalytic behaviors.[146] Intriguingly, it has been revealed that for amorphous CoB, the electron interaction between Co and B was of great importance in the surface reconstruction during the electrocatalytic reactions.[147] In general, theoretical calculations suggested that electron transfer should occur from the metal to boron when the Co–B is in the crystalline form.[148, 149] However, in a study by Gupta et al., it was pointed out that the electron transfer proceeded from B to Co, with B acting as a sacrificial agent, partially preventing Co from oxidizing.[147] In the case of Co–B in the amorphous form or metal-rich

borides (MB_x, $x \leq 2$), according to the charge transfer measurement and DFT calculations, the electron migration occurred from the B to Co (metal) atom, which yielded a more electronegative property for Co (metal). This finding was also inferred from the binding energy shifts of Co in the XPS spectra, of which a positive shift of B in the amorphous CoB in comparison to pure B and a negative shift of Co suggested the electron of B migrated to the unoccupied *d*-orbital of Co.

In contrast, boron in amorphous Co_2B has been reported to likely reduce the energy barrier of the hydroxylation reaction, promoting the irreversible surface reconstruction to form CoOOH under OER condition; this generation of the OOH□ intermediate thus promoted the OER activity.[134] In particular, boron was responsible for inducing the lattice strain of cobalt, as evidenced by the increased Co–Co bond distances in Co_2B compared to CoO observed from EXAFS (**Fig. 7i**). This lattice strain directly stemmed from the chemical interaction of cobalt and boron, including the electron transfer and hybridization between B 2p states and Co 3d orbitals, as well as the previously described electron transfer that occurs between B and Co during the OER process. Theoretical calculations were used to verify that the hybridization between B 2p states and Co 3d orbitals would cause the reinforcement of Co–B and B–B bonds, whereas the Co–Co bonds would be weakened.[150] The theoretical calculation emphasized the effect of the weakened Co–Co bonds on reducing the energy barrier for oxyhydroxide species production during the OER. Through both experimental and theoretical studies, boron is confirmed to be the major contributor that promotes the surface reconstruction of metal borides and improves the OER activity.[134] Apart from the mono-metal borides, some bimetal borides have been found to exhibit a similar surface reconstruction. Pan et al. constructed a sequence of bimetal Ni-Co borides, and observed that CoOOH and NiOOH intermediates were produced during the OER process through XPS measurements.[151] However, further studies are anticipated to explore the synergistic effect of both Ni and Co on the surface reconstruction process and OER activity.

3.2.4 Metal carbides. Tungsten carbide was first discovered as a platinum-like electrocatalyst due to its *d*-band electronic density state similar to platinum.[152] This revelation evoked great interest in the research and development of metal carbide-based applications,

including heterogeneous catalysis, fuel cells and so on.[153-156] Currently, there are few reported studies focused on the surface reconstruction of metal carbides. An investigation into the surface reconstruction of Co_3C provided by Mullins and co-workers serves as a representative case of novel metal carbide precatalysts and their transformation into metal oxides during electrochemical oxidation.[135] The reconstruction of Co_3C was systematically studied by measuring the OER overpotential and electrochemically active surface area (ECSA), in addition to performing HRTEM, XPS and XRD characterizations, after the system was exposed to an increasing number of linear sweep voltammetry (LSV) scans. First, the formation of a ~4 nm thick amorphous oxide shell around Co_3C was observed after two LSV sweeps. The ECSA results became much changeless after 150 sweeps, and the core-shell structure was no longer present in the HRTEM images of the particles, suggesting a complete reconstruction of Co_3C into amorphous Co oxide particles. Furthermore, the overpotential and ECSA remained stable after 350 sweeps, which further confirmed that the complete reconstruction into Co oxide was achieved after 150 LSV sweeps. The entire reconstruction process of Co_3C during the OER was summarized and divided into three stages (**Fig. 7j**) as follows: (i) crystalline Co_3C → (ii) Co_3C core-amorphous Co oxide shell → (iii) amorphous Co oxide.

3.2.5 Metal fluorides. Among metal compounds, the metal fluorides have been mostly reported for their application in supercapacitors, lithium ion batteries, and so forth.[157-159] However, given that the chemical or electrochemical properties of the fluorine ions are unpredictable and the bond between metal and fluorine is weak, metal fluorides are rarely applied in the field of electrocatalytic water splitting.[160] Generally, fluorine ions are much easier to replace with other anions during the electrochemical testing process, which is beneficial to initiate surface reconstruction and to optimize the OER activity. In addition, the leaching of fluorine ions can further increase the amount of sites on the catalyst with unsaturated coordination, which would enhance water splitting.[161] In addition, as a result of having the highest electronegativity, fluorine can absorb the electrons from neighboring metals, thus manipulating the electronic structure of electrocatalysts surface, tuning the energy band, and enhancing the adsorption of reactive species. Therefore, metal fluorides have been considered promising alternatives to achieve high-efficiency OER catalysts. Recently, Dong

and co-workers utilized Fe-doped CoF_2 as electrocatalyst to explore its OER activity and catalytic mechanism.[162] The Fe-doped CoF_2 catalyst was prepared via a two-step synthesis strategy, involving the hydrothermal fabrication of Fe-doped $Co(OH)_2$ and a subsequent fluorination process. Afterwards, cobalt hydroxide produced through anionic reconstruction during the alkaline OER process, favored a superior OER activity with a low overpotential and stability. The appearance of $Co(OH)_2$ was detected by XRD, and the amount of oxygen increased while the fluorine decreased, which illustrated the partially transformation of CoF_2 into $Co(OH)_2$ on the electrode surface through anionic reconstruction.

Table 2. Summary of the synthesis methods, surface reconstruction potential, original oxidation state, reconstructed oxidation state, and measurements for analyzing the surface reconstruction of the metal non-oxides catalysts, including metal chalcogenides (MS and MSe), metal pnictides (MN and MP), metal borides (MB), metal carbides (MC), and metal fluorides (MF) during the OER.

Catalyst	Synthesis method	Surface reconstruction potential (V vs. RHE)	Original oxidation state/structure	Reconstructed oxidation state/surface species/structure	Measurements for detecting surface reconstruction	Application (electrolyte)	Ref.
Metal chalcogenides							
CoS_2	Electrodeposition and sulfurization	~1.75 V	CoS_2	CoO_2	ex situ TEM, ex situ XRD and ex situ XPS	OER (1.0 M KOH)	18
CoS_x	Hydrothermal	Not available	CoS_x → $Co(OH)_2$ → CoOOH	CoOOH	in situ TEM, in situ FTIR and ex situ XAS	OER (1.0 M KOH)	20
$Co_{1-x}Ni_xS_2$	Hydrothermal	1.35 V	$Co_{1-x}Ni_xS_2$ → $Co(OH)_2$/Ni(OH)$_2$ → CoOOH/NiOOH	Ni-Co (hydr)oxide layer	LSV	OER (1.0 M KOH)	163
$NiCo_2S_4$	Hydrothermal	1.36 V	Ni^{2+} and Co^{2+}	CoOOH and NiOOH	ex situ XPS	OER (1.0 M KOH)	164
NiS	Pulse-electrodeposition	1.40 V	Ni^{2+}	Ni^{3+} (NiO_x)	ex situ SEM, ex situ XPS and ex situ XRD	OER (1.0 M KOH)	11

Cu_2S	Anion exchange	Not available	Cu^+ ($Cu_2S \rightarrow Cu(OH)_2 \rightarrow CuO$)	Cu^{2+} (CuO)	in situ Raman, ex situ SEM, ex situ XRD, ex situ XPS and ex situ EELS	OER (1.0 M KOH)	165
Cu_9S_5	Low-temperature molecular precursor method	Not available	Cu_9S_5	CuO	ex situ XPS	OER (1.0 M KOH)	166
MoS_2	Hydrothermal	Not available	MoS_2	MoO_3	ex situ SEM	OER (1.0 M NaOH)	167
$Ni_xFe_{1-x}Se_2$	Hydrothermal	Not available	$Co^{2+}{}_{Td}$	$NiFeO_x$	ex situ TEM, ex situ PXRD and ex situ XPS	OER (1.0 M KOH)	21
$(Ni, Co)_{0.85}Se$	Hydrothermal	1.31 V	$Ni^{2+} \rightarrow Ni^{3+} \rightarrow Ni^{4+}$	γ-NiOOH	ex situ XPS	OER (1.0 M KOH)	59
FeCoMo-Se	Hydrothermal	Not available	$FeSe_2$, $CoSe_2$	FeCo-oxyhydroxide	ex situ PXRD, ex situ SEM, ex situ EDX, ex situ HRTEM, and ex situ XPS	OER (1.0 M KOH)	168
NiSe	Hydrothermal	~1.40 V	NiSe	nickel oxide ($Ni(OH)_2$ and/or NiOOH)	ex situ XPS	OER (1.0 M KOH)	169
CuSe	High-temperature solid-state method	Not available	CuSe	$Cu(OH)_2$	LSV	OER (1.0 M KOH)	170
Metal pnictides							
Ni_2P	Thermal reaction	1.38 V	Ni^{2+} (Ni_2P)	Ni^{3+} (a core–shell Ni_2P/NiO_x assembly)	ex situ TEM and ex situ high-resolution depth-profiling XPS	OER (1.0 M KOH)	125
Co_xP	Hydrothermal and calcination	Not available	Co_xP	Co_xO	ex situ AR-XPS and in situ Raman	OER (1.0 M KOH)	143
$(Ni_{0.74}Fe_{0.26})_3P$	Electrochemical etching	Not available	Ni (Fe) phosphides	Ni(Fe) (oxy)hydroxides	ex situ TEM, ex situ STEM, and operando XAS	OER (1.0 M KOH)	138
NiCoP	Solvothermal and phosphorization	~1.30 V	NiCoP	Ni(Co)OOH	in situ Raman and ex situ TEM and ex situ XPS	OER (1.0 M KOH)	139
Co_4N	Hydrothermal and nitridation	Not available	$Co_4N \rightarrow CoOOH/Co_4N \rightarrow CoO_2/Co_4N$	CoO_2/Co_4N	ex situ EXAFS and ex situ HRTEM	OER (1.0 M KOH)	142
Co_xN	Hydrothermal and calcination	Not available	Co_xN	Co_xO	ex situ AR-XPS and in situ Raman	OER (1.0 M KOH)	143
$(Co,Fe)_3$	Precipitation and	Not available	Co^{2+}	Co^{4+}	Operando EXAFS	OER (0.1 M	145

N	thermal ammonization			((Co,Fe)OOH shell)		$HClO_4$)	
CoVFeN	Hydrothermal, electrodeposition and thermal nitridation	Not available	cobalt oxide/nitrides	$CoO_x(OH)_y$	ex situ Raman, ex situ SEM, ex situ XPS and ex situ XRD	OER (1.0 M $HClO_4$)	133
Metal borides							
Co_2B	Chemical reduction	1.1 V ~ 1.3 V	Co^{2+}	Co^{3+} (CoOOH)	ex situ XPS	OER (0.1 M KOH)	134
Co–10Ni–B	Chemical reduction	Not available	Co borides and Ni borides	CoOOH and NiOOH	ex situ XPS and ex situ XRD	OER (1.0 M KOH)	151
Metal carbides							
Co_3C	Wet-chemical method	~0.3 V (first) ~1.2V (second)	Co_3C → Co_3C/Co oxide → amorphous Co oxide	amorphous Co oxide	ex situ TEM and ex situ XPS	OER(1.0 M NaOH)	135
Metal fluorides							
Fe-doped CoF_2	Hydrothermal method and chemical vapor deposition fluorination	Not available	CoF_2	$Co(OH)_2$	ex situ SEM, ex situ XPS and ex situ XRD	OER (1.0 M KOH)	162

3.3 Metal hydroxides/layered double hydroxides

As typical layered-type catalysts, metal hydroxides ($M(OH)_2$; M is a transition metal) and metal layered double hydroxides (MLDHs) have exhibited outstanding electrocatalytic activity towards OER.[171] As shown in **Fig. 8a**, the general layered-type catalyst crystal structure is composed of alternating layers of MO_6 subunits, which connect with each other through edge-sharing, and protons (H^+) which stack on top of each other to result in a 2-D layered structure.[172] Comparatively, MLDHs generally with the chemical formula of $M^{2+}_{1-x}M^{3+}_x(OH)_2(A^{n-})_{x/n} \cdot zH_2O$ possess a larger inter-layer distance ($d_2 > d_1$) due to the intercalation of anions and water molecules in the layers.[7, 172, 173] One of the most intensively studied layered-type electrocatalysts are Ni-Fe (oxy)hydroxides, which have been researched for more than 30 years and represent a class of best-performance catalysts with the some of the lowest reported overpotentials for OER in alkaline electrolyte.[7] Apart from their remarkable OER activity, metal (oxy)hydroxides have been also investigated as precatalysts that form more

electrocatalytically active phases under oxidation conditions. **Table 3** summarizes some representative metal hydroxides and MLDHs that undergo surface reconstruction in oxidative conditions.

To understand the surface reconstruction mechanism of layered-type electrocatalyst, herein, $Ni(OH)_2$ is selected as an example. During the OER, $Ni(OH)_2$ dynamically experiences oxidation and deprotonation, resulting in the formation of reconstructed Ni oxyhydroxides. Note that the common Ni oxidation state in $Ni(OH)_2$ is +2, while the reconstructed Ni oxidation state can assume different values. The Ni could accomplish a full oxidation from +2 to +3 as described by the following transformation: $Ni(OH)_2 + OH^- \rightarrow NiOOH + H_2O + e^-$, where Ni in NiOOH possesses a +3 oxidation state. As shown in the Bode diagram (**Fig. 8b**), there are four different phases of Ni (oxy)hydroxides that can exist during electrochemical oxidation reactions, that is, α-$Ni(OH)_2$, β-$Ni(OH)_2$, β-NiOOH, and γ-NiOOH.[7] It has been determined that the active phase for OER is ascribed to γ-NiOOH, in which the average Ni oxidation state is 3.5 ~ 3.7.

For example, Yan et al. performed in situ Raman and operando XRD to study the dynamic generation of γ-NiOOH in NiCe hydroxide ($NiCeO_xH_y$) during the OER.[174] As shown in the Raman spectra (**Fig. 8c**), a clear variation of the catalysts occurred during the operando OER in alkaline solution. For $NiCeO_xH_y$, the peaks at 454, 494 and 595 cm^{-1} are ascribed to Ce–O, Ni–O and Ni–O–Ce vibrations, respectively. At 1.27 V, the characteristic peaks of γ-NiOOH phase, 474 and 554 cm^{-1}, appeared, indicating the transition of $NiCeO_xH_y$ to γ-NiOOH. Interestingly, in contrast to the amorphous state of $NiCeO_xH_y$, the XRD patterns suggested considerable crystallinity just shortly after electrochemically testing in 1 M KOH solution.

This phase transformation behavior was also found to occur in NiFe layered double hydroxide (LDH) during electrochemical processing at high anodic potentials, as reported by Edvinsson et al.[175] Similarly, the reconstruction of $Ni(OH)_2$ into NiOOH was confirmed via in situ Raman measurements (**Fig. 8d** and **e**), which showed the appearance of γ-NiOOH phase spectral features with an average Ni oxidation state of +3.3 ~ +3.7. Interestingly, the NiFe LDH showed a slower conversion from $Ni(OH)_2$ to NiOOH at larger applied potentials than pure $Ni(OH)_2$, which indicated that the existence of Fe component in NiFe LDH suppressed the dynamic reconstruction into NiOOH. However, the higher ratio of newly appeared Raman peak

intensities demonstrated a higher degree of γ-NiOOH generation in NiFe LDH. Therefore, it was proposed that the FeOOH species would be produced in NiFe LDH at low potentials, whereas the NiOOH species tended to form at higher potentials; this could be ascribed to the stronger Lewis acid property of Fe^{3+} ions in NiFe LDH, which are more likely to bond with OH^-.

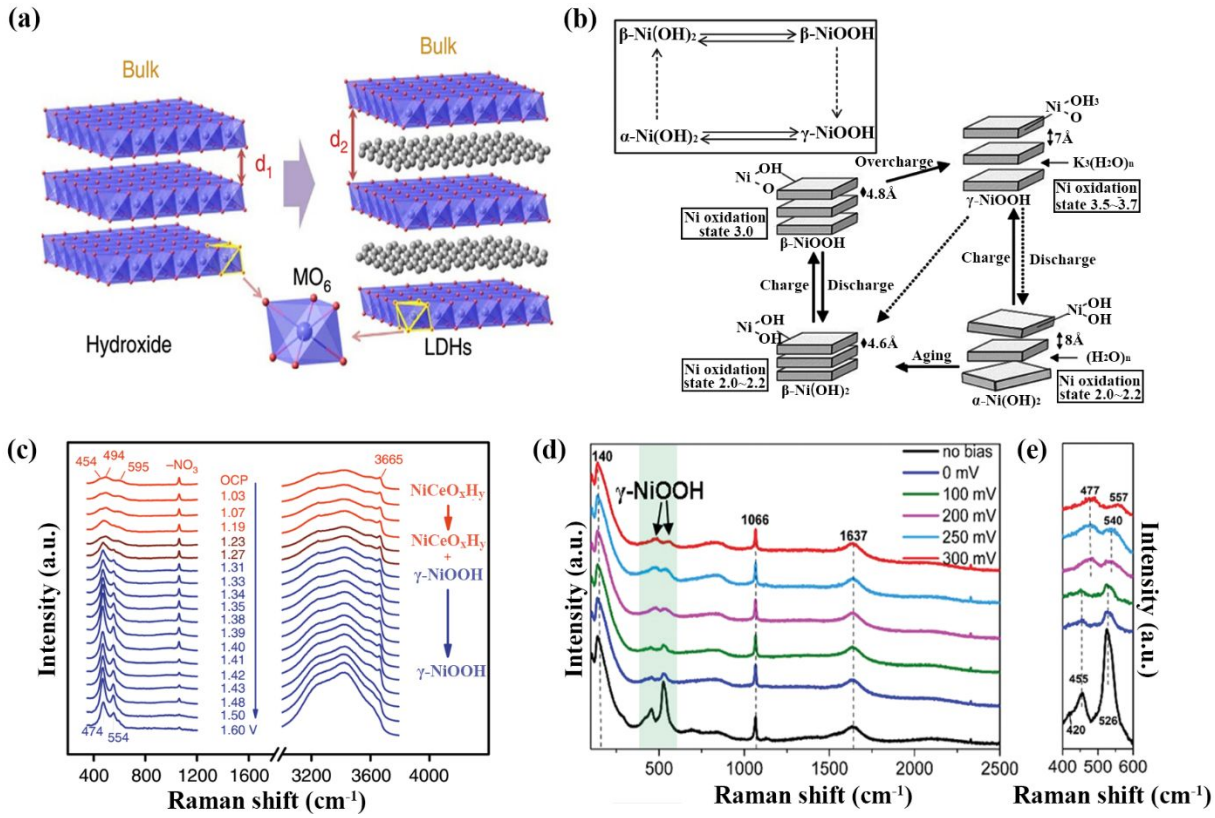

Fig. 8 (a) Schematic diagram describing the layered hydroxides and the LDHs intercalated with anions and H_2O molecules. d_1 and d_2 are the distances between each inter layers in hydroxides and LDHs, respectively, $d_2 > d_1$. Reproduced with permission from ref. 172. Copyright 2014, Springer Nature. (b) Bode scheme illustrating the reconstruction of $Ni(OH)_2$. Reproduced with permission from ref. 7. Copyright 2016, Wiley-VCH. (c) In situ Raman spectra collected on $NiCeO_xH_y$/graphite electrodes during the OER (from open circuit potential (OCP) to 1.6 V vs. RHE in 1.0 M KOH). Reproduced with permission from ref. 174. Copyright 2018, Springer Nature. (d) In situ Raman spectra collected on NiFe LDH at different overpotentials in 1.0 M KOH. (e) Magnified wavelength region in accordance with the green marked area of (d).

Reproduced with permission from ref. 175. Copyright 2019, Royal Society of Chemistry.

Table 3. Summary of the synthesis methods, surface reconstruction potential, original oxidation state, reconstructed oxidation state, and measurements for analyzing the surface reconstruction of the metal hydroxides ($M(OH)_2$) and metal layered double hydroxides (MLDHs) during the OER.

Catalyst	Synthesis method	Surface reconstruction potential (V vs. RHE)	Original oxidation state/structure	Reconstructed oxidation state/surface species/structure	Measurements for detecting surface reconstruction	Application (electrolyte)	Ref.
$NiCeO_xH_y$	Electrodeposition	1.27 V	Ni(II)	Ni(III) (γ-NiOOH)	in situ Raman, operando XRD, ex situ FTIR and ex situ XPS	OER (1.0 M KOH)	174
$CoNi(OH)_x$	Solution-phase cation exchange	1.20 ~ 1.30 V (first) 1.30 ~ 1.40 V (second)	Co^{2+} and Ni^{2+}	Co^{3+} and Ni^{3+} (CoOOH and NiOOH)	CV	OER (1.0 M KOH)	176
NiFe LDH	Hydrothermal	Not available	Ni^{2+} ($Ni(OH)_2$)	$Ni^{3.3\sim3.7+}$ (NiOOH) and Fe^{3+} (FeOOH)	in situ Raman, ex situ FTIR and ex situ XPS	OER (1.0 M KOH)	175
ultrathin Ni–Fe LDH	Alcohol intercalation method	1.42 V	Ni^{2+} and Fe^{3+}	Ni^{3+} and Fe^{4+}	operando XAS	OER (1.0 M KOH)	177
Ni–Fe hydroxide	Alcohol intercalation method	Not available	Ni–Fe hydroxide	FeOOH	operando XAS	OER (1.0 M KOH)	178
$Co(Fe)O_xH_y$	Electrodeposition	Not available	Co^{2+} and Fe^{3+}	Co^{3+} and $Fe^{4+/5+}$	operando XAS	OER (1.0 M KOH)	179
NiCo carbonate hydroxide	Hydrothermal	Not available	Co^{2+} (NiCo carbonate hydroxide)	Co^{3+} (NiCo LDH and $Ni(OH)_2$)	operando EXAFS and ex situ XAS	OER (6.0 M KOH)	180

3.4 Metals/metal alloys

Metals and metal alloys have been proved as promising candidates to enhance the catalytic reactivity, especially, the 3d transition metals possessing alloying effect can further tune the catalytic property.[54, 55] It can be easy to dynamically change a metal or metal alloy catalyst

surface under alkaline condition, thus giving rise to a coexistence of multiple surface phases and the formation of meta-stable phases.

As aforementioned, metal tellurides are classified as metal alloys due to the strong metallic property of Te anions. Huang et al. precisely performed an electrochemical reconstruction of $IrTe_2$ hollow nanoshuttles (HNSs) by adjusting the applied potential (mild and high potentials) to produce different reconstructed products, that is, $IrTe_2$ with metal Ir shell (D-$IrTe_2$ HNSs) at mild potentials (**Fig. 9a**), and $IrTe_2$ HNS with IrO_x surface (DO-$IrTe_2$ HNSs) at high potentials (**Fig. 9b**), respectively.[181] As shown in **Fig 9a**, during the electrochemical dealloying at mild potentials, Te was selectively leached because of its weaker stability than Ir, resulting in the production of D-$IrTe_2$ HNSs. In contrast, when cycling was performed at high potentials, the Te leaching took place concurrently with the oxidation of Ir, leading to the generation DO-$IrTe_2$ HNSs, as confirmed by the decrease of H_2 adsorption charges in CV plots. Additionally, XANES results revealed that the Ir L_3 edge in D-$IrTe_2$ HNSs was close to those of $IrTe_2$ and Ir/C, demonstrating the metallic property of Ir in the system. While the DO-$IrTe_2$ HNSs presented a positive shift towards IrO_2, which illustrated that Ir in DO-$IrTe_2$ HNSs was partially oxidized into IrO_x. According to the operando XAS tests (**Fig. 9c** and **9d**), the Ir would undergo further oxidation and form Ir^{3+}–OH on the surface of DO-$IrTe_2$ HNSs when taking the OER test from 0.5 to 1.5 V, with such a surface reconstruction being reversible for DO-$IrTe_2$ HNSs through backward scanning from 1.51 to 0.5 V.

More strikingly, there are more and more studies focused on the in situ dealloying of multi-metal alloys and then in situ generation of actual active oxyhydroxides via electrochemical oxygen evolution process (summarized in **Table 4**).[182-186] For example, Xia and co-workers achieved homogeneous oxyhydroxides, namely, Fe-doped NiOOH and Cu-doped NiOOH, through the in situ reconstruction of the multi-metal-site alloys (denoted MsA) $FeNi_3$ and NiCu, respectively.[185] A series of characterizations, including XRD, Raman, XPS, and scanning transmission electron microscopy (STEM), were performed to explore the in situ reconstruction process and the dealloyed products (denoted dealloyed multi-metal-site alloy, DMsA). As shown in **Fig 9e**, it was observed that a Ni-contained shell and a Cu-contained core formed after 3000 CV cycles, confirming the transformation to DMsA. The results of XRD, Raman and XPS confirmed the existence of NiOOH with Ni^{3+}, FeOOH with Fe^{3+}, and $Cu(OH)_2$

with Cu^{2+}, which indicated that the crystalline DMsA comprised Fe-doped NiOOH and Cu-doped NiOOH. This further verified the in situ structural reconstruction from multi-metal alloys to multi-metal oxyhydroxides via electrochemical dealloying (**Fig. 9f**). Furthermore, the operando attenuated total reflectance FTIR (ATR-FTIR) contour image in **Fig. 9g**, directly demonstrated the O–O bond as the intermediates generated in the OER process, where the peak intensity of O–O bond rapidly increased when the potential was raised to 1.68 V, indicating an O–O bond produced among the metal sites. According to the oxygen evolution mechanism, the generation of O–O bond could be promoted by the synergistic effect between multi-metal sites, and then directly evolved O_2 from the electrocatalytic system, thus boosted the OER.

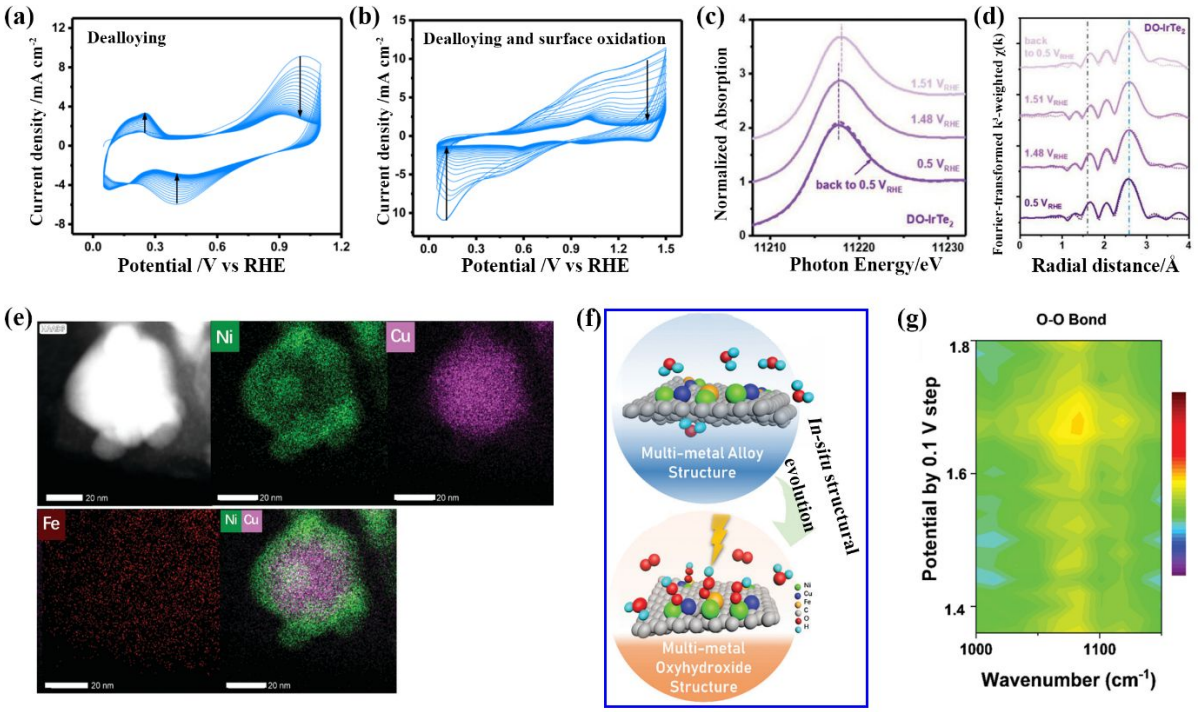

Fig. 9 Electrochemical protocols for fabricating (a) D-$IrTe_2$ HNSs and (b) DO-$IrTe_2$ HNSs. (c) Normalized XANES profiles of DO-$IrTe_2$ HNSs at different potentials. (d) k^3-Weighted Fourier transforms of EXAFS profiles of DO-$IrTe_2$ HNSs at different potentials. Reproduced with permission from ref. 181. Copyright 2020, Wiley-VCH. (e) High-angle annular dark field scanning transmission electron microscopy (HAADF-STEM) image and corresponding elemental mapping of DMsA. Scale bar: 20 nm. (f) Schematic illustration of the structural reconstruction process initiated via electrochemical dealloying. (g) 2D contour image of the operando ATR FT-IR spectrum for DMsA electrocatalyst along with the OER proceeding from

1.4 V to 1.8 V vs. RHE in 1.0 M $H_2{}^{16}O$-labelled KOH. Reproduced with permission from ref. 185. Copyright 2020, Royal Society of Chemistry.

Table 4. Summary of the synthesis methods, surface reconstruction potential, original oxidation state, reconstructed oxidation state, and measurements for analyzing the surface reconstruction of the metals and multi-metal alloys during the OER.

Catalyst	Synthesis method	Surface reconstruction potential (V vs. RHE)	Original oxidation state/structure	Reconstructed oxidation state/surface species/structure	Measurements for detecting surface reconstruction	Application (electrolyte)	Ref.
$IrTe_2$	Hydrothermal	Not available	Ir	IrO_x	operando XAS	OER (0.1 M KOH)	181
AuNi	Hydrothermal	~1.4 V	Ni →$Ni(OH)_2$ → $Ni^{3+/4+}$	$Ni(OH)_2$ $Ni^{3+/4+}$	ex situ XPS and ex situ XRD	OER (1.0 M KOH)	186
$FeSn_2$	Reduction	Not available	Fe^0	Fe^{3+} (α-FeO(OH))	ex situ XPS, ex situ Raman and ex situ PXRD	OER (1.0 M KOH)	182
$CoSn_2$	Reduction	~1.1 V	$Co^{0/2+}$	Co^{3+} (CoO_x(H))	ex situ XPS	OER (1.0 M KOH)	184
$FeNi_3$ and NiCu alloys	Hydrothermal and pyrolysis	Not available	Ni^0, Fe^0, and Cu^0	Ni^{3+} (NiOOH), Fe^{3+} (FeOOH), and Cu^{2+} ($Cu(OH)_2$)	ex situ XRD, ex situ XPS and ex situ STEM	OER (1.0 M KOH)	185
Ni_3Sn_2	Reduction	1.30 ~ 1.45 V	Ni^0	$Ni^{2+/3+}$ (NiO_xH_y)	ex situ TEM and ex situ XPS	OER (1.0 M KOH)	187
$NiFe_xSn$ alloy	Electrodeposition	Not available	metallic Ni and Fe	NiFe (oxy)hydroxide	ex situ XRD, ex situ XPS and ex situ TEM	OER (1.0 M KOH)	183

4. Strategies for activating surface reconstruction

Based on the aforementioned discussion and considerable number of reports, surface reconstruction plays a vital role in enhancing electrocatalytic performance; however, its ability to be utilized is still restricted because the reconstructed layer can prevent electrolyte ions from further penetrating into the catalyst material. Therefore, initiating and tuning the surface reconstruction process via rational and effective strategies is more pivotal and remains a challenge. It has been widely accepted that changing the electrochemical conditions, including

the electrolyte pH, conductivity of supports, applied potentials, and time, can modulate the electrochemical redox process. For example, Strasser et al. uncovered the effect of electrolyte pH on the electrochemical oxidation-reduction process by studying the Ni-Fe(OOH) catalyst through a series of in situ/operando measurements, including in situ UV-vis measurements, operando differential electrochemical mass spectrometry (DEMS), and in situ cryo XAS.[64] The analyses consistently confirmed that an electrolyte pH larger than 13 significantly increased the redox peak region of the Ni-Fe oxyhydroxide, induced a lower-potential redox reaction, and led to a 2~3 fold enhancement in OER activity. In addition to changing these electrochemical conditions, other strategies have emerged which can be readily employed to modulate the surface reconstruction, such as substituting/doping with metals, introducing anions, incorporating defects, tuning morphologies, and utilizing the plasmonic/thermal/photothermal effect. In the following sections, we outline recent works which apply these strategies to control the surface reconstruction process. **Table 5** provides a representative summary of the recently reports regarding surface reconstruction activation for OER electrocatalysts.

4.1 Metal-doping/substituting-facilitated

Recently, metal-doping/substituting has been revealed as an effective way to activate the surface reconstruction process, resulting in generating the electrocatalytically active species for oxygen evolution. A detailed investigation of the dynamic active site generation on spinel $CoAl_2O_4$ facilitated by Fe substitution was reported by Xu and co-works, in which they found that a low level-substitution of Fe (x = 0.25) in the system, i.e. $CoFe_{0.25}Al_{1.75}O_4$, resulted in an increased OER performance under alkaline conditions.[188] Pseudocapacitive behaviors during potential sweeps was observed in the CV curves of $CoAl_2O_4$ and $CoFe_{0.25}Al_{1.75}O_4$, demonstrating that the irreversible reconstruction process into oxyhydroxides species occurred on the surfaces of both materials. According to the in situ Co EXAFS spectra, the peak of Co_{Oh} (Co in octahedral site) in both $CoAl_2O_4$ (**Fig. 10a**) and $CoFe_{0.25}Al_{1.75}O_4$ (**Fig. 10b**) increased with the rising applied potentials in the K-edge spectra; and the L-edge spectra (**Fig. 10c**) demonstrated an increased oxidation state of Co ions, indicating an irreversible reconstruction of Co oxyhydroxide accompanied with the oxidation of Co^{2+} to Co^{3+}. The in situ Fe EXAFS

spectra presented no change in Fe valence state at open circuit potential (OCP) and 1.5 V, which conclusively excluded the reconstruction of Fe ions during the CV sweeps. More interestingly, a less anodic peak appeared in $CoFe_{0.25}Al_{1.75}O_4$ (~1.32 V) than $CoAl_2O_4$ (~1.41 V), and the overpotential for $CoFe_{0.25}Al_{1.75}O_4$ was significantly reduced in the second CV curve in comparison to the first cycle; meanwhile, no noticeable variation can be observed in the CV curves of $CoAl_2O_4$, suggesting a positive impact of Fe substitution on both the generation of more electrocatalytically active oxyhydroxides and the subsequent oxygen evolution. After the oxidation of Co^{2+} to Co^{3+}, it was observed that $CoFe_{0.25}Al_{1.75}O_4$ required an approximately 70 mV lower overpotential in comparison to $CoAl_2O_4$. As aforementioned, the high oxidation state (Co^{3+}) obtained by oxidizing Co^{2+} is considered a critical step for the dynamic generation of active oxyhydroxide species.[189, 190] **Fig. 10d** presented the nominal valence states of $CoFe_{0.25}Al_{1.75}O_4$ and $CoAl_2O_4$ under applied potentials that were measured by in situ XANES. For $CoFe_{0.25}Al_{1.75}O_4$, it exhibited the valency increment of Co in both regions I (1.05 ~ 1.20 V) and II (1.20 ~ 1.42 V). While the increasing trend of Co valence state was only observed in regions I for $CoAl_2O_4$, which represented the limitation in the deprotonation process of $CoAl_2O_4$. The second deprotonation process of $CoAl_2O_4$, that is, the pre-OER stage, occurred at region III (1.42 ~ 1.52 V). Therefore, the delay of the second deprotonation process caused the retardation of the OER kinetics. Concerning the active oxyhydroxides, the active oxygen species have been considered as the ultimate active site in some studies, which would be produced by the deprotonation of the reconstructed oxyhydroxides during the anodic sweeping process.[191, 192] Therefore, the authors proposed a proton/electron transfer (deprotonation) process to illustrate the active oxygen site reconstruction on the electrocatalysts. For $CoFe_{0.25}Al_{1.75}O_4$, there were two deprotonation steps as follows (**Fig. 10e**). Firstly, the deprotonation began at the OH site of Co–OH–Fe, and the neighboring Fe^{3+} center was responsible for facilitating this process, leading to an increase in the Co oxidation state. Subsequently, the following deprotonation was accomplished at the OH site of Co–OH, as evidenced by the activated Co oxidation in the case of $CoFe_{0.25}Al_{1.75}O_4$. Additionally, in the second step, the negatively charged oxygen ligand (O□) would be formed and act as an active site, accounting for a boosted OER with lowered overpotential. However, without Fe substitution ($CoAl_2O_4$), the deprotonation occurred only on bridged OH, and then the second

deprotonation process was suppressed, resulting in a limitation in triggering OER.

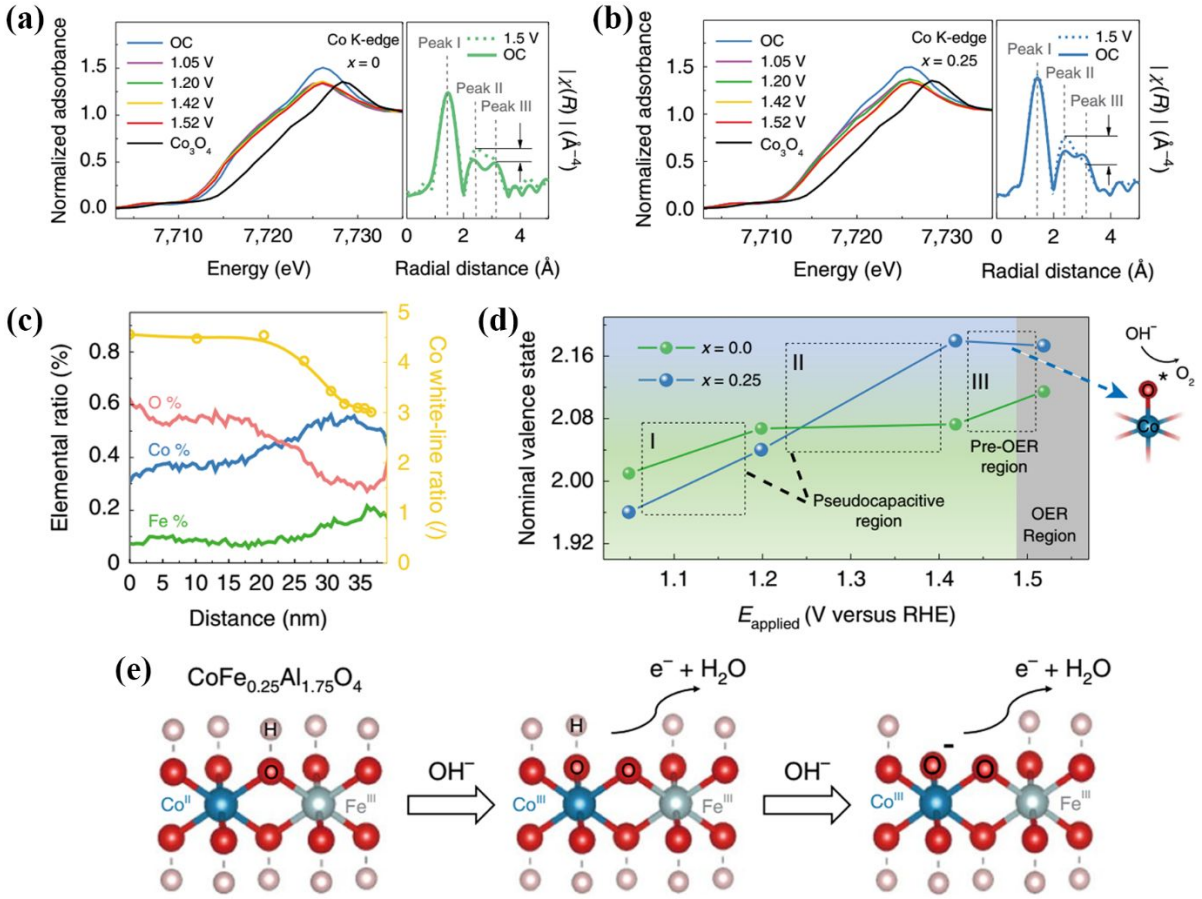

Fig. 10 Normalized in situ Co K-edge XANES spectra and in situ EXAFS spectra (right axis) of (a) $CoAl_2O_4$ and (b) $CoFe_{0.25}Al_{1.75}O_4$ (left axis) under different potentials using Co_3O_4 as reference. Peaks I, II and III in the EXAFS spectra correspond to the radial distances of Co–O, Co_{Oh}–Co_{Oh} and Co_{Oh}–Co_{Td}, respectively. (c) Co white-line ratio derived from the L-edge. (d) Tendency of the variations of Co oxidation states in $CoFe_{0.25}Al_{1.75}O_4$ and $CoAl_2O_4$ under different potentials. (e) Two-step deprotonation process before OER proposed for $CoFe_{0.25}Al_{1.75}O_4$. Reproduced with permission from ref. 188. Copyright 2019, Springer Nature.

4.2 Anion-induced

The introduction of anions has been also applied to induce the in situ surface reconstruction of electrocatalysts under OER conditions. Hu et al. reported that NiFe hydroxide nanosheets array incorporated with fluoride (denoted NiFe-OH-F) exhibited an unexpectedly excellent OER activity due to the highly active NiFe oxide layer produced by F-induced

dynamic surface reconstruction (denoted NiFe-OH-F-SR).[160] HRTEM and XPS results in **Fig. 11a** and **11b**, showed a clear loss of F content, while the oxygen signals appeared, revealing the occurrence of F-leaching. Additionally, the directly-synthesized NiFe hydroxide (NiFe-OH) exhibited significant differences in CV cycling with NiFe-OH-F, of which the oxidation peak in NiFe-OH gradually increased after the first 8 cycles but began to shrink following the 9th cycle until it disappeared. Conversely, the oxidation peak of $Ni(OH)_2$/NiOOH in NiFe-OH-F positively shifted in the 50 cycles. The NiFe-OH-F showed a much better OER activity at same overpotential than NiFe-OH following the CV cycling; however, the original NiFe-OH possessed a slightly higher OER activity in comparison to the original NiFe-OH-F. These results indicated that the F-leaching during the electrochemical process played a crucial role in the in situ reconstruction of NiFe-OH-F into the active amorphous oxide, thus promoting the OER. Because of the weak mechanical stability of a completely reconstructed catalyst material, it was suggested that the reconstructed core-shell structure was more desirable for high OER activity. Therefore, there still exists tremendous challenges to interpret the balance of thickness ratio between the reconstructed shell and the original catalyst core, which is critical to form a stable and highly active OER electrocatalyst.

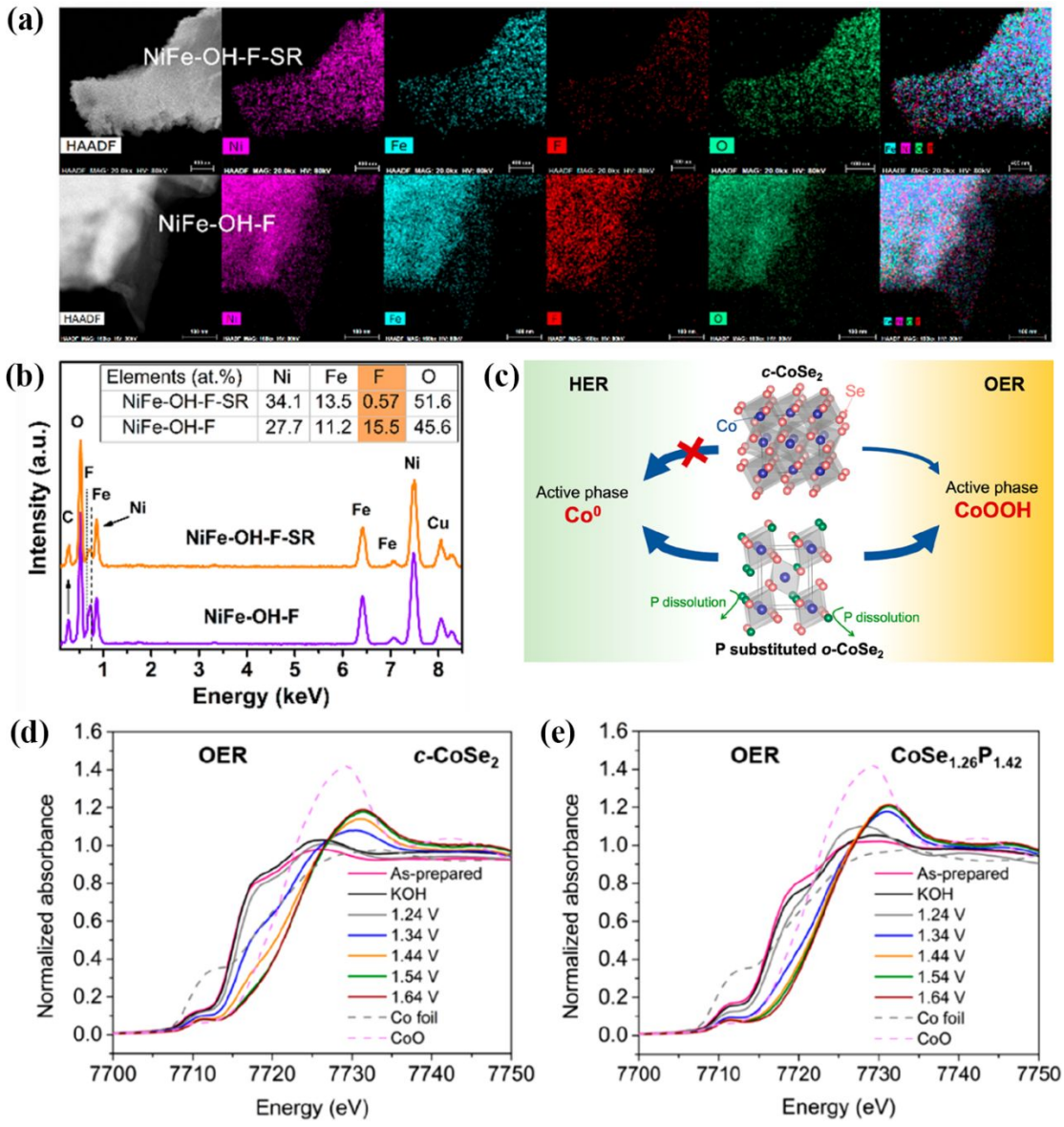

Fig. 11 (a) Elemental mapping images and (b) EDX spectra of NiFe-OH-F-SR and NiFe-OH-F. Reproduced with permission from ref. 160. Copyright 2019, American Chemical Society. (c) Schematic models of P-induced structure reconstruction in $CoSe_2$ during the HER and OER under alkaline conditions. In situ Co K-edge XANES spectra of (d) c-$CoSe_2$ and (e) $CoSe_{1.26}P_{1.42}$ during the OER. Reproduced with permission from ref. 193. Copyright 2019, American Chemical Society.

In addition to fluoride, phosphorus (P) substitution has also been revealed to facilitate the structural transformation of certain electrocatalyst materials. For example, P substitution into $CoSe_2$ was found to promote its surface reconstruction into the actual active species in alkaline

solution, i.e., metallic Co for hydrogen evolution reaction (HER) and CoOOH OER (**Fig. 11c**).[193] Focusing on the P-substituted $CoSe_2$ ($CoSe_{1.26}P_{1.42}$) for OER, the in situ XANES spectroscopy analysis (**Fig. 11d** and **11e**) evidently clarified that the Co was more easily oxidized into a high valence state (Co^{3+}) under a lower potential of 1.44 V than the original $CoSe_2$ (c-$CoSe_2$, 1.54 V). Furthermore, the results of in situ Raman, ex situ inductively coupled plasma mass spectrometry (ICP-MS), and ex situ XPS analyses consistently demonstrated that both P and Se anions were leached out during the OER process, confirming that the reconstructed cobalt oxyhydroxide (CoOOH) was the actual active species for OER.

Quite recently, Wang et al. applied a cationic redox-tuning strategy via doping of Cl to rationally manipulate both the in situ leaching of Li ions and the dynamic surface reconstruction of Co in the layered $LiCoO_{2-x}Cl_x$ (x = 0, 0.1 or 0.2), which subsequently transformed into a self-terminated, amorphous (oxy)hydroxide phase at lower electrochemical potentials during the OER.[194] As shown in the operando XANES (**Fig. 12a**), with Cl doping (x = 0.2), $LiCoO_{1.8}Cl_{0.2}$ underwent the oxidation of Co^{2+} to Co^{3+} and the leaching of Li at a lower potential (<1.40 V), whereas Cl-free $LiCoO_2$ underwent the oxidation at a higher potential (>1.40 V). However, the oxidation peak situated at 1.50 V was generally ascribed to the transition of Co^{3+} to Co^{4+} [195], of which the Co^{4+} cation was metastable, thus the valence state of Co reduced as the Co K-edge of $LiCoO_2$ reverted to the lower-energy position when the LSV scan ceased (**Fig. 12a**). In contrast, both $LiCoO_{1.8}Cl_{0.2}$ and $LiCoO_{1.9}Cl_{0.1}$ did not display any changes in the reconstructed valence state (Co^{3+}) during or after the OER, indicating that the Co^{3+} cations in the reconstructed Cl-doped $LiCoO_2$ were stable and the reconstruction process was irreversible. Moreover, the largest amorphous layer was found on the surface of cycled $LiCoO_{1.8}Cl_{0.2}$ in contrast to cycled $LiCoO_2$ as presented in **Fig. 12b**; this further confirmed that the Cl doping facilitated the in situ surface reconstruction during the OER. As supported by the ICP-MS results, there was no Co detected in either the cycled $LiCoO_{1.8}Cl_{0.2}$ or $LiCoO_2$; however, the proportion of Li extracted from $LiCoO_{1.8}Cl_{0.2}$ was much higher and the leaching process was quenched faster when compared to $LiCoO_2$. Consistent with the operando XANES results, the Li leaching in $LiCoO_{1.8}Cl_{0.2}$ started at 1.40 V for during the first CV cycle and terminated after 20 cycles; while for $LiCoO_2$, the Li diffusion was continued for 100 cycles, leading to a delay in the completion of the surface reconstruction process.

Combined with the loss of surface Li and the presence of Cl in $LiCoO_{1.8}Cl_{0.2}$ in STEM-EDS results, it could be inferred that the reconstructed layer was constituted by Cl-containing Co (oxy)hydroxide. Therefore, it was concluded that Cl doping rationally manipulated the in situ surface reconstruction of $LiCoO_2$, with the oxidation of Co^{2+} to Co^{3+}, via engineering the Li leaching process degree, as illustrated in **Fig. 12c**, while Cl-free $LiCoO_2$ generated the spinel-typed layer ($Li_{1\pm x}Co_2O_4$) accompanied by oxidizing Co^{3+} into Co^{4+} due to the unfavorable Li leaching.

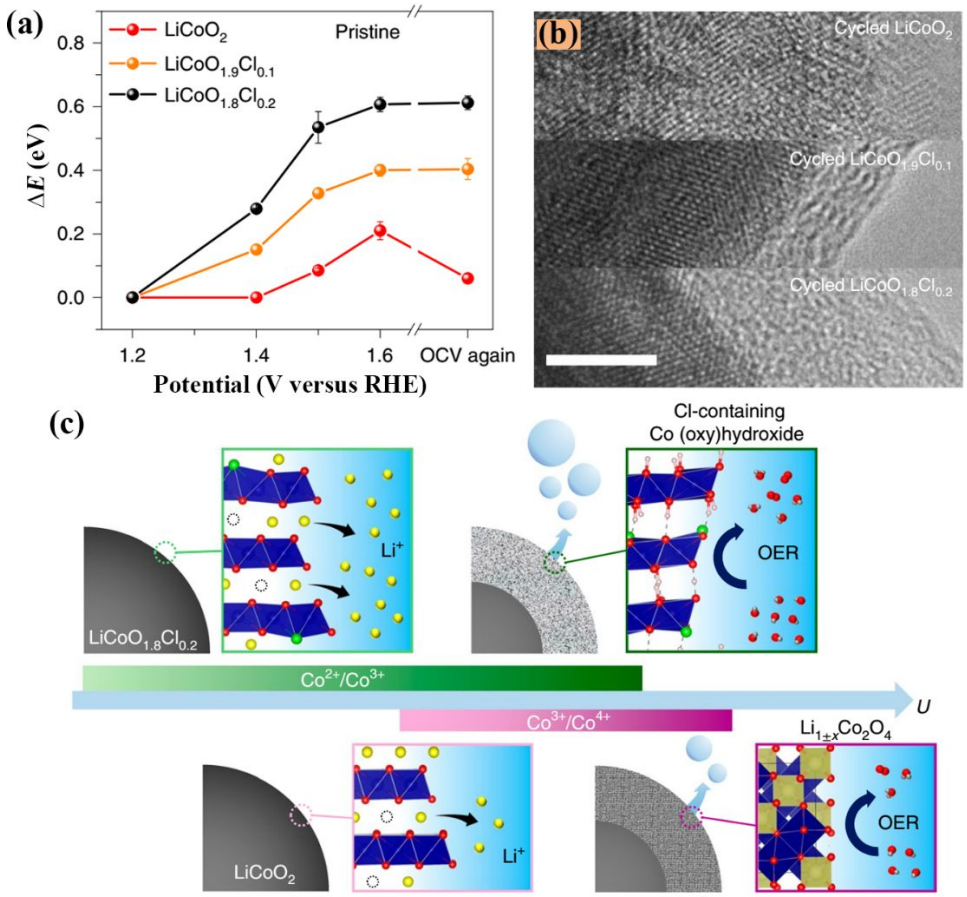

Fig. 12 (a) Tendency of Co K-edge shift originated from XANES spectra at varied electrochemical potentials and (b) TEM images for $LiCoO_2$, $LiCoO_{1.9}Cl_{0.1}$ and $LiCoO_{1.8}Cl_{0.2}$. Scale bar in (b) is 5 nm. (c) Scheme illustrating the in situ surface reconstruction process of $LiCoO_2$ and $LiCoO_{1.8}Cl_{0.2}$ during the OER. Reproduced with permission from ref. 194. Copyright 2021, Springer Nature.

4.3 Defects-rich-promoted

Atomic defect engineering has been widely accepted as an efficient method for electronic structure regulation and interface coordination, thus allowing the rational design of electrocatalysts with optimized electrocatalytic activity. Generally, the introduction of oxygen vacancies (V_O) into Co_3O_4-based OER catalysts would significantly improve the electronic conductivity and produce more Co sites with low oxidation state (Co^{2+}), which was considered to be the definitive role of V_O.[196, 197] However, it seems to be contradictory that the low-valence-state Co sites achieved improved OER activity, while it was preferentially-accepted that high-valence-state metal cations are more conducive to attaining highly active OER catalysts. Thus, thorough investigation of the intrinsic role of V_O in OER was required, especially in the dynamic reconstruction during the OER, which may be the underlying cause for these conflicting phenomena. Wang and co-workers unveiled the mechanism of V_O on improving the Co_3O_4-based OER via various (quasi-) operando/ex situ techniques including operando electrochemical impedance spectroscopy (EIS), electron paramagnetic resonance (EPR), quasi-operando XPS, and operando EXAFS, which proved that the V_O would initiate the dynamic reconstruction of defective Co_3O_4 and facilitate the oxidation of Co^{2+} at lower applied potential in comparison to pure Co_3O_4.[198] According to the electrochemical tests (operando EIS as shown in **Fig. 13a** and **13b**), the oxygen vacancy-rich Co_3O_4 (V_O-Co_3O_4) preferred to form the Co–OOH$^{\bullet}$ species due to the accelerated adsorption of the OH^- ions by oxygen vacancy, i.e., expedite the charge transfer and improve the deprotonation ability. In addition, the operando EXAFS further confirmed that the dynamic reconstruction of the active species occurred at relatively lower potential for V_O-Co_3O_4 in comparison to pure Co_3O_4 (**Fig. 13c** and **13d**). It is noteworthy that V_O-Co_3O_4 exhibited a faster oxidation of Co ions than that of pure Co_3O_4 during the deprotonation process prior to the OER. This was related to the effect of the V_O, which would reduce the adsorption energy of OH^- on Co sites to generate Co–OH$^{\bullet}$ species, and then underwent a faster deprotonation process at lower potential to generate active Co–OOH$^{\bullet}$ species. Based on the above results, it could be clarified the mechanism of V_O-promoted reconstruction of Co_3O_4 during the OER, which the V_O benefited the adsorption of OH^- and accelerated the reconstruction process, thus accounting for the boosted OER activity.

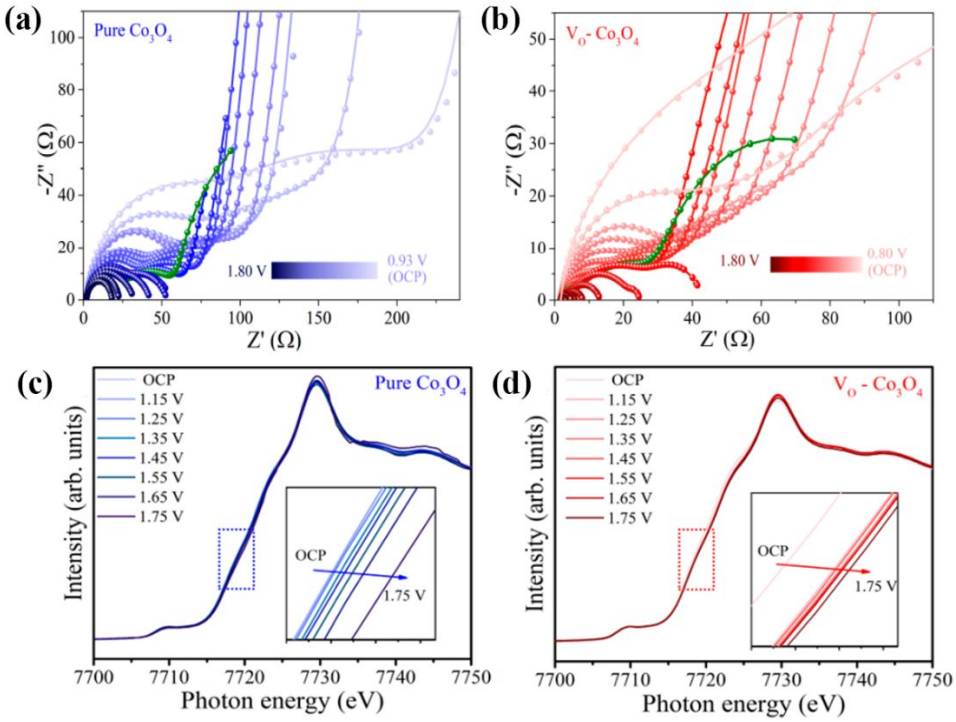

Fig. 13 Operando EIS measurements for (a) pure Co_3O_4 and (b) V_O-Co_3O_4 catalysts at various voltages in 1.0 M KOH. The green curves represent the potential of 1.5 V. Operando Co K-edge EXAFS spectra of (c) pure Co_3O_4 and (d) V_O-Co_3O_4. Insets, zoom in the regions of dotted boxes. Reproduced with permission from ref. 198. Copyright 2020, American Chemical Society.

Apart from oxygen vacancies, cation vacancies can also be introduced to regulate the intrinsic properties of electrocatalysts, the dynamic reconstruction processes, and the related electrocatalytic activities. For example, Song et al. applied a hydrolysis strategy to successfully prepare nickel hydroxide (α-NiOOH) with tunable concentrations of nickel vacancy (V_{Ni}), of which the V_{Ni} was of great account in the reconstruction into active γ-NiOOH species during surface reconstruction.[65] In contrast to oxygen vacancies, the introduction of V_{Ni} increased the oxidation state of Ni and then generated more energetic Ni^{3+} in V_{Ni}–rich α-NiOOH (denoted V_{Ni}-α-$Ni(OH)_2$-x, the V_{Ni} concentration x = 1, 2, 3, and 4), since the Ni K-edge in the XANES spectra showed positive shifts with the increasing V_{Ni} concentration, suggesting the increasing oxidation state in V_{Ni}-α-$Ni(OH)_2$-x. The peak intensities of Ni–Ni bonds in the EXAFS spectra decreased when the V_{Ni} concentrations increased, indicating a reduced coordination number (CN) caused by V_{Ni}. Correspondingly, the V_{Ni}-α-$Ni(OH)_2$-x catalyst with highest V_{Ni}

concentration achieved the best catalytic activity and the largest oxidation peaks of Ni^{2+}/Ni^{3+} during the OER measurements, which implied that the generation of active species (NiOOH) from reconstruction was promoted by V_{Ni}. DFT calculations further confirmed that the defective α-NiOOH with high V_{Ni} concentration acquired an accelerated charge transfer and increased electronic conductivity, thus promoting the reconstruction into the active species while also benefiting the oxygen evolution activities.

4.4 Morphology-tuned

Apart from atomic defect engineering, optimizing the morphology and size of electrocatalysts to maximize the amount of exposed active sites is another viable means of boosting the OER activity.[3] More importantly, due to the limitations of electrolyte penetration, it is difficult to achieve a complete reconstruction of catalysts during the electrochemical process when a certain thickness of reconstructed dense layer is formed. Therefore, downsizing the electrocatalyst particles is conducive to better contact between the electrolyte and catalysts, resulting in a deeper level of reconstruction possible. Mai et al. found that ~5 nm was the deepest reconstructed NiOOH layers attainable using the bulk Ni precatalyst. In this respect, they presented a strategy involving the lithiation of Ni nanoparticles to reduce the particle to a ultrasmall size (sub-10 nm); then a deep reconstruction (DR) of Ni into active NiOOH was realized.[22] Herein, a one-cycle lithiation process was employed to synthesize the ultrasmall Ni nanoparticles. The Ni nanoparticles were pre-oxidized into NiO during the synthesis process because of their oxygen-sensitive nature; through this strategy, post-lithiation Ni nanoparticles grown on nickel foam was achieved (denoted lithiated NiO@NF). The obtained lithiated NiO@NF was then treated with an electro-oxidation process in alkaline electrolyte, resulting in the deep reconstruction of NiO into NiOOH species (denoted DR-NiOOH). In situ Raman measurements (**Fig. 14a**) further verified NiOOH as the OER active species when the lithiated NiO@NF applied as the working electrode, of which the two emerged Raman peaks located at 474 and 554 cm^{-1} during LSV tests suggested the Ni–O bonds vibration in NiOOH.[199] Furthermore, in comparison to the reconstructed core-shell Ni@NiOOH originated from the oxidation of the Ni particles without lithiation (denoted Ni@NiOOH/NF), the DR-NiOOH showed higher OER activity with significantly decreased overpotential (**Fig. 14b**). This could

be ascribed to that the deep reconstruction of the catalysts presenting more catalytically active NiOOH species, while the uncompleted one (Ni@NiOOH/NF) possessed an inactive inner core (Ni). It has been generally considered that there would be an electronic interaction of the core/shell in catalysts; however, it should be noted that the electronic effects of Ni core on the NiOOH shell would be neglected when the shell thickness was larger than three layers (> 0.5 nm).[200] Future work regarding the systemic investigation of the deep or complete reconstruction mechanisms, in addition to the synergistic effect between reconstructed layers and the pristine catalysts on the OER activity, is still required in order to produce high-efficiency OER catalysts.

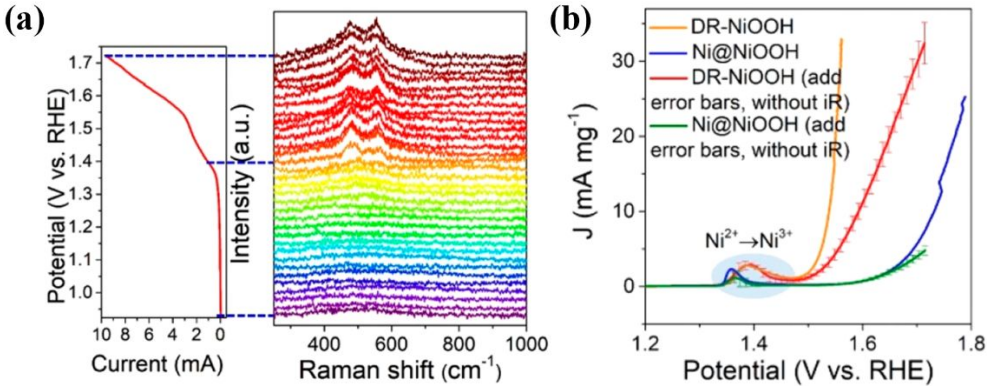

Fig. 14 (a) LSV curve of the lithiated NiO@NF electrode and the corresponding in situ Raman spectra recorded at a potential interval (ΔV of 25 mV) from 0.924 to 1.724 V vs. RHE. (b) Mass activity of DR-NiOOH and Ni@NiOOH with and without *iR* compensation. Reproduced with permission from ref. 22. Copyright 2019, American Chemical Society.

4.5 Plasmon-enhanced

The utilization of the surface plasmon resonance (SPR) to enhance the activities of OER electrocatalysts has attracted great research interest in recent years. To provide a brief overview of SPR, by illuminating plasmon nanomaterials, such as noble Au and Ag nanostructures, the electrons are excited (now so-called hot electrons) by the resonant photons and then transported into attached substrates; meanwhile, the holes (defined as hot holes) remain on the surface of the plasmon materials.[201] This process will cause a photovoltaic effect, which is favorable for solar energy conversion, but more importantly, could serve as a novel strategy to effectively

promote the production of high-oxidation-state active species during the OER due to the assistance of hot holes with strong oxidizing ability. Therefore, for plasmon-enhanced transition-metal-based OER electrocatalysts, researchers have proposed the mechanism responsible for the activity improvement was primarily considered to be the more efficient generation of high oxidation state active sites caused by the hot holes. Ye and co-workers reported a representative work on plasmon-enhanced OER, in which a significantly improved OER activity, specifically a decreased overpotential and lowered Tafel slope, was observed in Au-nanoparticle-decorated $Ni(OH)_2$ nanosheets ($Ni(OH)_2$-Au) after irradiation under a 532 nm laser (denoted $Ni(OH)_2$-Au (light)).[202] By comparing the CV scans of $Ni(OH)_2$ and $Ni(OH)_2$-Au with and without irradiation, it was observed that the integrated area of the $Ni^{2+}/Ni^{3+/4+}$ oxidation peaks for $Ni(OH)_2$-Au increased under irradiation ($Ni(OH)_2$-Au (light)) (**Fig. 15a**); this promoted oxidation of Ni^{2+} to $Ni^{3+/4+}$ in $Ni(OH)_2$-Au was ascribed to the SPR effect. The authors proposed that, during the plasmon-enhanced OER, the hot holes generated on Au nanoparticles facilitated the inactive Ni^{2+} to reconstruct into active $Ni^{3+/4+}$, subsequently increasing OER activity, while the plasmon-induced hot electrons were transferred to the electrode (glassy carbon, GC) under the external applied potential (**Fig. 15b**). Similar results have also been observed for CoO-Au and FeOOH-Au catalysts, indicating the generality of plasmon-enhanced OER.[202] Nonetheless, more thorough studies on the plasmon-enhancement mechanism via in situ spectroscopy techniques are still needed to clarify the catalytically active site and to gain further insight on the dynamic variation of valence states and coordination environments within the system.

Inspired by the SPR effect on noble-metal nanostructures, Zhang et al. employed a photo-generated-carrier-driven strategy based on transition-metal/semiconductor (Ni/NiO) electrocatalysts for OER.[203] It was observed that the oxidation peak of $Ni^{2+}/Ni^{3+/4+}$ negatively shifted and the peak area correspondingly increased as the irradiation time was extended from 0 to 15 min (**Fig. 15c**), indicating that the generation of the catalytically active Ni species was promoted under irradiation. A significantly improved OER performance with lower onset overpotential, smaller Tafel slope, and higher mass activity was achieved for the Ni/NiO electrode under light irradiation. Based on the photo-driven semiconductor excitation of NiO, the following OER improvement mechanism was proposed: the photo-generated holes in NiO

would promote the oxidation of slightly active Ni^{2+} to highly active $Ni^{3+/4+}$, while the remaining electrons were transferred to the electrode (nickel foam) under the applied potential (**Fig. 15d**).

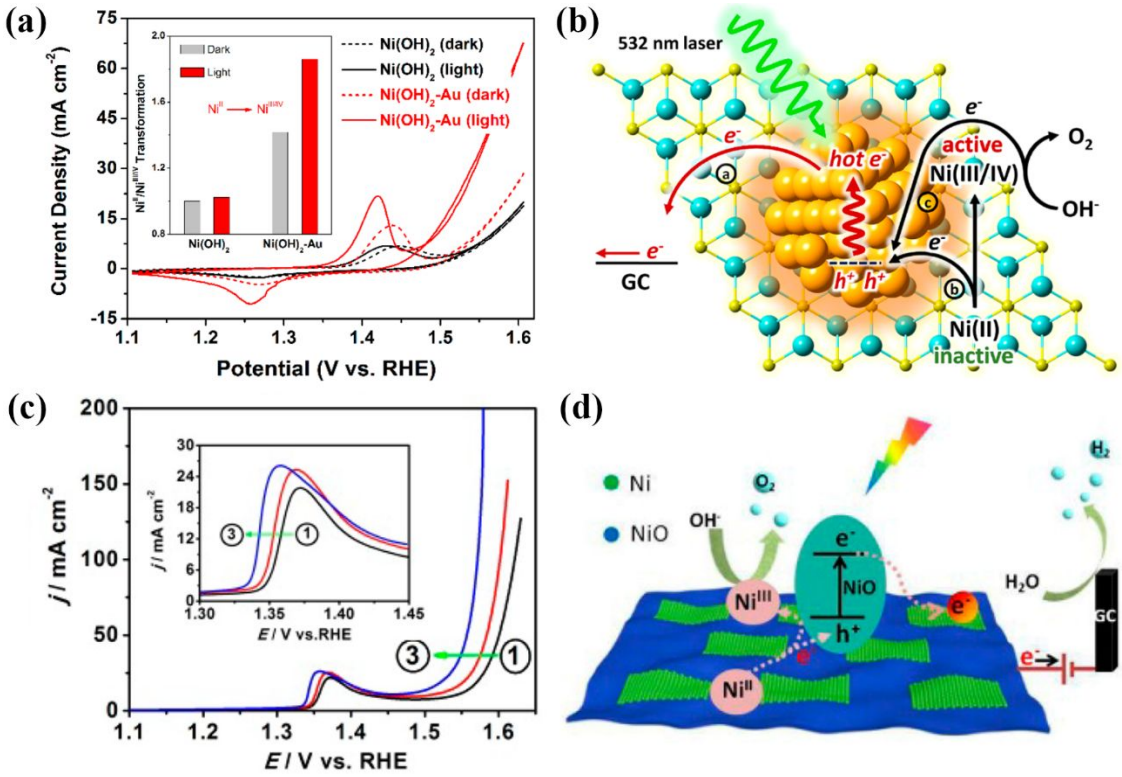

Fig. 15 (a) CV curves for $Ni(OH)_2$ nanosheets and $Ni(OH)_2$-Au hybrids with and without 532 nm laser irradiation. Inset, the corresponding transformation of $Ni^{2+}/Ni^{3+/4+}$ derived from CV curves. (b) Schematic illustration of electron transfer pathways in the $Ni(OH)_2$-Au electrode when irradiation with 532 nm laser. Reproduced with permission from ref. 202. Copyright 2016, American Chemical Society. (c) *iR*-corrected LSV curves of Ni/NiO-NF with various irradiation durations. (d) Schematic diagram illustrating the mechanism of photo-generated-carrier-driven OER process. Reproduced with permission from ref. 203. Copyright 2017, American Chemical Society.

4.6 Thermal/photothermal-enabled

It has been well accepted that increasing the temperature (T) during OER could achieve larger current density (*j*) at lower overpotential and faster kinetics of water splitting; resulting in an improved catalytic efficiency, as demonstrated by the following Arrhenius' law (eqn (11)).[204]

$$j = A \exp(-E_a/RT) \quad (11)$$

where *j* is current density, A is pre-exponential factor, E_a is activation energy, R is gas constant and T is temperature.

Due to these advantages, assisted by thermal energy has been applied to facilitate electrocatalytic conversion. Very recently, Mai et al. realized the thermally induced complete reconstruction (TICR) of a nickel molybdate ($NiMoO_4$) pre-catalyst during alkaline OER at 51.9 ^oC (denoted cat.-51.9).[23] As shown in the HRTEM images (**Fig. 16a-d**), the reconstruction depth of $NiMoO_4$ increased with rising treatment temperatures. At each temperature, the NiOOH phase was identified, and at 51.9 ^oC, no phase boundary could be observed, suggesting the complete reconstruction of $NiMoO_4$. Additionally, in situ Raman and chronopotentiometric measurements were simultaneously performed for two different temperatures, 25 ^oC and 52 ^oC, to further confirm that complete reconstruction was achieved at 52 ^oC (**Fig. 16e** and **f**); at 52 ^oC, the Raman peaks of $NiMoO_4$ completely disappeared and the increased generation of OER-active (oxy)hydroxide species caused the potential to gradually decrease, as shown in the chronopotentiometric curve (**Fig. 16f**). After 60 h chronopotentiometric measurements, cat.-51.9 required the lowest overpotentials (274.1, 282.3, 288.0, and 293.2 mV) to reach the same respective current densities (15, 20, 25, and 30 mA cm^{-2}) among all electrodes tested at different temperatures (cat.-25.0, cat.-32.4, cat.-39.6, and cat.-51.9). Apart from $NiMoO_4$, they also proved that such TICR strategy also can realize the complete reconstruction of the $CoMoO_4$ into the highly active CoOOH. While the TICR strategy shows promising potential to efficiently activate surface reconstruction, it is important to consider that, by directly heating the electrolyte, the increased electrolyte temperature leads to a deviation from standard condition and, thus, changes the theoretical decomposition potential of water to some extent.

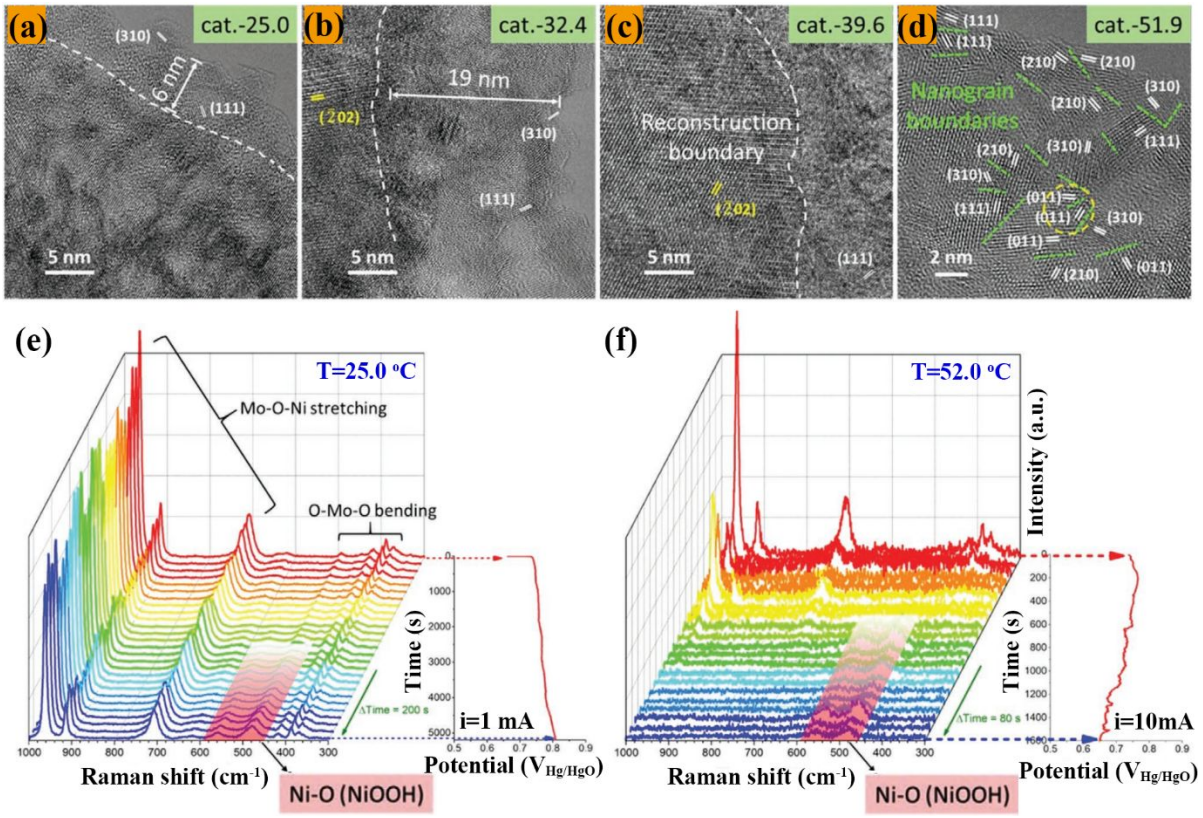

Fig. 16 (a-d) HRTEM images of the post-OER catalysts at different temperature, (marked as cat.-T, T = 25.0, 32.4, 39.6, 51.9). The inset white dotted lines are for visual guidance of the reconstruction boundary. (e) In situ Raman spectra performed at low temperature and the corresponding chronopotentiometric curve of $NiMoO_4$ recorded at each 200 s in 1.0 M KOH (T = 25.0 °C). (f) In situ Raman spectra performed at high temperature and the corresponding chronopotentiometric curve of $NiMoO_4$ recorded at each 80 s in 1.0 M KOH (T = 52.0 °C). Reproduced with permission from ref. 23. Copyright 2020, Wiley-VCH.

To avoid the issue of significantly changing the whole electrocatalytic system, namely by increasing the temperature of the electrolyte, while still benefiting from the increased degree of surface reconstruction, the utilization of electrocatalysts which enable the ability of the photo-to-thermal conversion (defined as photothermal electrocatalysts) is particularly promising. Photothermal electrocatalysts possess in situ heating during the OER caused by photothermal effect when illuminated with visible or near infrared (NIR) light, thus effectively confining the production of heat in a defined region (i.e., the working electrode) as well as avoiding the complex use of extra devices to provide thermal energy.[205] To fill this knowledge

gap concerning photothermal-promoted electrocatalysis, a recent study by Lin et al. provided in-depth insights into the assistance of the photothermal effect, originated from spinel $NiFe_2O_4$ nanoparticles (NFO NPs), for promoting electrocatalytic activity.[24] Firstly, as modeled by a computational method, i.e., the finite-element method (FEM) (**Fig. 17a**), both the isolated NFO NP (d = 12 nm) and the seven NFO NPs assembled together in close proximity presented the electric-field distributions when excited under 808 nm NIR light in addition to the temperature distributions surrounding the NFO NPs, confirming that NFO NPs are capable of converting light into heat. Then, as the system was exposed to NIR light, the OER activity of NFO NPs on nickel foam (NFO/NF) was progressively increased, since the higher current densities across all potentials and gradually decreased overpotentials (at current density of 20 mA cm^{-2}) were obtain (**Fig. 17b**). In comparison to the bare nickel foam electrode with E_a of 147.62 kJ mol^{-1}, the NFO/NF electrode with photothermal effect only required a much lower E_a of 98.50 kJ mol^{-1} (**Fig. 17c**), indicating a reduced energy barrier and superior kinetics for OER. This could be ascribed to the more drastic reactant-molecule activation caused by the thermal energy, making it much easier to overcome the activation barrier during the OER.[206] Furthermore, an operando Raman spectra-electrochemistry study revealed that active γ-NiOOH species were formed at a relatively lower potential of 1.36 V in the surface reconstruction process aided by the photothermal effect (**Fig. 17d**), in comparison to the case without photothermal assistance. NFO/NF with photothermal effect displayed newly emerged Raman peaks at 474 and 554 cm^{-1}, which were ascribed to γ-NiOOH. These peaks showed much higher ratios ($\Delta I_2'$ and $\Delta I_1'$) than the original NFO peak (692 cm^{-1}) without photothermal effect (ΔI_2 and ΔI_1), further proving the reconstruction into γ-NiOOH species was more thorough when there was the presence of photothermal effect. Therefore, such transition-metal-based materials including oxides, sulfides, phosphides, etc., possessing the function of photothermal conversion are expected to encourage the elaborate design of highly effective OER electrocatalysts, among which the localized heating coupled with electrochemistry should be a promising direction.

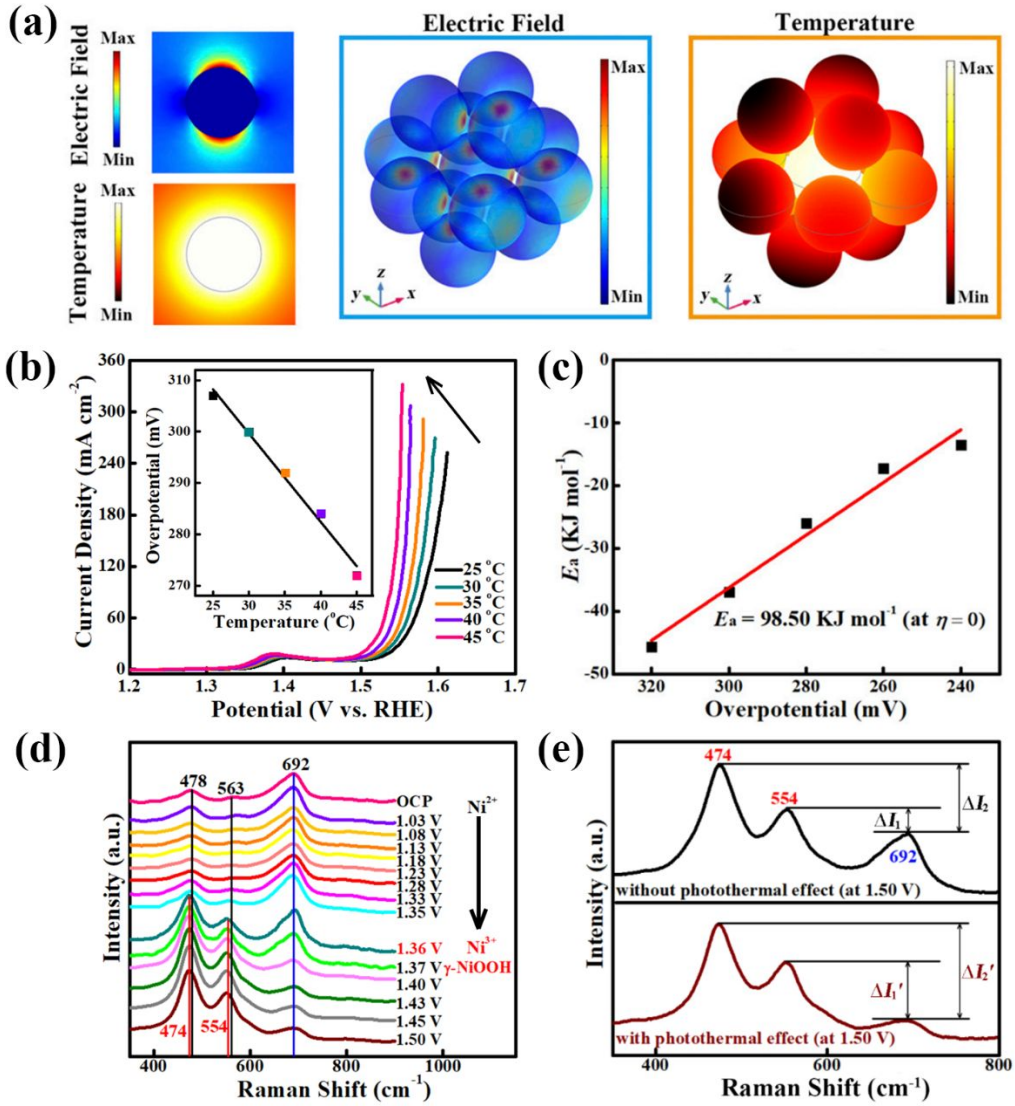

Fig. 17 (a) Distributions of electric field (*Upper Left*) and temperature (*Lower Left*) for an isolated NFO NP (d = 12 nm), as well as distributions of electric field (*Center*) and temperature (*Right*) for seven NFO NPs (d = 12 nm), as modeled by FEM. (b) LSV curves of NFO/NF electrode with photothermal effect. Inset, tendency of overpotential at j = 20 mA cm^{-2} along with the rising temperature. (c) Relationship between E_a and overpotentials. (d) Operando Raman spectra of NFO/NF with photothermal effect from OCP to 1.50 V vs. RHE in 1.0 M KOH. (e) Operando Raman spectra of NFO/NF electrode without and with photothermal effect at 1.50 V vs. RHE in 1.0 M KOH. ΔI_1 and $\Delta I_1'$ represent the peak intensity difference between 554 cm^{-1} and 692 cm^{-1} for the spectra of NFO/NF without and with photothermal effect, respectively. Similarly, ΔI_2 and $\Delta I_2'$ represent the peak intensity difference between 474 cm^{-1} and 692 cm^{-1} for the spectra of NFO/NF without and with photothermal effect, respectively. Reproduced with permission from ref. 24. Copyright 2021, National Academy of Sciences.

Besides, some transition-metal-based catalysts that generally exhibited high OER activities, such as Co_3O_4, CoN, CoP, and CoS, also display photothermal behavior. For example, Liu et al. reported a markedly boosted electrocatalytic OER activity of Co_3O_4 by elevating the temperature via photo-to-thermal conversion under NIR light irradiation.[207] However, research on photothermal-promoted electrocatalysis is still in its infancy; future studies including in situ techniques and computational simulations are still needed in order to enrich the current understanding.

Table 5. Summary of different activation strategies for the representative OER catalysts.

Activation strategy	Catalyst	Original surface oxidation potential (V vs. RHE)	Promoted surface oxidation potential (V vs. RHE)	Reconstructed oxidation state/surface species/structure	Measurements for detecting surface reconstruction	Application (electrolyte)	Ref.
Metal-doping/substituting-facilitated							
Fe substitution	$CoAl_2O_4$	~1.41 V	~1.32 V	Co oxyhydroxides	in situ XAS	OER (1.0M KOH)	188
Introduction of Ce	$Ni(OH)_2$	1.41 V	1.27 V	γ-NiOOH	in situ Raman and operando XRD	OER (1.0M KOH)	174
Al modification	Ni_5P_4-Ni_2P	Not available	Not available	$Ni(OH)_2$/NiO	ex situ STEM and ex situ XPS	OER (1.0M KOH)	208
Ni^{3+}-rich	Ni–Co oxide	Not available	Not available	NiOOH	in situ XAS	OER (1.0M KOH)	209
Ni substitution	$ZnCo_2O_4$	Not available	Not available	CoOOH/NiOOH	ex situ XAS and ex situ XPS	OER (1.0M KOH)	210
Mo-enriched	Co-Mo_2C	Not available	1.40 V	γ-CoOOH	in situ Raman and ex situ STEM	OER (1.0M KOH)	211
Anions-induced							
F-incorporated	NiFe hydroxide	Not available	Not available	amorphous NiFe oxide	ex situ STEM and ex situ XPS	OER (1.0M KOH)	160
F-Substituted	CoO	Not available	Not available	amorphous layer with high Co^{3+}/Co^{2+} ratio	ex situ XPS	OER (1.0M KOH)	212
P-Substituted	$CoSe_2$	1.54 V	1.44 V	CoOOH	in situ XAS, in situ Raman, and ex situ LP-TEM	OER (1.0M KOH)	193
Cl-doping	$LiCoO_{2-x}Cl_x$	~1.504 V	< 1.40 V	amorphous Co (oxy)hydroxide	Operando XANES, ex situ TEM, ex situ	OER (1.0M KOH)	194

				with Co^{3+}	HAADF-STEM, and ex situ ICP-MS		
Defect-rich-promoted							
Oxygen vacancy-rich	Co_3O_4	1.55 V	1.15 V	Co-OOH•	quasi-operando XPS, operando EIS and operando EXAFS	OER (1.0M KOH)	198
Nickel vacancy-rich	α-NiOOH	~0.355 V	~0.355 V	γ-NiOOH	ex situ XAFS, ex situ XPS and LSV	OER (1.0M KOH)	65
Morphology-tuned							
Lithiation	Ni	Not available	~1.38 V	NiOOH	in situ XRD, in situ Raman, and ex situ TEM	OER (1.0M KOH)	22
Plasmon-enhanced							
Surface plasmon resonance of Au	$Ni(OH)_2$	1.42 V	Not available	NiOOH ($Ni^{3+/4+}$) active species	ex situ ESR and ex situ XPS	OER (1.0M KOH)	202
Photogenerated holes	Ni/NiO	1.40 V	Not available	$Ni^{3+/4+}$ active species	ex situ XPS	OER (1.0M KOH)	203
Thermal/photothermal-enabled							
High temperature (51.9 °C)	$NiMoO_4$	Not available	Not available	NiOOH	ex situ HRTEM and in situ Raman	OER (1.0M KOH)	23
Photothermal effect	N-CNTs/Ni_3Fe/TiO_{2-x}	1.50 V	Not available	Highly oxidative nickel	LSV	OER (1.0M KOH)	213
Photothermal effect	Co_3O_4	1.38 V	< 1.38 V	Co^{4+} species	LSV	OER (1.0M KOH)	207
Photothermal effect	$NiFe_2O_4$	1.41 V	1.36 V	(Ni,Fe)OOH	Operando Raman, ex situ HRTEM and ex situ XPS	OER (1.0M KOH)	24

5. Investigation into surface reconstruction

The development of modern spectroscopy and microscopy measurements, especially the advancements made in operando and in situ techniques, render it possible to clearly recognize the dynamic reconstruction of catalysts under operating conditions, such as structure, composition and electronic configuration, as well as the in situ adsorption/desorption of reaction intermediates. Regarding distinguishing between in situ and operando, it is widely accepted that operando is representative of a measurement performed under an ongoing

condition; for example, the operando Raman is commonly conducted during the electrochemical catalytic process. Meanwhile, in situ is generally used to describe where a reaction takes place or a measurement taken in the original position.[27, 214] Nevertheless, it is difficult to conduct a thorough investigation of the mechanisms of oxygen evolution and electrochemical reconstruction through only a single operando data. Combining complementary ex situ methods that provide the physical and chemical properties of the catalysts before and after the electrochemical process, researchers can gain insight into the dynamic reconstruction process and the identification of the actual active species. In addition, DFT calculations have been considered a high-accuracy and valid means to further confirm the active sites and elucidate the mechanism of electrochemical water splitting.[215, 216] There are already several reviews which have summarized the characterizations and theoretical simulations of the OER catalysts.[27, 32, 214] In this section, only a few representative studies of operando and in situ characterizations for detecting the dynamic reconstruction of the catalysts in OER, as well as the DFT calculations are recapitulated here.

5.1 Operando/in situ technique analysis

X-ray absorption spectroscopy (XAS) is a broadly welcomed technique that affords detailed information on the local atomic structure, coordination environment, chemical bonding and oxidation state, and is especially useful in electrocatalysis research. Particularly, operando XAS (**Fig. 18a**) has been employed to monitor the dynamic reconstruction process on catalyst surfaces.[16] Tan et al. employed operando XAS measurements to establish the dynamic variations in oxidation state and local coordination environment of Ir, Ni, and Fe in isolated Ir atoms on free-standing nanoporous NiFeO (denoted np-Ir/NiFeO) (**Fig. 18b-g**).[138] As the potential was increased, both the coordination number of Ir-O bonds and valence state of Ir were increased; however, it displayed no change in coordination number when continually applied the potential to 1.55 V (**Fig. 18b** and **c**). This may be ascribed to the transformation of Ir-OH into Ir-O□ via a deprotonation process, which would occur on the Ir site under higher potentials and lead to the continued oxidation of Ir without altering the coordination environment. The positive shifts seen in both the Ni and Fe XANES spectra (**Fig. 18d** and **f**) evidenced an oxidation process, with the Ni and Fe oxyhydroxides species being further

generated under high potentials (1.45 and 1.55 V). The corresponding negative shifts (Ni-O, Ni-P and peak I) in the FT-EXAFS spectrum of Ni (**Fig. 18e**) demonstrated the shrinkage of bonds, which was consistent with the isolated Ir atoms on the surface of np-Ir/NiFeO, resulting in a preventable aggregation during the OER. While no significant change was found in the Fe FT-EXAFS spectrum (**Fig. 18g**), this may be ascribed to the relatively decreased amount of Fe on the surface to enrich the variation during OER. Moreover, compared to the sample without Ir atoms (np-NiFeO), a larger shifts in np-Ir/NiFeO indicated a promoted transformation into Ni(Fe) oxyhydroxides during the oxidizing process.

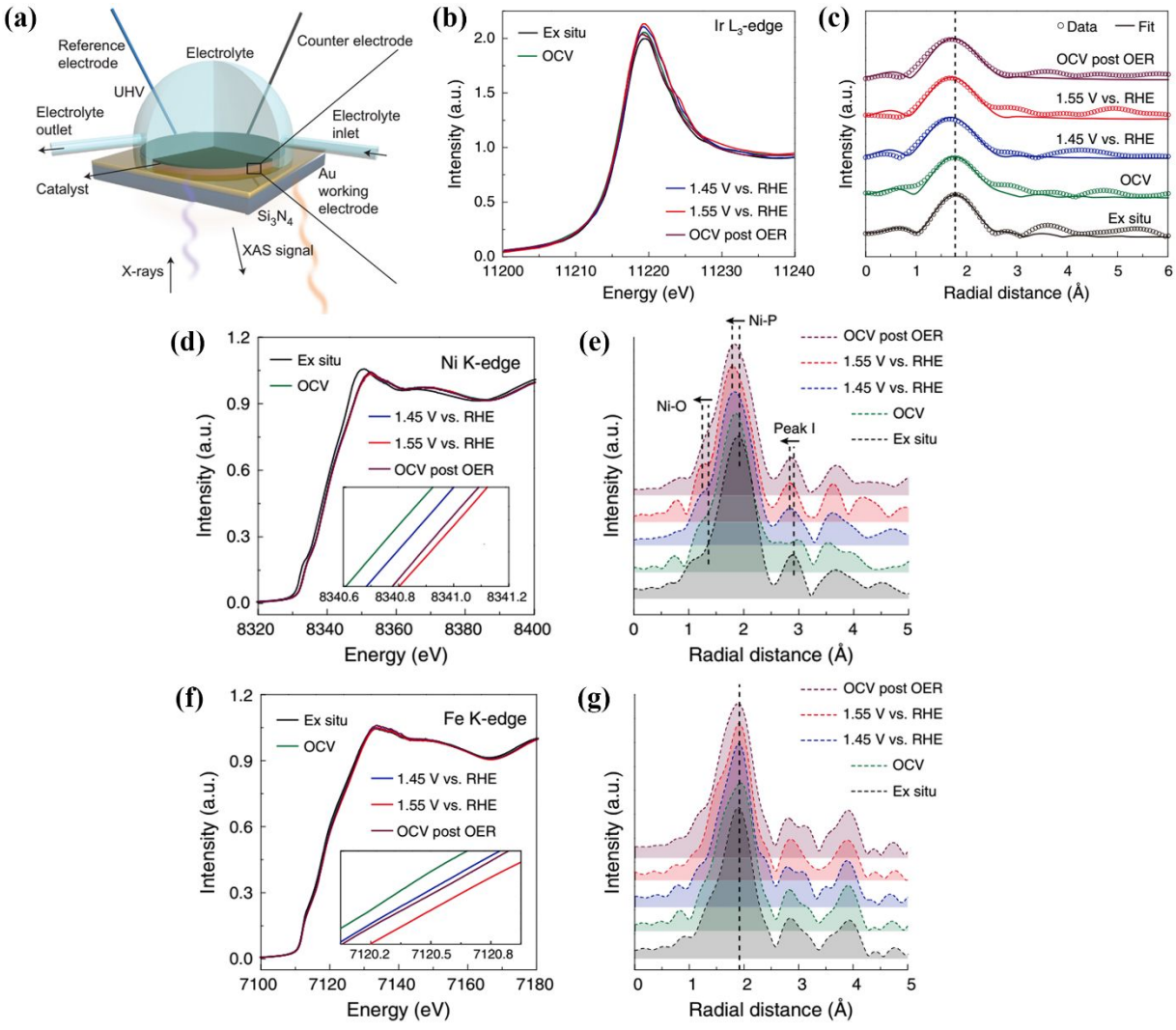

Fig. 18 (a) Schematic of the in situ electrochemical flow-cell-enabled operando XAS. Reproduced with permission from ref. 16. Copyright 2018, Springer Nature. (b) Operando Ir L_3-edge XANES spectra and (c) corresponding FT-EXAFS spectra of np-Ir/NiFeO under

varied applied potentials from OCV to 1.55 V vs. RHE in 1.0 M KOH. (d) Operando Ni K-edge XANES spectra and (e) corresponding FT-EXAFS spectra of np-Ir/NiFeO under varied applied potentials from OCV to 1.55 V vs. RHE in 1.0 M KOH. (f) Operando Fe K-edge XANES spectra and (g) corresponding FT-EXAFS spectra of np-Ir/NiFeO under varied applied potentials from OCV to 1.55 V vs. RHE in 1.0 M KOH. Reproduced with permission from ref. 138. Copyright 2020, Springer Nature.

The operando Raman spectroscopy (**Fig. 19a**), with the scan range from 100 to 4000 cm^{-1}, has been extensively adopted to detect the in situ phase transitions and generation of intermediates under working conditions.[23] Particularly, using operando Raman technique, the dynamic transformations of Ni- and Co-based catalysts into oxyhydroxides (NiOOH and CoOOH, respectively) can be easily probed upon applied potentials. Nevertheless, there is still a debate on the evidences of FeOOH species formed in NiFe-based catalysts via Raman measurements. As reported by Hu et al., the Raman features of γ-FeOOH were unable to be observed in the NiFe layered double hydroxide (LDH) when the Fe content is up to 28%.[217] Very recently, they applied the operando Raman measurements as well as the oxygen isotope labeling experiments to compare the two kinds of NiFe-based catalysts, that is, FeOOH-NiOOH and NiFe LDH.[218] It was found that the γ-FeOOH species distributed on the surface of FeOOH-NiOOH, but not in NiFe LDH; this could be attributed to major Fe ions occupied the bulk of NiFe LDH but the surface of FeOOH-NiOOH. Subsequently, the isotope experiments were carried on through immersing the ^{16}O-labeled samples into the ^{18}O-KOH electrolyte. As shown in **Fig. 19b**, at potentials ≤ 1.3 V, there were shifts in the Ni^{2+}–O and Ni^{2+}–OH peaks for FeOOH-NiOOH, which could not be distinguished because of the overlapping, while no change of FeOOH peak was seen. For NiFe LDH (**Fig. 19c**), at potentials ≤ 1.35 V, the Ni^{2+}–O and Ni^{2+}–OH peaks appeared positive shifts, which demonstrated that the ^{16}O was replaced by the ^{18}O of the electrolyte. Upon applying the potential of 1.55 V, the generation of NiOOH could be clearly observed, with Ni^{3+}–O peaks appearing in both FeOOH-NiOOH and NiFe LDH. The positive shifts of the Ni^{3+}–O peaks in FeOOH-NiOOH and NiFe LDH illustrated the effect of the O isotope exchange. However, for FeOOH, there was an exchange of the lattice oxygen during the OER. Furthermore, as the ^{18}O-labeled samples were placed back into the

^{16}O-KOH electrolyte, the Raman results showed that there was an exchange of lattice O in FeOOH-NiOOH but not in NiFe LDH, suggesting two different mechanisms for these two benchmark OER catalysts in alkaline electrolyte. Coupled with the OER performances in Tafel slopes and rate orders of [OH^-], the authors pointed out that for FeOOH-NiOOH, in the rate-determining step, the O_2 formation depended on the reaction between the Fe=O sites, the extrinsic OH^-, and the Ni^{3+}–O. While for NiFe LDH, the O_2 formation was accomplished by a successive proton-coupled-electron-transfer process (PCET), of which the Fe=O center reacted with OH^- and, after further oxidation, produced O_2.

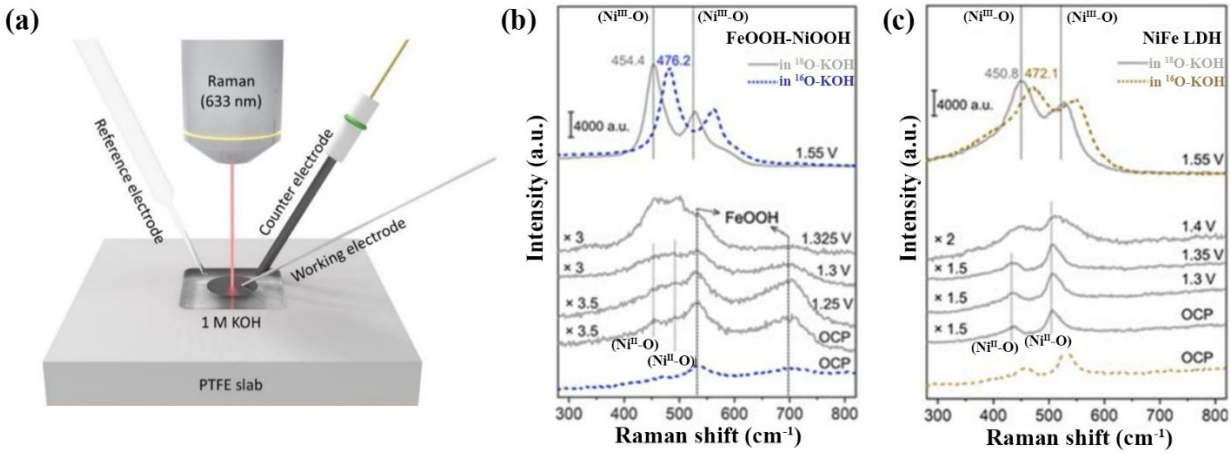

Fig. 19 (a) Schematic illustration of operando Raman spectroscopy consisted of a Raman-electrochemistry coupling system. Reproduced with permission from ref. 23. Copyright 2020, Wiley-VCH. Operando Raman spectra of (b) FeOOH-NiOOH and (c) NiFe LDH from OCP to 1.55 V vs. RHE in 1.0 M KOH-$H_2{}^{18}O$ solution. Reproduced with permission from ref. 218. Copyright 2020, Wiley-VCH.

The formation of Fe species, such as the unobserved Fe^{4+} species in Raman spectra, can be directly captured by operando Mössbauer spectroscopy when carrying on the steady-state OER reaction. Stahl et al. found the existence of Fe^{4+} species in NiFe catalyst via applying operando Mössbauer measurement, which originated from the stabilizing effect of the NiOOH lattice.[219] Besides, the XPS can also be applied to characterize the oxidation states and elemental compositions. However, due to the requirement of an ultrahigh vacuum during the testing procedure, it can only be utilized for ex situ analyses of OER catalysts. Recently, the

ambient pressure X-ray photoelectron spectroscopy (AP-XPS) conducted with synchrotron radiation sources, which can avoid the ultrahigh vacuum requirement, has been developed for the in situ characterization of surface chemistry. For example, Yano et al. employed the operando AP-XPS and XAS to investigate the chemical and structural reconstruction of the quinary oxides (Ni-Fe-Co-Ce)O_x.[220] The operando AP-XPS results indicated that the surface of the oxides underwent electrochemical activation at low overpotential, driving the transformation of $(Ni,Fe,Co)^{2+}(OH)_2$ into the $(Ni,Fe,Co)^{3+}O(OH)$ phase; interestingly, only a partial oxidative conversion of Ni and Co was observed. Furthermore, the operando XAS findings suggested a significant difference between the bulk and surface Co in the electrocatalysts. The bulk portion showed a partial oxidation from Co^{2+} to Co^{3+}, while it may keep the mixed oxide $Co^{2+}O•{Co^{3+}}_2O_3$ with an increased Co^{3+} content when immersed in the electrolyte. Conversely, the surface was reduced to $Co^{2+}(OH)_2$ when immersed in the electrolyte and subsequently oxidized into the oxyhydroxide ($Co^{2+/3+}O_x(OH)_y$) under catalytic conditions, which is in accordance with the operando AP-XPS results.

Apart from the composition and electronic structure probed by the above spectroscopy techniques, in situ transmission electron microscopy (TEM) can provide information on the structural and morphological changes of electrocatalysts under real-time observation. Recently, Ersen et al. implemented the in situ electrochemical TEM (in situ EC-TEM, **Fig. 20a**) with a liquid electrochemical Poseidon TEM holder (**Fig. 20b**) to observe the reconstruction of Co_3O_4 nanoparticles during the OER process in different aqueous electrolytes.[221] Nevertheless, it would be a challenge to capture the surface reconstruction of the catalysts via in situ EC-TEM due to the specimen damage and atom movements caused by the electron beam.[222] In this respect, Yu et al. employed pseudo-in situ TEM to identify the morphology change on the very same location of CoS_x on the carbon grid along with the OER proceeding for different times.[20]

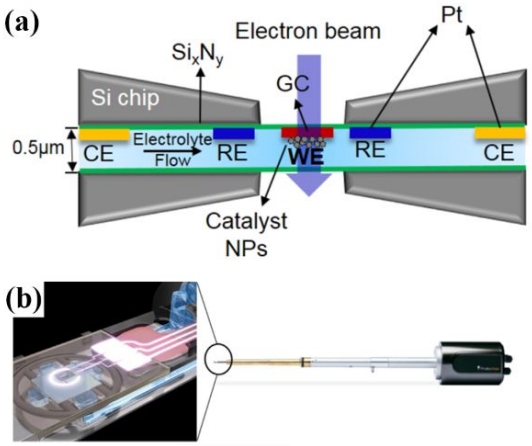

Fig. 20 Schematic illustration of (a) the electrochemical cell for in situ TEM and (b) the liquid electrochemical Poseidon TEM holder. WE, CE, RE represent working electrode, counter electrode, and reference electrode, respectively. Reproduced with permission from ref. 221. Copyright 2020, American Chemical Society.

Operando and in situ characterizations are indispensable in the advancement of our understanding of dynamic electrocatalyst reconstruction and catalytic mechanisms, including the identification of actual active species and active sites, by rendering the real-time and in-place examination of local morphologies, compositions, and oxidation states possible. However, the complex setups and cell configurations required for different measurements still serve as barriers to the actualization of comprehensive observation of the dynamic process in electrocatalytic water splitting. Therefore, the continued development and utilization of operando and in situ characterization techniques is key to unlocking a more complete understanding of electrocatalyst surface reconstruction during OER.

5.2 Density functional theory calculations

As well known, advances in DFT calculations have significantly contributed to precisely determine the binding energies of the electrocatalysts, which have been used as an active descriptor to elucidate reaction mechanisms, screen potential candidates, and optimize electrocatalysts. For example, Sargent and co-workers performed theoretical simulation of different Ni structures including $Ni(OH)_2$, β-NiOOH and NiO_2 doped with Co, Fe and P, respectively, based on Hubbard-like corrections (DFT + U), to model different oxidation states

including Ni^{2+}, Ni^{3+} and Ni^{4+}, respectively.[16] Interestingly, the calculation results suggested that the Gibbs formation energy of NiO_2, which is intrinsically unstable, can be reduced when doped with Co, Fe and P. To better understand this phenomenon, the following two PCET processes (eqn (12) ~ (13)) are considered; and the proposed transformation from Ni^{2+} to Ni^{4+} was illustrated (**Fig. 21a**).

$$Ni(OH)_2 \rightarrow NiOOH + H^+ + e^- \quad (12)$$

$$NiOOH \rightarrow NiO_2 + H^+ + e^- \quad (13)$$

It was found that doping with P destabilized the $Ni(OH)_2$ phase, thus promoting $Ni^{2+} \rightarrow Ni^{3+}$ oxidation (**Fig. 21b**). In addition, the Ni^{4+} phase could be stabilized via substituting Ni with Co and Fe, accelerating the oxidation from Ni^{3+} into Ni^{4+} (**Fig. 21b**).

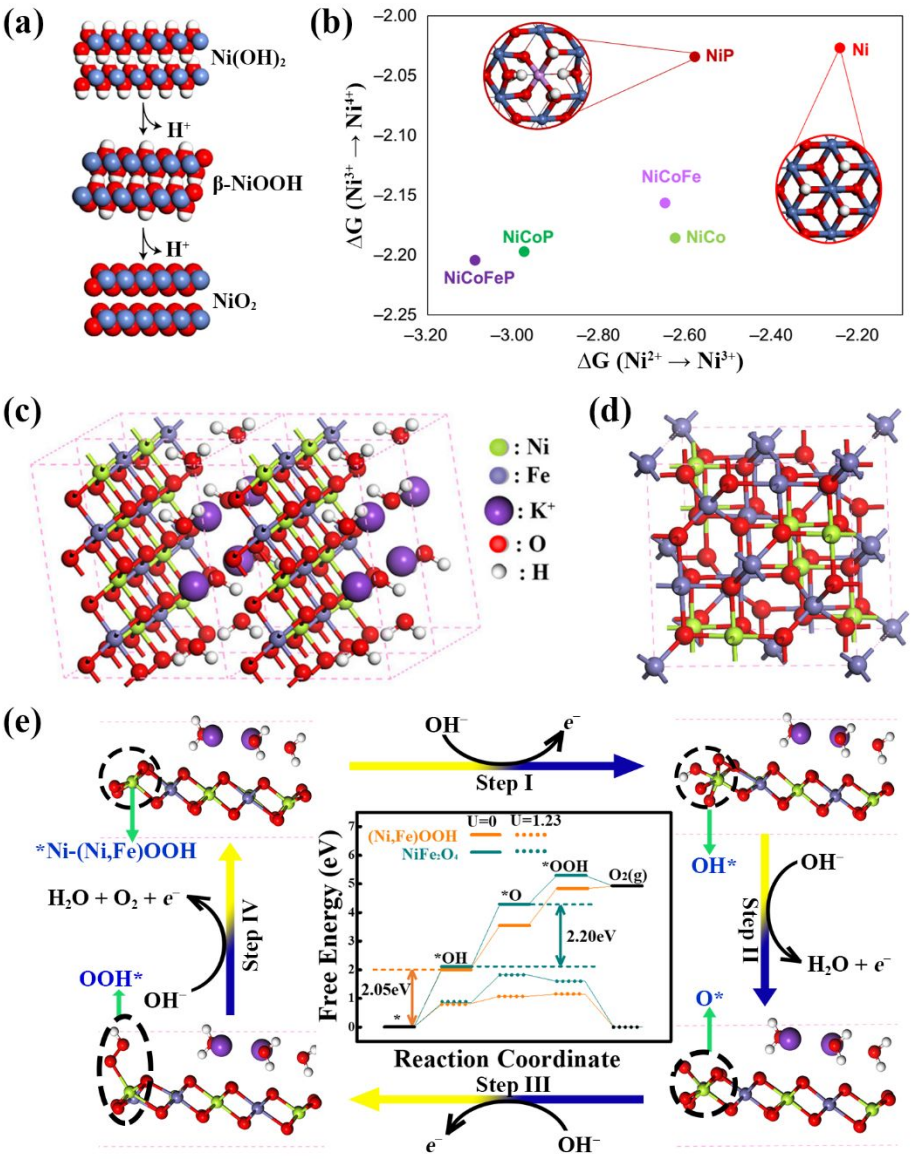

Fig. 21 (a) Schematic of the two-step oxidation process from $Ni(OH)_2$ into NiO_2. (b) Gibbs free energies of the oxidation from $Ni(OH)_2$ into NiO_2 on various Ni structures with different substitutions. Reproduced with permission from ref. 16. Copyright 2018, Springer Nature. (c) Schematic for the model crystal structure of (Ni,Fe)OOH. (d) The model crystal structure for inverse spinel $NiFe_2O_4$. (e) Schematic of the proposed 4*e*-OER steps on (Ni,Fe)OOH. Inset, schematic illustration of DFT-based Gibbs free energy calculations on (Ni,Fe)OOH and $NiFe_2O_4$ at applied potentials (U = 0 and 1.23). Reproduced with permission from ref. 24. Copyright 2021, National Academy of Sciences.

In consideration of the dynamic reconstruction of electrocatalysts during the OER, it is noteworthy that, as a general rule, the resultant oxyhydroxides should be the actual active species; thus, an exact model structure is required to make a suitably accurate prediction of the kinetics, among which the structure is determined by the aforementioned operando/in situ analyses. Lin et al. compared theoretical OER activities of the reconstructed species (i.e., (Ni,Fe)OOH) and the pristine catalyst (i.e., $NiFe_2O_4$) according to DFT-based Gibbs free energy calculations to achieve a thorough acknowledge of the relationship between the reconstructed species and OER activity.[24] As aforementioned (**Section 4.6**), $NiFe_2O_4$ nanoparticles (NFO NPs) were dynamically reconstructed into (Ni,Fe)OOH species during the OER; therefore, in order to accurately represent this system, the model of (Ni,Fe)OOH was constructed from two-dimensional $(Ni,Fe)O_2$ layers, intercalated with H_2O molecules and K^+ ions, as shown in **Fig. 21c**. Meanwhile, the model of the original spinel NFO, in accordance with the inverse spinel structure (i.e., $Fe(Ni,Fe)O_4$), the tetrahedral space was occupied by half of Fe^{3+} ions, while the octahedral space was filled by the remaining Fe^{3+} ions and Ni^{2+} ions (**Fig. 21d**). Comparing the DFT calculation results for each model structure (**Fig. 21e**), it was determined that (Ni,Fe)OOH exhibited a lower Gibbs free energy than the initial surface structure, verifying that the reconstructed surface acted more active for OER. By confirming that the reconstructed (Ni,Fe)OOH is the true active site during oxygen evolution, this study highlighted the importance of the dynamic reconstruction process for improving the OER activity.

In addition to Gibbs free energy diagrams, density of states (DOS) and band structures are

often calculated to demonstrate the electronic structure of electrocatalysts. More importantly, the location of the O 2*p*-band level with respect to the Fermi level can indicate the likelihood for a dynamic change of the pristine catalyst into reconstructed oxyhydroxides in an oxidizing, alkaline electrochemical process. For example, Xu et al. found that spinel $CoAl_2O_4$ substituted by Fe can upshift the O 2*p*-band level and move it closer to the Fermi level as given by their band center energies in the projected density of state (PDOS) (**Fig. 22a**).[188] The location of the O 2*p*-band level versus the Fermi level reflected a positive correlation with the OER performance. That is, the Fermi level shifted towards the O 2*p* center would create the oxygen-state holes during the OER, which is due to the consistency of the O_2/H_2O redox potential and the O 2*p* state energy in the catalyst, thus promoting the lattice oxygen oxidation.[48] In addition, it has been well revealed that the high O 2*p* center demonstrated the decreased generation energy of oxygen vacancy, which was representative for the facilitated formation of oxygen vacancy.[223, 224] As discussed earlier, the introduction of oxygen vacancies in pristine electrocatalysts could facilitate the surface reconstruction process.[66, 198] However, in this study, when at the highest ratio of Fe substitution (i.e., $CoFe_2O_4$), it was found to possess the maximum of oxygen vacancies inside the catalysts in comparison to $CoAl_2O_4$ and $CoFe_{0.25}Al_{1.75}O_4$, yet showed the unapparent reconstruction behavior during the OER and the lowest O 2*p* level (**Fig. 22b**). In contrast, the O 2*p* level in the $CoFe_{0.25}Al_{1.75}O_4$ was highest, which was more favorable for the oxidation of lattice oxygen and generation of surface oxygen vacancies. Given that the spinel structure possesses the same octahedral parts as the perovskites (**Section 3.1.2**), the surface reconstruction should be also initiated with lattice oxygen evolution reaction (LOER), resulting in the leaching of Al cations and the reconstruction of Co cations into oxyhydroxides. This was also supported by the experimental results from in situ XANES (**Section 4.2**) and ICP-MS, which confirmed a mass of Al cations leaching into the electrolyte and the oxidation of Co cations without leaching. Taking all of the above analyses into consideration, the critical role for triggering surface reconstruction in the case of Fe-substituted $CoAl_2O_4$ OER system should be the surface oxygen vacancy produced in the LOER process. Thus, it is proposed that as more oxygen vacancies continually accumulated on the electrocatalyst surface via the LOER, the surface was increasingly driven to more completely reconstruct into oxyhydroxides (**Fig. 22c**). In the other words, such surface reconstruction in

the OER process can be theoretically illustrated by the integrated DOS and O 2*p* level.

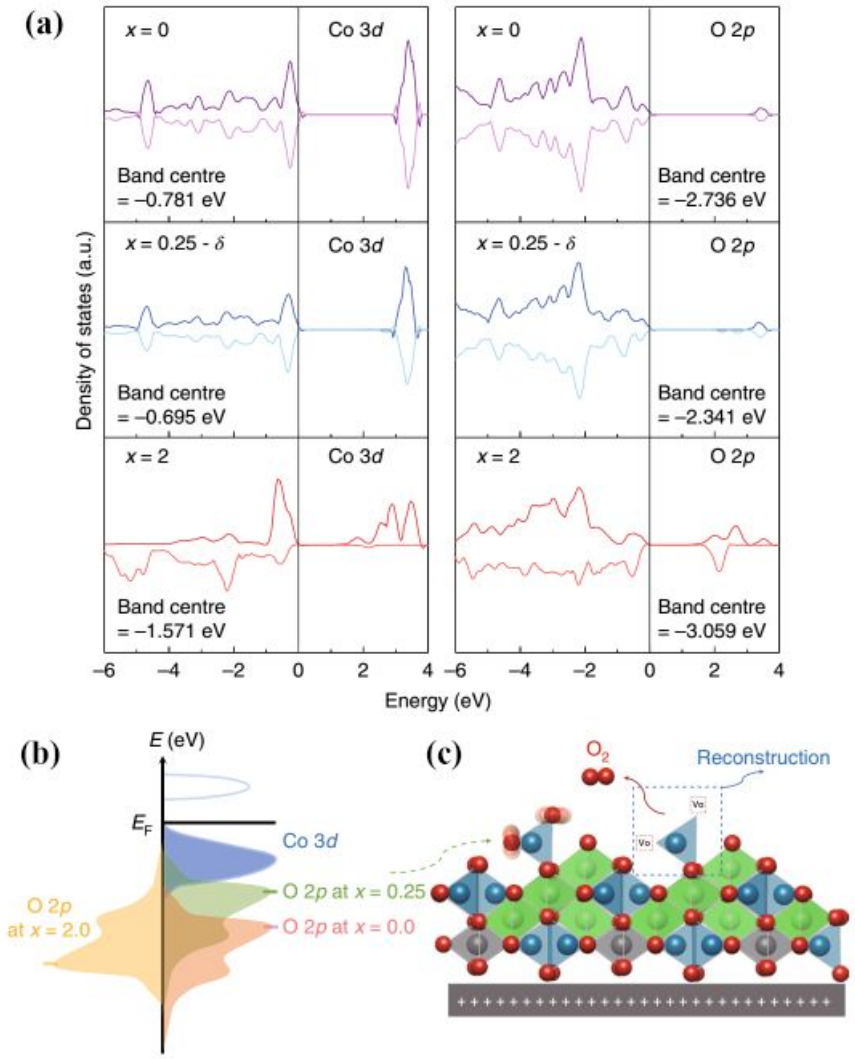

Fig. 22 (a) Projected density of state (PDOS) of Co 3*d*, O 2*p* in $CoFe_xAl_{2-x}O_4$ ($x = 0$, 0.25 and 2.0). (b) Schematic illustration for the band of $CoFe_xAl_{2-x}O_4$ ($x = 0$, 0.25 and 2.0). (c) Schematic illustration for the surface reconstruction mechanism using $CoFe_{0.25}Al_{1.75}O_4$ as catalyst. Reproduced with permission from ref. 188. Copyright 2019, Springer Nature.

6. Conclusions and future perspectives

In recent years, great efforts have been devoted to understanding the dynamic reconstruction process of transition-metal-based electrocatalysts for the oxygen evolution reaction (OER), with many studies utilizing the advances in operando/in situ experimental techniques and theoretical calculations. In this review, we have summarized the dynamic

behavior of transition-metal-based catalysts during the electrochemical oxygen evolution process, discussed some emerging strategies employed to activate and tailor the surface reconstruction for triggering high-efficient OER, and briefly provided an overview of in situ/operando characterization techniques and DFT calculations which are commonly employed to study the surface reconstruction. Detailed mechanism-centered studies aided by operando/in situ measurements and computational simulations are prerequisite to build a fundamental understanding of electrocatalytic activity and the material properties that influence it. Upon reaching this base-understanding, we will be able to overcome the most pressing challenges faced in the development of more efficient water splitting. As discussed above, some advancements have been made in this regard; yet there are considerable challenges which remain based on the following aspects:

(1) Systematic studies are imperative to evaluate and compare the influences of reconstruction level/depth on the catalytic activity. In general, electrocatalytic reactions are a kind of heterogeneous catalytic reaction that occur on the electrocatalyst surface. Therefore, the catalytic performance is largely dependent on the properties of the catalyst surface. Moreover, it should be noted that electrocatalysts that undergo only partial reconstruction, it can be considered a special kind of in-situ-generated composite catalyst which may exhibit a distinct interfacial effect that greatly influences the adsorption/desorption of reaction intermediates along with the transportation of electrons and ions. The interfacial effect in reconstructed catalysts, such as oxide/oxyhydroxide-core/shell catalysts, may bring about novel strategies to improve electrocatalytic activity and stability. For this reason, future research efforts should be dedicated to vigorously exploring the structure-activity relationship, with particular focus on the reconstruction depth and synergistic core-shell interactions, to yield the largest possible performance enhancement.

(2) Precise computational simulations are required to investigate the real-world electrocatalytic reactions. Although a series of electrocatalysis studies based on integrated operando/in situ techniques and DFT calculations have found great success, some limitations remain. DFT calculations can provide insight into the catalytic mechanism and identify active sites through modeling the electrocatalysts and working conditions; however, these calculation results can vary significantly due to different choices of model structures (the exposed face and

layers) and simulation parameters (exchange correlation functions and U values). Therefore, the actual structure of the catalysts should be precisely confirmed via operando/in situ techniques to limit this variability. In particular, special attention should be paid to partially reconstructed catalysts, which comprise heterogeneous structures consisting of the reconstructed species and initial catalyst material. Additionally, the operando/in situ analysis techniques should be continuously developed. Current in situ electrochemical cell configurations and the corresponding experimental equipment cannot provide enough accuracy to confidently capturing the real-world dynamic reconstruction of electrocatalysts. For instance, the limited detection depth of operando Raman fails to convey the practical reconstruction depth, which would further interfere with the accuracy of any derived DFT calculations.

(3) The active sites, defects, and compositions of electrocatalysts should be further identified and optimized. This holds especially true for bi-metal- or multi-metal-based catalysts, which may have more than one kind of metal taking part in the reconstruction process to form the active species. The function of each metal and the synergistic effect between the different components continues to be highly controversial. It remains a tremendous challenge to further modulate the electronic structure via precise tailoring of the reconstructed species, component distributions, and defect content under OER conditions. As discussed above, in the case of multi-metal-based electrocatalysts, one study considered the leaching of one metal's ions could promote the reconstruction of the other metal cations.[133] Likewise, it is critical to investigate and summarize the group of metals that are more prone to leach out while also facilitating the dynamic reconstruction during the OER process. In addition, special attention should be directed towards the clarification of active sites in reconstructed bi-metal/multi-metal-based catalysts; this information could accelerate the optimization of electrocatalysts and aid in the regulation of dynamic reconstruction processes in future work.

(4) Substantial room for adjusting the dynamic reconstruction process remains in the exploration of more available and effective strategies. Although some novel strategies have been demonstrated to achieve deeper-level dynamic changes in catalysts, the OER activity and stability of many non-precious electrocatalysts are still inferior to that of the traditional RuO_2 and IrO_2 benchmark OER catalysts in alkaline electrolyte. Outside of the rational design of electrocatalysts incorporating various combinations of nanocomposite materials and the

methodical property comparison of each, the assistance of external energy could be employed to drive the endothermic reactions and lower the kinetics barriers. For example, a moderate magnetic field (350 mT) has been recently applied to the cathodes, which promoted the electron transfer in Co catalyst; as a result, high spin polarization and improved adsorption of oxygen intermediates was achieved, which ultimately yielded a significant boost in OER and ORR activity.[225] Moreover, most studies on photothermal-promoted OER were conducted through the combination of catalysts and photothermal agents (carbon materials or plasmonic materials).[213] For practical applications, "bifunctional" materials that can serve as both the catalyst and photothermal/magnetic agent should be developed; and the formation mechanisms of these photothermal/magnetic-promoted active species should be comprehensively investigated for further develop robust and low-cost OER systems.

(5) The dynamic reconstructions that occur during other electrochemical reactions, such as oxygen reduction reaction (ORR), CO_2 reduction (CO_2RR), hydrogen evolution reaction (HER), N_2 reduction reaction (NRR), and methanol oxidation reaction (MOR), should be further explored. As already summarized in several other works, significant achievements have already been made in the investigation of electrochemical reduction and oxidation reactions.[9, 222, 226-229] Future work can focus on fundamental mechanism studies, utilizing the modern characterization techniques and computational simulations covered in this review, since the mechanisms of dynamic reconstruction in these reduction reactions are completely different from the OER. For example, the high-valence In of a InN catalyst reconstructed into metallic In^0 during the CO_2 electroreduction, leading to an enhanced carrier density on the reconstructed surface that further promoted the formation of the HCOO□ intermediate key to triggering formate generation.[230] More recently, Mn oxide (MnO) has been explored as an ORR electrocatalyst and was found to experience the in situ generation of both the high-valence species (Mn^{3+} and Mn^{4+}) and oxygen vacancies under operando conditions; both of these reconstructed species would favor the adsorption and reduction of O_2, thus boosting the ORR activity.[231] Nevertheless, scientific research aimed at systematically and fundamentally understanding the dynamic changes which occur in each pertinent electrochemical reaction (i.e., OER, ORR, HER, CO_2RR, etc.) has been, up until now, obviously inadequate.

All in all, new opportunities for the exploration of dynamic catalyst reconstruction

behaviors in electrocatalytic reactions are still abundant. The standardized evaluation system for tracking the reconstruction process, clarifying the actual active species, unveiling the catalytic mechanism, and rationally designing the electrocatalysts, should be further enriched. We anticipate that this review will push forward the field of electrocatalysis and serve as a comprehensive source of information to help overcome the significant challenges in developing more efficient water splitting.

Acknowledgments

This work is supported by the Air Force Office of Scientific Research (FA9550-19-1-0317). L. G. gratefully acknowledges the financial support from the China Scholarship Council.

References

1. X. Cui, L. Gao, S. Lei, S. Liang, J. Zhang, C. D. Sewell, W. Xue, Q. Liu, Z. Lin and Y. Yang, *Adv. Funct. Mater.*, 2021, **31**, 2009197.
2. Y. Jiao, Y. Zheng, M. Jaroniec and S. Z. Qiao, *Chem. Soc. Rev.*, 2015, **44**, 2060-2086.
3. Z. W. Seh, J. Kibsgaard, C. F. Dickens, I. Chorkendorff, J. K. Nørskov and T. F. Jaramillo, *Science*, 2017, **355**, eaad4998.
4. Q. Shi, C. Zhu, D. Du and Y. Lin, *Chem. Soc. Rev.*, 2019, **48**, 3181-3192.
5. S. Zhao, C. Tan, C.-T. He, P. An, F. Xie, S. Jiang, Y. Zhu, K.-H. Wu, B. Zhang and H. Li, *Nat. Energy*, 2020, **5**, 881-890.
6. B. Zhang, L. Wang, Z. Cao, S. M. Kozlov, F. P. G. de Arquer, C. T. Dinh, J. Li, Z. Wang, X. Zheng and L. Zhang, *Nat. Catal.*, 2020, **3**, 985-992.
7. F. Dionigi and P. Strasser, *Adv. Energy Mater.*, 2016, **6**, 1600621.
8. Z. Zeng, M. K. Chan, Z.-J. Zhao, J. Kubal, D. Fan and J. Greeley, *J. Phys. Chem. C*, 2015, **119**, 18177-18187.
9. H. Jiang, Q. He, Y. Zhang and L. Song, *Accounts. Chem. Res.*, 2018, **51**, 2968-2977.
10. S. Anantharaj, S. R. Ede, K. Sakthikumar, K. Karthick, S. Mishra and S. Kundu, *ACS Catal.*, 2016, **6**, 8069-8097.
11. O. Mabayoje, A. Shoola, B. R. Wygant and C. B. Mullins, *ACS Energy Lett.*, 2016, **1**, 195-201.
12. B. R. Wygant, K. Kawashima and C. B. Mullins, *ACS Energy Lett.*, 2018, **3**, 2956-2966.
13. Z. Zou, T. Wang, X. Zhao, W.-J. Jiang, H. Pan, D. Gao and C. Xu, *ACS Catal.*, 2019, **9**, 7356-7364.
14. X. Wang, L. Chai, J. Ding, L. Zhong, Y. Du, T.-T. Li, Y. Hu, J. Qian and S. Huang, *Nano Energy*, 2019, **62**, 745-753.
15. F. Lin, Y. Liu, X. Yu, L. Cheng, A. Singer, O. G. Shpyrko, H. L. Xin, N. Tamura, C. Tian and T.-C. Weng, *Chem. Rev.*, 2017, **117**, 13123-13186.
16. X. Zheng, B. Zhang, P. De Luna, Y. Liang, R. Comin, O. Voznyy, L. Han, F. P. G. De Arquer, M. Liu and C. T. Dinh, *Nat. Chem.*, 2018, **10**, 149-154.

17. H. Kim, J. Park, I. Park, K. Jin, S. E. Jerng, S. H. Kim, K. T. Nam and K. Kang, *Nat. Commun.*, 2015, **6**, 1-11.
18. W. Chen, H. Wang, Y. Li, Y. Liu, J. Sun, S. Lee, J.-S. Lee and Y. Cui, *ACS Central Sci.*, 2015, **1**, 244-251.
19. H. Liang, A. N. Gandi, C. Xia, M. N. Hedhili, D. H. Anjum, U. Schwingenschlögl and H. N. Alshareef, *ACS Energy Lett.*, 2017, **2**, 1035-1042.
20. K. Fan, H. Zou, Y. Lu, H. Chen, F. Li, J. Liu, L. Sun, L. Tong, M. F. Toney and M. Sui, *ACS Nano*, 2018, **12**, 12369-12379.
21. X. Xu, F. Song and X. Hu, *Nature Commun.*, 2016, **7**, 1-7.
22. X. Liu, K. Ni, B. Wen, R. Guo, C. Niu, J. Meng, Q. Li, P. Wu, Y. Zhu and X. Wu, *ACS Energy Lett.*, 2019, **4**, 2585-2592.
23. X. Liu, R. Guo, K. Ni, F. Xia, C. Niu, B. Wen, J. Meng, P. Wu, J. Wu and X. Wu, *Adv. Mater.*, 2020, **32**, 2001136.
24. L. Gao, X. Cui, Z. Wang, C. D. Sewell, Z. Li, S. Liang, M. Zhang, J. Li, Y. Hu and Z. Lin, *P. Natl. Acad. Sci. USA,* 2021, **118**, e2023421118.
25. B. You and Y. Sun, *Accounts. Chem. Res.*, 2018, **51**, 1571-1580.
26. M.-R. Gao, Y.-R. Zheng, J. Jiang and S.-H. Yu, *Accounts. Chem. Res.*, 2017, **50**, 2194-2204.
27. J. Wang, Y. Gao, H. Kong, J. Kim, S. Choi, F. Ciucci, Y. Hao, S. Yang, Z. Shao and J. Lim, *Chem. Soc. Rev.*, 2020, **49**, 9154-9196.
28. P. F. Liu, H. Yin, H. Q. Fu, M. Y. Zu, H. G. Yang and H. Zhao, *J. Mater. Chem. A*, 2020, **8**, 10096-10129.
29. X. Cui, S. Lei, A. C. Wang, L. Gao, Q. Zhang, Y. Yang and Z. Lin, *Nano Energy*, 2020, **70**, 104525.
30. N.-T. Suen, S.-F. Hung, Q. Quan, N. Zhang, Y.-J. Xu and H. M. Chen, *Chem. Soc. Rev.*, 2017, **46**, 337-365.
31. C. Hu, L. Zhang and J. Gong, *Energ. Environ. Sci.*, 2019, **12**, 2620-2645.
32. F. Song, L. Bai, A. Moysiadou, S. Lee, C. Hu, L. Liardet and X. Hu, *J. Am. Chem. Soc.*, 2018, **140**, 7748-7759.
33. J. H. Montoya, L. C. Seitz, P. Chakthranont, A. Vojvodic, T. F. Jaramillo and J. K. Nørskov, *Nat. Mater.*, 2017, **16**, 70-81.
34. J. Song, C. Wei, Z.-F. Huang, C. Liu, L. Zeng, X. Wang and Z. J. Xu, *Chem. Soc. Rev.*, 2020, **49**, 2196-2214.
35. W. T. Hong, M. Risch, K. A. Stoerzinger, A. Grimaud, J. Suntivich and Y. Shao-Horn, *Energ. Environ. Sci.*, 2015, **8**, 1404-1427.
36. A. Grimaud, W. T. Hong, Y. Shao-Horn and J.-M. Tarascon, *Nat. Mater.*, 2016, **15**, 121-126.
37. A. J. Medford, A. Vojvodic, J. S. Hummelshøj, J. Voss, F. Abild-Pedersen, F. Studt, T. Bligaard, A. Nilsson and J. K. Nørskov, *J. Catal.*, 2015, **328**, 36-42.
38. I. C. Man, H. Y. Su, F. Calle-Vallejo, H. A. Hansen, J. I. Martinez, N. G. Inoglu, J. Kitchin, T. F. Jaramillo, J. K. Nørskov and J. Rossmeisl, *ChemCatChem*, 2011, **3**, 1159-1165.
39. A. Kulkarni, S. Siahrostami, A. Patel and J. K. Nørskov, *Chem. Rev.*, 2018, **118**, 2302-2312.
40. M. T. Koper, *Chem. Sci.*, 2013, **4**, 2710-2723.
41. S. H. Ye, Z. X. Shi, J. X. Feng, Y. X. Tong and G. R. Li, *Angew. Chem. Int. Edit.*, 2018, **57**, 2672-2676.
42. Y. Yang, X. Cui, D. Gao, H. He, Y. Ou, M. Zhou, Q. Lai, X. Wei, P. Xiao and Y. Zhang, *Sustain. Energ. Fuels*, 2020, **4**, 3647-3653..

43. J. Liu, Y. Ji, J. Nai, X. Niu, Y. Luo, L. Guo and S. Yang, *Energ. Environ. Sci.*, 2018, **11**, 1736-1741.
44. J. Suntivich, K. J. May, H. A. Gasteiger, J. B. Goodenough and Y. Shao-Horn, *Science*, 2011, **334**, 1383-1385.
45. D. A. Kuznetsov, B. Han, Y. Yu, R. R. Rao, J. Hwang, Y. Román-Leshkov and Y. Shao-Horn, *Joule*, 2018, **2**, 225-244.
46. B. Han, A. Grimaud, L. Giordano, W. T. Hong, O. Diaz-Morales, L. Yueh-Lin, J. Hwang, N. Charles, K. A. Stoerzinger and W. Yang, *J. Phys. Chem. C*, 2018, **122**, 8445-8454.
47. Z.-F. Huang, J. Song, Y. Du, S. Xi, S. Dou, J. M. V. Nsanzimana, C. Wang, Z. J. Xu and X. Wang, *Nat. Energy*, 2019, **4**, 329-338.
48. A. Grimaud, O. Diaz-Morales, B. Han, W. T. Hong, Y.-L. Lee, L. Giordano, K. A. Stoerzinger, M. T. Koper and Y. Shao-Horn, *Nat. Chem.*, 2017, **9**, 457-465.
49. X. Rong, J. Parolin and A. M. Kolpak, *ACS Catal.*, 2016, **6**, 1153-1158.
50. J. S. Yoo, X. Rong, Y. Liu and A. M. Kolpak, *ACS Catal.*, 2018, **8**, 4628-4636.
51. J. Hwang, R. R. Rao, L. Giordano, Y. Katayama, Y. Yu and Y. Shao-Horn, *Science*, 2017, **358**, 751-756.
52. S. Jin, *ACS Energy Lett.,* 2017, **2**, 1937-1938.
53. Y. Yang, M. Luo, W. Zhang, Y. Sun, X. Chen and S. Guo, *Chem*, 2018, **4**, 2054-2083.
54. X. Cui, W. Guo, M. Zhou, Y. Yang, Y. Li, P. Xiao, Y. Zhang and X. Zhang, *ACS Appl. Mater. Inter.*, 2015, **7**, 493-503.
55. X. Cui, P. Xiao, J. Wang, M. Zhou, W. Guo, Y. Yang, Y. He, Z. Wang, Y. Yang and Y. Zhang, *Angew. Chem. Int. Edit.*, 2017, **129**, 4559-4564.
56. X. Cui, Y. Yang, Y. Li, F. Liu, H. Peng, Y. Zhang and P. Xiao, *J. Electrochem. Soc.*, 2015, **162**, F1415.
57. Y. Yang, M. Zhou, W. Guo, X. Cui, Y. Li, F. Liu, P. Xiao and Y. Zhang, *Electrochim. Acta*, 2015, **174**, 246-253.
58. X. Zhao, Y. Yang, Y. Li, X. Cui, Y. Zhang and P. Xiao, *J. Mater. Sci.*, 2016, **51**, 3724-3734.
59. C. Xia, Q. Jiang, C. Zhao, M. N. Hedhili and H. N. Alshareef, *Adv. Mater.*, 2016, **28**, 77-85.
60. S. Li, S. Peng, L. Huang, X. Cui, A. M. Al-Enizi and G. Zheng, *ACS Appl. Mater. Inter.*, 2016, **8**, 20534-20539.
61. V. Stevanović, S. Lany, X. Zhang and A. Zunger, *Phys. Rev. B*, 2012, **85**, 115104.
62. F. A. Rasmussen and K. S. Thygesen, *J. Phys. Chem. C*, 2015, **119**, 13169-13183.
63. B. M. Hunter, H. B. Gray and A. M. Muller, *Chem. Rev.*, 2016, **116**, 14120-14136.
64. M. Görlin, J. Ferreira de Araújo, H. Schmies, D. Bernsmeier, S. r. Dresp, M. Gliech, Z. Jusys, P. Chernev, R. Kraehnert and H. Dau, *J. Am. Chem. Soc.*, 2017, **139**, 2070-2082.
65. Q. He, Y. Wan, H. Jiang, Z. Pan, C. Wu, M. Wang, X. Wu, B. Ye, P. M. Ajayan and L. Song, *ACS Energy Lett.*, 2018, **3**, 1373-1380.
66. E. Fabbri, M. Nachtegaal, T. Binninger, X. Cheng, B.-J. Kim, J. Durst, F. Bozza, T. Graule, R. Schäublin and L. Wiles, *Nat. Mater.*, 2017, **16**, 925-931.
67. N. Ullah, W. Zhao, X. Lu, C. J. Oluigbo, S. A. Shah, M. Zhang, J. Xie and Y. Xu, *Electrochim. Acta*, 2019, **298**, 163-171.
68. M. Steimecke, G. Seiffarth, C. Schneemann, F. Oehler, S. Förster and M. Bron, *ACS Catal.*, 2020, **10**, 3595-3603.
69. M. K. Bates, Q. Jia, H. Doan, W. Liang and S. Mukerjee, *ACS Catal.*, 2016, **6**, 155-161.
70. D. M. Morales, M. A. Kazakova, S. Dieckhöfer, A. G. Selyutin, G. V. Golubtsov, W. Schuhmann

and J. Masa, *Adv. Funct. Mater.*, 2020, **30**, 1905992.
71. Z. J. Xu, *Science China Materials*, 2020, **63**, 3-7.
72. Y. Li, X. Du, J. Huang, C. Wu, Y. Sun, G. Zou, C. Yang and J. Xiong, *Small*, 2019, **15**, 1901980.
73. K. J. Lee, B. D. McCarthy and J. L. Dempsey, *Chem. Soc. Rev.*, 2019, **48**, 2927-2945.
74. A. Sivanantham, P. Ganesan, A. Vinu and S. Shanmugam, *ACS Catal.*, 2019, **10**, 463-493.
75. M. Morita, C. Iwakura and H. Tamura, *Electrochim. Acta*, 1977, **22**, 325-328.
76. J. G. Metz, P. J. Nixon, M. Rogner, G. W. Brudvig and B. A. Diner, *Biochemistry*, 1989, **28**, 6960-6969.
77. M. M. Najafpour and D. J. Sedigh, *Dalton T.*, 2013, **42**, 12173-12178.
78. Q. Zhao, Z. Yan, C. Chen and J. Chen, *Chem. Rev.*, 2017, **117**, 10121-10211.
79. L. Han, S. Dong and E. Wang, *Adv. Mater.*, 2016, **28**, 9266-9291.
80. E. Hryha and L. Nyborg, *Metall. Mater. Trans. A*, 2014, **45**, 1736-1747.
81. K. Uusi-Esko, E.-L. Rautama, M. Laitinen, T. Sajavaara and M. Karppinen, *Chem. Mater.*, 2010, **22**, 6297-6300.
82. D. Chen, C. Chen, Z. M. Baiyee, Z. Shao and F. Ciucci, *Chem. Rev.*, 2015, **115**, 9869-9921.
83. N. Zhang, F. Cheng, Y. Liu, Q. Zhao, K. Lei, C. Chen, X. Liu and J. Chen, *J. Am. Chem. Soc.*, 2016, **138**, 12894-12901.
84. F. Cheng, T. Zhang, Y. Zhang, J. Du, X. Han and J. Chen, *Angew. Chem. Int. Edit.*, 2013, **125**, 2534-2537.
85. J. Bao, X. Zhang, B. Fan, J. Zhang, M. Zhou, W. Yang, X. Hu, H. Wang, B. Pan and Y. Xie, *Angew. Chem. Int. Edit.*, 2015, **127**, 7507-7512.
86. H. Yang, Y. Liu, S. Luo, Z. Zhao, X. Wang, Y. Luo, Z. Wang, J. Jin and J. Ma, *ACS Catal.*, 2017, **7**, 5557-5567.
87. C. Wei, Z. Feng, G. G. Scherer, J. Barber, Y. Shao-Horn and Z. J. Xu, *Adv. Mater.*, 2017, **29**, 1606800.
88. D. M. Robinson, Y. B. Go, M. Greenblatt and G. C. Dismukes, *J. Am. Chem. Soc.*, 2010, **132**, 11467-11469.
89. T. Maiyalagan, K. A. Jarvis, S. Therese, P. J. Ferreira and A. Manthiram, *Nat. Commun.*, 2014, **5**, 1-8.
90. A. Bergmann, E. Martinez-Moreno, D. Teschner, P. Chernev, M. Gliech, J. F. De Araújo, T. Reier, H. Dau and P. Strasser, *Nat. Commun.*, 2015, **6**, 8625.
91. H.-Y. Wang, S.-F. Hung, H.-Y. Chen, T.-S. Chan, H. M. Chen and B. Liu, *J. Am. Chem. Soc.*, 2016, **138**, 36-39.
92. L. Qian, L. Gu, L. Yang, H. Yuan and D. Xiao, *Nanoscale*, 2013, **5**, 7388-7396.
93. H. Wang, M. Zhou, P. Choudhury and H. Luo, *Appl. Mater. Today*, 2019, **16**, 56-71.
94. A. Kubacka, M. Fernandez-Garcia and G. Colon, *Chem. Rev.*, 2012, **112**, 1555-1614.
95. K. J. May, C. E. Carlton, K. A. Stoerzinger, M. Risch, J. Suntivich, Y.-L. Lee, A. Grimaud and Y. Shao-Horn, *J. Phys. Chem. Lett.*, 2012, **3**, 3264-3270.
96. J.-I. Jung, M. Risch, S. Park, M. G. Kim, G. Nam, H.-Y. Jeong, Y. Shao-Horn and J. Cho, *Energ. Environ. Sci.*, 2016, **9**, 176-183.
97. Y. Wang, J. Ren, Y. Wang, F. Zhang, X. Liu, Y. Guo and G. Lu, *J. Phys. Chem. C*, 2008, **112**, 15293-15298.
98. H. Wang, X. Chen, D. Huang, M. Zhou, D. Ding and H. Luo, *ChemCatChem*, 2020, **12**, 2768-2775.
99. J. Park and J. Cho, *Angew. Chem. Int. Edit.*, 2020, **59**, 15314-15324.

100. S. Song, J. Zhou, X. Su, Y. Wang, J. Li, L. Zhang, G. Xiao, C. Guan, R. Liu and S. Chen, *Energ. Environ. Sci.*, 2018, **11**, 2945-2953.
101. X. Li, H. Wang, Z. Cui, Y. Li, S. Xin, J. Zhou, Y. Long, C. Jin and J. B. Goodenough, *Sci. Adv.*, 2019, **5**, eaav6262.
102. H. A. Tahini, X. Tan, U. Schwingenschlögl and S. C. Smith, *ACS Catal.*, 2016, **6**, 5565-5570.
103. Y. Zhu, W. Zhou, Y. Zhong, Y. Bu, X. Chen, Q. Zhong, M. Liu and Z. Shao, *Adv. Energy Mater.*, 2017, **7**, 1602122.
104. Y. Zhu, W. Zhou, Z. G. Chen, Y. Chen, C. Su, M. O. Tadé and Z. Shao, *Angew. Chem. Int. Edit.*, 2015, **127**, 3969-3973.
105. J.-P. Correa-Baena, M. Saliba, T. Buonassisi, M. Grätzel, A. Abate, W. Tress and A. Hagfeldt, *Science*, 2017, **358**, 739-744.
106. B. Zhao, L. Zhang, D. Zhen, S. Yoo, Y. Ding, D. Chen, Y. Chen, Q. Zhang, B. Doyle and X. Xiong, *Nat. Commun.*, 2017, **8**, 1-9.
107. F. Lu, M. Zhou, Y. Zhou and X. Zeng, *Small*, 2017, **13**, 1701931.
108. H.-s. Nan, X.-y. Hu and H.-w. Tian, *Mat. Sci. Semicon. Proc.*, 2019, **94**, 35-50.
109. S. Geiger, O. Kasian, M. Ledendecker, E. Pizzutilo, A. M. Mingers, W. T. Fu, O. Diaz-Morales, Z. Li, T. Oellers and L. Fruchter, *Nat. Catal.*, 2018, **1**, 508-515.
110. Y. Chen, H. Li, J. Wang, Y. Du, S. Xi, Y. Sun, M. Sherburne, J. W. Ager, A. C. Fisher and Z. J. Xu, *Nat. Commun.*, 2019, **10**, 1-10.
111. J. S. Kim, B. Kim, H. Kim and K. Kang, *Adv. Energy Mater.*, 2018, **8**, 1702774.
112. G. C. Mather, C. Dussarrat, J. Etourneau and A. R. West, *J. Mater. Chem.*, 2000, **10**, 2219-2230.
113. K. Fominykh, J. M. Feckl, J. Sicklinger, M. Döblinger, S. Böcklein, J. Ziegler, L. Peter, J. Rathousky, E. W. Scheidt and T. Bein, *Adv. Funct. Mater.*, 2014, **24**, 3123-3129.
114. J. Xiao and S. Yang, *J. Mater. Chem.*, 2012, **22**, 12253-12262.
115. X. Xu, B. Dong, S. Ding, C. Xiao and D. Yu, *J. Mater. Chem. A*, 2014, **2**, 13069-13074.
116. H. Xu, Z. X. Shi, Y. X. Tong and G. R. Li, *Adv. Mater.*, 2018, **30**, 1705442.
117. L. Trotochaud, J. K. Ranney, K. N. Williams and S. W. Boettcher, *J. Am. Chem. Soc.*, 2012, **134**, 17253-17261.
118. H. G. Sanchez Casalongue, M. L. Ng, S. Kaya, D. Friebel, H. Ogasawara and A. Nilsson, *Angew. Chem. Int. Edit.*, 2014, **126**, 7297-7300.
119. Z. Pavlovic, C. Ranjan, M. van Gastel and R. Schlögl, *Chem. Commun.*, 2017, **53**, 12414-12417.
120. J. Rossmeisl, Z.-W. Qu, H. Zhu, G.-J. Kroes and J. K. Nørskov, *J. Electroanal. Chem.*, 2007, **607**, 83-89.
121. R. P. Forslund, W. G. Hardin, X. Rong, A. M. Abakumov, D. Filimonov, C. T. Alexander, J. T. Mefford, H. Iyer, A. M. Kolpak and K. P. Johnston, *Nat. Commun.*, 2018, **9**, 1-11.
122. X. Liang, L. Shi, R. Cao, G. Wan, W. Yan, H. Chen, Y. Liu and X. Zou, *Adv. Mater.*, 2020, **32**, 2001430.
123. C. Kuai, Y. Zhang, L. Han, H. L. Xin, C.-J. Sun, D. Nordlund, S. Qiao, X.-W. Du and F. Lin, *J. Mater. Chem. A*, 2020, **8**, 10747-10754.
124. X. Zou and Y. Zhang, *Chem. Soc. Rev.*, 2015, **44**, 5148-5180.
125. L.-A. Stern, L. Feng, F. Song and X. Hu, *Energ. Environ. Sci.*, 2015, **8**, 2347-2351.
126. R. R. Eady, *Chem. Rev.*, 1996, **96**, 3013-3030.
127. B. K. Burgess and D. J. Lowe, *Chem. Rev.*, 1996, **96**, 2983-3012.
128. P. C. Hallenbeck and J. R. Benemann, *Int. J. Hydrogen Energ.*, 2002, **27**, 1185-1193.

129. S. Kaur-Ghumaan and M. Stein, *Dalton T.*, 2014, **43**, 9392-9405.
130. W. T. Eckenhoff, W. R. McNamara, P. Du and R. Eisenberg, *BBA-Bioenergetics*, 2013, **1827**, 958-973.
131. I. J. McPherson and K. A. Vincent, *J. Brazil. Chem. Soc.*, 2014, **25**, 427-441.
132. M.-R. Gao, Y.-F. Xu, J. Jiang and S.-H. Yu, *Chem. Soc. Rev.*, 2013, **42**, 2986-3017.
133. D. Liu, H. Ai, J. Li, M. Fang, M. Chen, D. Liu, X. Du, P. Zhou, F. Li and K. H. Lo, *Adv. Energy Mater.*, 2020, **10**, 2002464.
134. J. Masa, P. Weide, D. Peeters, I. Sinev, W. Xia, Z. Sun, C. Somsen, M. Muhler and W. Schuhmann, *Adv. Energy Mater.*, 2016, **6**, 1502313.
135. J.-H. Kim, K. Kawashima, B. R. Wygant, O. Mabayoje, Y. Liu, J. H. Wang and C. B. Mullins, *ACS Appl. Energ. Mater.*, 2018, **1**, 5145-5150.
136. Y. Li, Z. Dong and L. Jiao, *Adv. Energy Mater.*, 2020, **10**, 1902104.
137. Y. Shi, M. Li, Y. Yu and B. Zhang, *Energ. Environ. Sci.*, 2020, **13**, 4564-4582.
138. K. Jiang, M. Luo, M. Peng, Y. Yu, Y.-R. Lu, T.-S. Chan, P. Liu, F. M. de Groot and Y. Tan, *Nat. Commun.*, 2020, **11**, 1-9.
139. W. Zou, C. Sun, K. Zhao, J. Li, X. Pan, D. Ye, Y. Xie, W. Xu, H. Zhao and L. Zhang, *Electrochim. Acta*, 2020, **345**, 136114.
140. J. Chang, Y. Xiao, M. Xiao, J. Ge, C. Liu and W. Xing, *ACS Catal.*, 2015, **5**, 6874-6878.
141. A. Dutta, A. K. Samantara, S. K. Dutta, B. K. Jena and N. Pradhan, *ACS Energy Lett.*, 2016, **1**, 169-174.
142. P. Chen, K. Xu, Z. Fang, Y. Tong, J. Wu, X. Lu, X. Peng, H. Ding, C. Wu and Y. Xie, *Angew. Chem. Int. Edit.*, 2015, **127**, 14923-14927.
143. Y. Lyu, J. Zheng, Z. Xiao, S. Zhao, S. P. Jiang and S. Wang, *Small*, 2020, **16**, 1906867.
144. H.-Y. Wang, S.-F. Hung, Y.-Y. Hsu, L. Zhang, J. Miao, T.-S. Chan, Q. Xiong and B. Liu, *J. Phys. Chem. Lett.*, 2016, **7**, 4847-4853.
145. Y.-P. Deng, Y. Jiang, R. Liang, S.-J. Zhang, D. Luo, Y. Hu, X. Wang, J.-T. Li, A. Yu and Z. Chen, *Nat. Commun.*, 2020, **11**, 1-10.
146. S. Gupta, M. K. Patel, A. Miotello and N. Patel, *Adv. Funct. Mater.*, 2020, **30**, 1906481.
147. S. Gupta, N. Patel, A. Miotello and D. Kothari, *J. Power Sources*, 2015, **279**, 620-625.
148. C. Zhou, J. Xing, B. Xiao, J. Feng, X. Xie and Y. Chen, *Comp. Mater. Sci.*, 2009, **44**, 1056-1064.
149. B. Xiao, J. Xing, S. Ding and W. Su, *Physica B*, 2008, **403**, 1723-1730.
150. L. Burke, M. Lyons and O. Murphy, *Journal of Electroanalytical Chemistry and Interfacial Electrochemistry*, 1982, **132**, 247-261.
151. J. Zhang, X. Li, Y. Liu, Z. Zeng, X. Cheng, Y. Wang, W. Tu and M. Pan, *Nanoscale*, 2018, **10**, 11997-12002.
152. L. Bennett, J. Cuthill, A. McAlister, N. Erickson and R. Watson, *Science*, 1974, **184**, 563-565.
153. Y. Li, J. Qian, M. Zhang, S. Wang, Z. Wang, M. Li, Y. Bai, Q. An, H. Xu and F. Wu, *Adv. Mater.*, 2020, **32**, 2005802.
154. D. Liu, Q. Chang, Y. Gao, W. Huang, Z. Sun, M. Yan and C. Guo, *Electrochim. Acta*, 2020, **330**, 135243.
155. W. Zheng, L. Wang, F. Deng, S. A. Giles, A. K. Prasad, S. G. Advani, Y. Yan and D. G. Vlachos, *Nat. Commun.*, 2017, **8**, 1-8.
156. S. T. Hunt, T. Nimmanwudipong and Y. Román-Leshkov, *Angew. Chem. Int. Edit.*, 2014, **126**, 5231-5236.

157. X. Zhou, H. Dai, X. Huang, Y. Ren, Q. Wang, W. Wang, W. Huang and X. Dong, *Mater. Today Energy*, 2020, **17**, 100429.
158. F. Wu, V. Srot, S. Chen, S. Lorger, P. A. van Aken, J. Maier and Y. Yu, *Adv. Mater.*, 2019, **31**, 1905146.
159. F. Wang, S.-W. Kim, D.-H. Seo, K. Kang, L. Wang, D. Su, J. J. Vajo, J. Wang and J. Graetz, *Nat. Commun.*, 2015, **6**, 6668.
160. B. Zhang, K. Jiang, H. Wang and S. Hu, *Nano Lett.*, 2018, **19**, 530-537.
161. J. Zhang and L. Dai, *Angew. Chem. Int. Edit.*, 2016, **55**, 13296-13300.
162. Q. Dong, T. Su, W. Ge, Y. Ren, Y. Liu, W. Wang, Q. Wang and X. Dong, *Adv. Mater. Interfaces*, 2020, **7**, 1901939.
163. H. Han, K. M. Kim, H. Choi, G. Ali, K. Y. Chung, Y.-R. Hong, J. Choi, J. Kwon, S. W. Lee and J. W. Lee, *ACS Catal.*, 2018, **8**, 4091-4102.
164. A. Sivanantham, P. Ganesan and S. Shanmugam, *Adv. Funct. Mater.*, 2016, **26**, 4661-4672.
165. Y. Zuo, Y. Liu, J. Li, R. Du, X. Han, T. Zhang, J. Arbiol, N. r. J. Divins, J. Llorca and N. s. Guijarro, *Chem. Mater.*, 2019, **31**, 7732-7743.
166. B. Chakraborty, S. Kalra, R. Beltrán-Suito, C. Das, T. Hellmann, P. W. Menezes and M. Driess, *Chem.–Asian J.*, 2020, **15**, 852-859.
167. K. Yan and Y. Lu, *Small*, 2016, **12**, 2975-2981.
168. Y.-J. Tang, Y. Wang and K. Zhou, *J. Mater. Chem. A*, 2020, **8**, 7925-7934.
169. Y.-Y. Sun, Y.-X. Zhu, L.-K. Wu, G.-Y. Hou, Y.-P. Tang, H.-Z. Cao and G.-Q. Zheng, *Electrochim. Acta*, 2020, **353**, 136519.
170. B. Chakraborty, R. Beltrán-Suito, V. Hlukhyy, J. Schmidt, P. W. Menezes and M. Driess, *ChemSusChem*, 2020, **13**, 3222.
171. J. Yu, Q. Wang, D. O'Hare and L. Sun, *Chem. Soc. Rev.*, 2017, **46**, 5950-5974.
172. F. Song and X. Hu, *Nat. Commun.*, 2014, **5**, 4477.
173. G. Fan, F. Li, D. G. Evans and X. Duan, *Chem. Soc. Rev.*, 2014, **43**, 7040-7066.
174. Z. Yan, H. Sun, X. Chen, H. Liu, Y. Zhao, H. Li, W. Xie, F. Cheng and J. Chen, *Nat. Commun.*, 2018, **9**, 2373.
175. Z. Qiu, C.-W. Tai, G. A. Niklasson and T. Edvinsson, *Energ. Environ. Sci.*, 2019, **12**, 572-581.
176. S. Li, Y. Wang, S. Peng, L. Zhang, A. M. Al-Enizi, H. Zhang, X. Sun and G. Zheng, *Adv. Energy Mater.*, 2016, **6**, 1501661.
177. C. Kuai, Y. Zhang, D. Wu, D. Sokaras, L. Mu, S. Spence, D. Nordlund, F. Lin and X.-W. Du, *ACS Catal.*, 2019, **9**, 6027-6032.
178. C. Kuai, Z. Xu, C. Xi, A. Hu, Z. Yang, Y. Zhang, C.-J. Sun, L. Li, D. Sokaras and C. Dong, *Nat. Catal.*, 2020, **3**, 743-753.
179. L. J. Enman, M. B. Stevens, M. H. Dahan, M. R. Nellist, M. C. Toroker and S. W. Boettcher, *Angew. Chem. Int. Edit.*, 2018, **130**, 13022-13026.
180. S. Li, Y. Zhang, N. Liu, C. Yu, S.-J. Lee, S. Zhou, R. Fu, J. Yang, W. Guo and H. Huang, *Joule*, 2020, **4**, 673-687.
181. Y. Pi, Y. Xu, L. Li, T. Sun, B. Huang, L. Bu, Y. Ma, Z. Hu, C. W. Pao and X. Huang, *Adv. Funct. Mater.*, 2020, **30**, 2004375.
182. B. Chakraborty, R. Beltrán-Suito, J. N. Hausmann, S. Garai, M. Driess and P. W. Menezes, *Adv. Energy Mater.*, 2020, **10**, 2001377.
183. M. Chen, S. Lu, X. Z. Fu and J. L. Luo, *Adv. Sci.*, 2020, **7**, 1903777.

184. P. W. Menezes, C. Panda, S. Garai, C. Walter, A. Guiet and M. Driess, *Angew. Chem. Int. Edit.*, 2018, **130**, 15457-15462.
185. B. Wang, K. Zhao, Z. Yu, C. Sun, Z. Wang, N. Feng, L. Mai, Y. Wang and Y. Xia, *Energ. Environ. Sci.*, 2020, **13**, 2200-2208.
186. B. Ni, P. He, W. Liao, S. Chen, L. Gu, Y. Gong, K. Wang, J. Zhuang, L. Song and G. Zhou, *Small*, 2018, **14**, 1703749.
187. P. Wang, J. Qi, C. Li, X. Chen, J. Luo, W. Li, X. Shi, L. Olivet, T. Wang and C. Liang, *Int. J. Hydrogen Energ.*, 2019, **44**, 14955-14967.
188. T. Wu, S. Sun, J. Song, S. Xi, Y. Du, B. Chen, W. A. Sasangka, H. Liao, C. L. Gan and G. G. Scherer, *Nat. Catal.*, 2019, **2**, 763-772.
189. M. W. Kanan, J. Yano, Y. Surendranath, M. Dinca, V. K. Yachandra and D. G. Nocera, *J. Am. Chem. Soc.*, 2010, **132**, 13692-13701.
190. B. S. Yeo and A. T. Bell, *J. Am. Chem. Soc.*, 2011, **133**, 5587-5593.
191. M. Zhang, M. De Respinis and H. Frei, *Nat. Chem.*, 2014, **6**, 362-367.
192. C. Yang, O. Fontaine, J. M. Tarascon and A. Grimaud, *Angew. Chem. Int. Edit.*, 2017, **129**, 8778-8782.
193. Y. Zhu, H.-C. Chen, C.-S. Hsu, T.-S. Lin, C.-J. Chang, S.-C. Chang, L.-D. Tsai and H. M. Chen, *ACS Energy Lett.*, 2019, **4**, 987-994.
194. J. Wang, S.-J. Kim, J. Liu, Y. Gao, S. Choi, J. Han, H. Shin, S. Jo, J. Kim and F. Ciucci, *Nat. Catal.*, 2021, **4**, 212–222.
195. H. Jiang, Q. He, X. Li, X. Su, Y. Zhang, S. Chen, S. Zhang, G. Zhang, J. Jiang and Y. Luo, *Adv. Mater.*, 2019, **31**, 1805127.
196. S. Peng, F. Gong, L. Li, D. Yu, D. Ji, T. Zhang, Z. Hu, Z. Zhang, S. Chou and Y. Du, *J. Am. Chem. Soc.*, 2018, **140**, 13644-13653.
197. Z. Wang, W. Xu, X. Chen, Y. Peng, Y. Song, C. Lv, H. Liu, J. Sun, D. Yuan and X. Li, *Adv. Funct. Mater.*, 2019, **29**, 1902875.
198. Z. Xiao, Y.-C. Huang, C.-L. Dong, C. Xie, Z. Liu, S. Du, W. Chen, D. Yan, L. Tao and Z. Shu, *J. Am. Chem. Soc.*, 2020, **142**, 12087-12095.
199. K. Zhu, X. Zhu and W. Yang, *Angew. Chem. Int. Edit. International Edition*, 2019, **58**, 1252-1265.
200. J. Deng, P. Ren, D. Deng and X. Bao, *Angew. Chem. Int. Edit.*, 2015, **54**, 2100-2104.
201. X. Cui, Y. Chen, M. Zhang, Y. W. Harn, J. Qi, L. Gao, Z. L. Wang, J. Huang, Y. Yang and Z. Lin, *Energ. Environ. Sci.*, 2020, **13**, 1743-1752.
202. G. Liu, P. Li, G. Zhao, X. Wang, J. Kong, H. Liu, H. Zhang, K. Chang, X. Meng and T. Kako, *J. Am. Chem. Soc.*, 2016, **138**, 9128-9136.
203. X. Han, Y. Yu, Y. Huang, D. Liu and B. Zhang, *ACS Catal.*, 2017, **7**, 6464-6470.
204. J. Masa, S. Piontek, P. Wilde, H. Antoni, T. Eckhard, Y. T. Chen, M. Muhler, U. P. Apfel and W. Schuhmann, *Adv. Energy Mater.*, 2019, **9**, 1900796.
205. M. Gao, L. Zhu, C. K. Peh and G. W. Ho, *Energ. Environ. Sci.*, 2019, **12**, 841-864.
206. M. Menzinger and R. Wolfgang, *Angew. Chem. Int. Edit.*, 1969, **8**, 438-444.
207. B. Jin, Y. Li, J. Wang, F. Meng, S. Cao, B. He, S. Jia, Y. Wang, Z. Li and X. Liu, *Small*, 2019, **15**, 1903847.
208. J. Xu, J. P. Sousa, N. E. Mordvinova, J. D. Costa, D. Y. Petrovykh, K. Kovnir, O. I. Lebedev and Y. V. Kolen'ko, *ACS Catal.*, 2018, **8**, 2595-2600.
209. H. Y. Wang, Y. Y. Hsu, R. Chen, T. S. Chan, H. M. Chen and B. Liu, *Adv. Energy Mater.*, 2015, **5**,

1500091.
210. Y. Duan, S. Sun, Y. Sun, S. Xi, X. Chi, Q. Zhang, X. Ren, J. Wang, S. J. H. Ong and Y. Du, *Adv. Mater.*, 2019, **31**, 1807898.
211. Z. Kou, Y. Yu, X. Liu, X. Gao, L. Zheng, H. Zou, Y. Pang, Z. Wang, Z. Pan and J. He, *ACS Catal.*, 2020, **10**, 4411-4419.
212. C. Zhong, Z. Han, T. Wang, Q. Wang, Z. Shen, Q. Zhou, J. Wang, S. Zhang, X. Jin and S. Li, *J. Mater. Chem. A*, 2020, **8**, 10831-10838..
213. F. L. Meng, G. Yilmaz, T. P. Ding, M. Gao and G. W. Ho, *Adv. Mater.*, 2019, **31**, 1903605.
214. J. Li and J. Gong, *Energ. Environ. Sci.*, 2020, **13**, 3748-3779.
215. Y.-F. Li and A. Selloni, *ACS Catal.*, 2014, **4**, 1148-1153.
216. A. Govind Rajan, J. M. P. Martirez and E. A. Carter, *J. Am. Chem. Soc.*, 2020, **142**, 3600-3612.
217. S. Lee, L. Bai and X. Hu, *Angew. Chem. Int. Edit.*, 2020, **59**, 8072-8077.
218. L. Bai, S. Lee and X. Hu, *Angew. Chem. Int. Edit.*, 2020, 10.1002/ange.202011388.
219. J. Y. Chen, L. Dang, H. Liang, W. Bi, J. B. Gerken, S. Jin, E. E. Alp and S. S. Stahl, *J. Am. Chem. Soc.*, 2015, **137**, 15090-15093.
220. M. Favaro, W. S. Drisdell, M. A. Marcus, J. M. Gregoire, E. J. Crumlin, J. A. Haber and J. Yano, *ACS Catal.*, 2017, **7**, 1248-1258.
221. N. Ortiz Peña, D. Ihiawakrim, M. Han, B. Lassalle-Kaiser, S. Carenco, C. Sanchez, C. Laberty-Robert, D. Portehault and O. Ersen, *ACS Nano*, 2019, **13**, 11372-11381.
222. A. Tsoukalou, P. M. Abdala, D. Stoian, X. Huang, M.-G. Willinger, A. Fedorov and C. R. Müller, *J. Am. Chem. Soc.*, 2019, **141**, 13497-13505.
223. J. T. Mefford, X. Rong, A. M. Abakumov, W. G. Hardin, S. Dai, A. M. Kolpak, K. P. Johnston and K. J. Stevenson, *Nat. Commun.*, 2016, **7**, 1-11.
224. Y.-L. Lee, J. Kleis, J. Rossmeisl, Y. Shao-Horn and D. Morgan, *Energ. Environ. Sci.*, 2011, **4**, 3966-3970.
225. J. Yan, Y. Wang, Y. Zhang, S. Xia, J. Yu and B. Ding, *Adv. Mater.*, 2020, 2007525.
226. J. Cao, A. Rinaldi, M. Plodinec, X. Huang, E. Willinger, A. Hammud, S. Hieke, S. Beeg, L. Gregoratti and C. Colbea, *Nat. Commun.*, 2020, **11**, 1-11.
227. A. Auer, M. Andersen, E.-M. Wernig, N. G. Hörmann, N. Buller, K. Reuter and J. Kunze-Liebhäuser, *Nat. Catal.*, 2020, **3**, 797-803.
228. H. Bluhm, M. Hävecker, A. Knop-Gericke, E. Kleimenov, R. Schlögl, D. Teschner, V. I. Bukhtiyarov, D. F. Ogletree and M. Salmeron, *J. Phys. Chem. B*, 2004, **108**, 14340-14347.
229. A. Rajput, A. Kundu and B. Chakraborty, *ChemElectroChem*, 2021, **8**, 1698.
230. A. Zhang, Y. Liang, H. Li, B. Zhang, Z. Liu, Q. Chang, H. Zhang, C.-F. Zhu, Z. Geng and W. Zhu, *Nano Lett.*, 2020, **20**, 8229-8235.
231. H. Tian, L. Zeng, Y. Huang, Z. Ma, G. Meng, L. Peng, C. Chen, X. Cui and J. Shi, *Nano-Micro Lett.*, 2020, **12**, 1-14.